DC SQUID based detection of a micromechanical oscillator

Michael Schmid

A Thesis presented for the degree of
Master of Science

Supervisor: **Univ.-Prof. Dr. Gerhard Kirchmair**

Superconducting Quantum Circuits Group
Fakultät für Mathematik, Informatik und Physik
Institut für Experimentalphysik
Universität Innsbruck
Austria

May 2018

DC SQUID based detection of a micromechanical oscillator

Michael Schmid

Submitted for the degree of Master of Science
May 2018

Abstract

The goal of this thesis is to detect the thermal fluctuations of a micromechanical oscillator using a DC SQUID. We describe the characterisation process of our SQUID sensor and use a stochastic numerical model to determine its characteristic parameters. After aligning the micro-cantilever to the SQUID, we analyse noise spectra to identify a signal from the oscillator. Due to issues in the fabrication of our SQUID and cantilever samples, the magnetic flux induced by the cantilever motion at 1 K is too small to be visible in the SQUID spectrum. This is investigated by estimations of the expected signal strength, which support an intensity below the limit of detection.

Acknowledgements

First of all, I want to thank my supervisor Gerhard for his excellent support throughout this master project and for giving me the chance to work in his research group. I enjoyed the time at the IQOQI a lot and will certainly benefit from what I learnt in everything the future holds for me.
Also my girlfriend Theresa was a great help throughout those years of studying. I would like to thank her for all the patience she had with me and for always being such a positive person that keeps me in a good mood and gives me strength.
My parents also gave me huge support and I want to thank them for reminding me of the really important things in life. Home is always a great place to find cosiness and distraction from the sometimes stressful days in the life of a student.
Last but not least, I would like to thank all my friends, those who have accompanied me starting from my early days in kindergarten, but also those who I met in recent years at the university. Their support and all the funny moments I got to share with them are what made my time as a student in Innsbruck such an amazing experience.

Cheers to you all!

Contents

Chapter 1

Introduction

Experiments where micro- or nanomechanical elements enter the regime of quantum mechanics have attracted increasing attention, especially in the last decade. Some key achievements paved the way for the emergence of a whole new field, be it ground state cooling of a mechanical oscillator [1], creating entanglement between mechanical motion and microwave signals [2], entering the strong coupling regime in cavity optomechanics [3] or being able to capture and release propagating quantum information with an electro-mechanical resonator [4].

In our research, we try to combine micromechanical resonators with superconducting circuits, which represent a promising platform for quantum simulation and computation. Most experiments to date make use of either optical cavities with a movable mirror or parallel plate capacitors with one flexible electrode to achieve a coupling between electromagnetics and mechanics. In contrast, our experiment tries to implement an inductive coupling between a superconducting circuit and the mechanical resonator.

Such a magneto-mechanical setup represents a novel platform for experiments of this type and provides a new set of tools, especially considering effects of superconductivity. As such, the proposal for our experiment [5] makes use of the Meissner effect to achieve the milestone of entering the strong single photon coupling regime.

The aim of this thesis is to realise a magneto-mechanical experiment that uses a SQUID to detect the motion of a mechanical oscillator. This should act as a starting point for the long term goal of achieving the strong single photon coupling.

Chapter 2

Theory

This chapter discusses some basic principles of the physics that underlies this work. The theoretical basics to be able to follow the analyses presented in this thesis are introduced. Most of the elaborations should be interpreted as a motivation of the respective subject and are far from being complete. Whenever suitable, the explanations are supported by references with a more thorough treatment.

2.1 Superconductors and Josephson junctions

Superconductivity is a macroscopic quantum effect that, among other phenomena, enables a dissipationless flow of electric currents. It can be described by a wave function

$$\Psi(\vec{r},t) = \Psi_0(\vec{r},t)e^{i\theta(\vec{r},t)} = \sqrt{n_{\mathrm{s}}(\vec{r},t)}e^{i\theta(\vec{r},t)}, \tag{2.1.1}$$

with amplitude $\Psi_0(\vec{r},t)$ and phase $\theta(\vec{r},t)$, which both can depend on position and time. In contrast to other quantum mechanics problems, the probability distribution of the macroscopic wave function $\Psi(\vec{r},t)$ is usually not normalised to one, but to the total number of carriers of the supercurrent. Hence, the probability density function $|\Psi(\vec{r},t)|^2 = n_s(\vec{r},t)$ describes the carrier density. These carriers of the supercurrent are correlated pairs of electrons, the so called Cooper-pairs.

If we make use of the continuity equation that one can derive from the Schrödinger equation, we find an expression for the supercurrent density $\vec{J}_\mathrm{s}(\vec{r},t)$ [6], which reads

$$\begin{aligned}\vec{J}_\mathrm{s}(\vec{r},t) &= q_\mathrm{s}\,\mathrm{Re}\left\{\Psi^*\left(\frac{\hbar}{m_\mathrm{s}i}\vec{\nabla}-\frac{q_\mathrm{s}}{m_\mathrm{s}}\vec{A}\right)\Psi\right\} = \\ &= \frac{q_\mathrm{s}n_\mathrm{s}\hbar}{m_\mathrm{s}}\left[\vec{\nabla}\theta(\vec{r},t)-\frac{2\pi}{\Phi_0}\vec{A}(\vec{r},t)\right] = \frac{q_\mathrm{s}n_\mathrm{s}\hbar}{m_\mathrm{s}}\vec{\gamma}(\vec{r},t). \qquad (2.1.2)\end{aligned}$$

Here, $q_\mathrm{s} = 2e$ and m_s are the charge and mass of a Cooper-pair, $\vec{A}(\vec{r},t)$ is the vector potential of the surrounding electromagnetic field and $\Phi_0 = h/2e$ is the magnetic flux quantum. It is assumed, that the Cooper-pair density $n_\mathrm{s}(\vec{r},t) = n_\mathrm{s}$ is static and homogeneous in the bulk of the superconductor. In the last step, we also introduced the gauge invariant phase gradient $\vec{\gamma}(\vec{r},t)$.

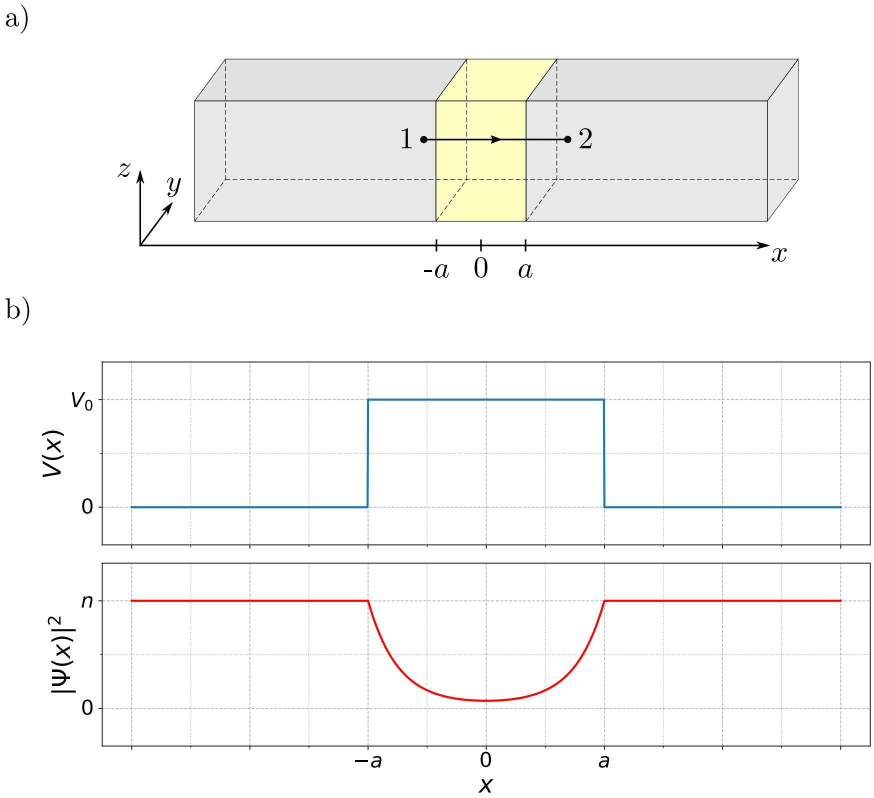

Figure 2.1: Sketch of a Josephson junction. Fig. a) shows the superconductor-insulator-superconductor arrangement with a small barrier dimension a. In b), the model as a potential barrier is illustrated. Also the carrier density $|\Psi(x)|^2$ along the JJ is shown. The superconductor contacts have an assumed constant carrier density of $n_{\mathrm{s},1} = n_{\mathrm{s},2} = n$.

If we connect two superconductors with a thin insulating layer as in fig. 2.1 a), the ability to conduct a dissipationless current can under certain conditions still persist due to the tunneling of Cooper-pairs through the barrier. Such an arrangement is called Josephson junction (JJ). To describe its behaviour, we start with defining the gauge invariant phase difference

$$\delta(\vec{r},t) = \int_1^2 \vec{\gamma}(\vec{r},t)\cdot \mathrm{d}\vec{l} = \theta_2 - \theta_1 - \frac{2\pi}{\Phi_0}\int_1^2 \vec{A}(\vec{r},t)\cdot \mathrm{d}\vec{l}, \tag{2.1.3}$$

which we obtain by integrating $\vec{\gamma}(\vec{r},t)$ along a path from 1 to 2, as illustrated in fig. 2.1 a). The notation $\theta_i = \theta(\vec{r_i},t)$ was used.

The insulating layer can be modelled as a potential barrier with height V_0 that the Cooper-pairs have to tunnel through, see fig. 2.1 b). By matching the boundary conditions of the macroscopic superconductor wave functions with the evanescent insulator wave function, one can find an expression for the current I_J through the JJ

$$I_\mathrm{J} = I_\mathrm{c}\sin(\delta), \tag{2.1.4}$$

with the critical current of the junction I_c, which is the maximum supercurrent a JJ can maintain. This is the first Josephson relation. The second one can be determined from the time derivative of eq. (2.1.3). It expresses the voltage U_J across the JJ as

$$U_\mathrm{J} = \frac{\hbar}{2e}\dot{\delta} = \frac{\Phi_0}{2\pi}\dot{\delta}. \tag{2.1.5}$$

Equations (2.1.4) and (2.1.5) fully describe the behaviour of the Josephson junction element.

2.2 DC SQUID

The elements we introduced so far can be combined to form a so called superconducting quantum interference device, in short SQUID. Such a superconducting circuit can be used to detect tiny magnetic field variations. Even though first experimental realisations of a SQUID already date back to 1964 [7], SQUID magnetometers still achieve record-breaking magnetic field sensitivities. Due to that, a so called DC SQUID represents the key element in our experimental arrangement.

2.2.1 Layout and function

The DC SQUID consists of a superconducting ring which is interrupted in two points by thin insulating layers that form Josephson junctions. In fig. 2.2 we show two possible layouts of such a SQUID.

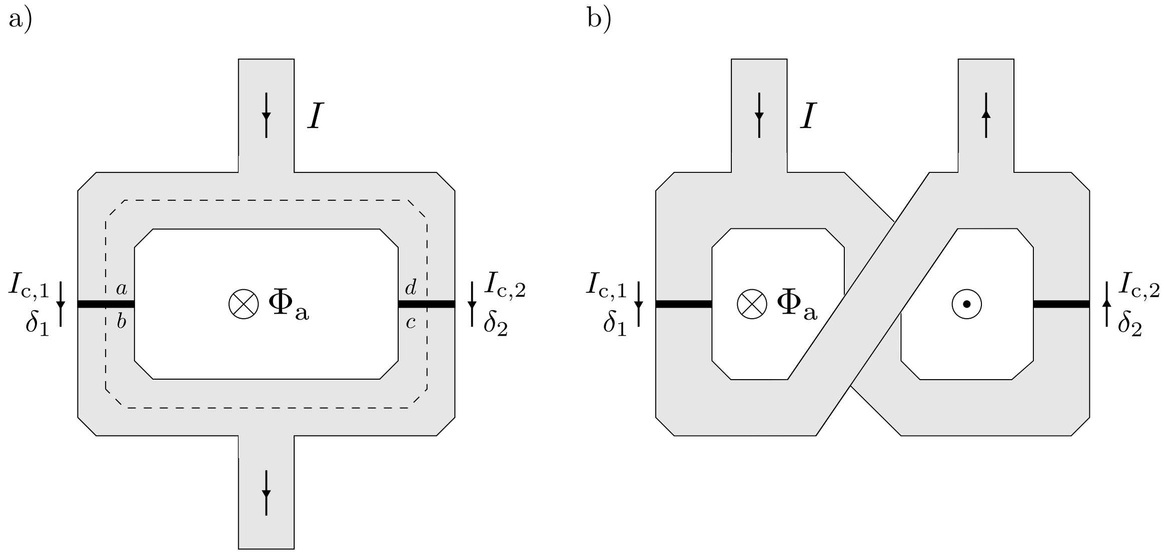

Figure 2.2: Sketch of two realisations of a DC SQUID. Fig. a) illustrates a magnetometer layout, whereas in fig. b) a gradiometer design is shown. Variable parameters are the bias current I and the external magnetic flux Φ_a. The Josephson junctions are parametrised by their critical current $I_{c,i}$ and the junction phase difference δ_i, see eq. (2.1.4).

The grey regions mark the superconducting loop and the thin black sections are JJs. Figure 2.2 a) shows a magnetometer design of the SQUID. Such an arrangement is suited to directly measure the magnetic field strength. In contrast, the figure eight shape in fig. 2.2 b) represents a gradiometer design. With this layout, a SQUID measures the magnetic field gradient, in this case along the horizontal direction.

The functional principle of the SQUID is based on the superconductivity effect of fluxoid quantisation. We can express this, by integrating the phase gradient $\vec{\nabla}\theta$ of the macroscopic wave function along a closed contour C, as indicated by the dashed line in fig. 2.2 a),

$$\oint_C \vec{\nabla}\theta \cdot \mathrm{d}\vec{l} = \frac{2\pi}{\Phi_0}\left[\Lambda \oint_C \vec{J}_\mathrm{s} \cdot \mathrm{d}\vec{l} + \oint_C \vec{A} \cdot \mathrm{d}\vec{l}\right] = 2\pi n. \tag{2.2.1}$$

For this we introduced the London coefficient $\Lambda = m_\mathrm{s}/n_\mathrm{s}q_\mathrm{s}^2$ and made use of eq. (2.1.2). The integral has to be equal to an integer multiple n of 2π in order to get constructive interference of the wave function. Via eq. (2.1.3), we can also express this in form of the gauge invariant phase differences δ_1 and δ_2 of the two JJs. One finds

$$\begin{aligned} \delta_2 - \delta_1 &= \frac{2\pi}{\Phi_0}\left[\oint_C \vec{A}\cdot \mathrm{d}\vec{l} + \Lambda\int_b^c \vec{J}_\mathrm{s}\cdot \mathrm{d}\vec{l} + \Lambda\int_d^a \vec{J}_\mathrm{s}\cdot \mathrm{d}\vec{l}\right] = \\ &= 2\pi\frac{\Phi_\mathrm{T}}{\Phi_0}. \end{aligned} \tag{2.2.2}$$

We see that the phase differences are connected via the total flux through the SQUID loop Φ_T. The vector potential $\vec{A}$ contains contributions from the externally applied magnetic field, indicated by Φ_a in fig. 2.2, as well as the field induced by the circulating current in the SQUID loop. The two integral terms involving the supercurrent density $\vec{J}_\mathrm{s}$ describe the so called kinetic inductance of the SQUID loop. Usually these contributions can be neglected, by taking the integration contour C deep inside the bulk material of the loop. The supercurrents only flow in a thin layer on the surface of the superconductor. This layer has a thickness on the order of the London penetration depth $\lambda_\mathrm{L} = \sqrt{\Lambda/\mu_0}$, which is 39 nm for niobium [8]. Hence, $\vec{J}_\mathrm{s} \approx 0$ inside the bulk superconductor.

2.2.2 RCSJ model

A versatile method for describing the behaviour of a DC SQUID is provided by the resistively and capacitively shunted junction (RCSJ) model. It incorporates the effect of intrinsic junction capacitance C_k, junction shunt resistance R_k, SQUID loop inductance L_k and the externally applied magnetic flux Φ_a. Also the Johnson current noise $I_{\mathrm{N},k}$ of the shunt resistors plays a key role. Its implementation is discussed in sections 2.5 and 4.1. Further, the model can be extended by taking asymmetries in all these parameters into account. We can represent the RCSJ model by the following schematic in fig. 2.3.

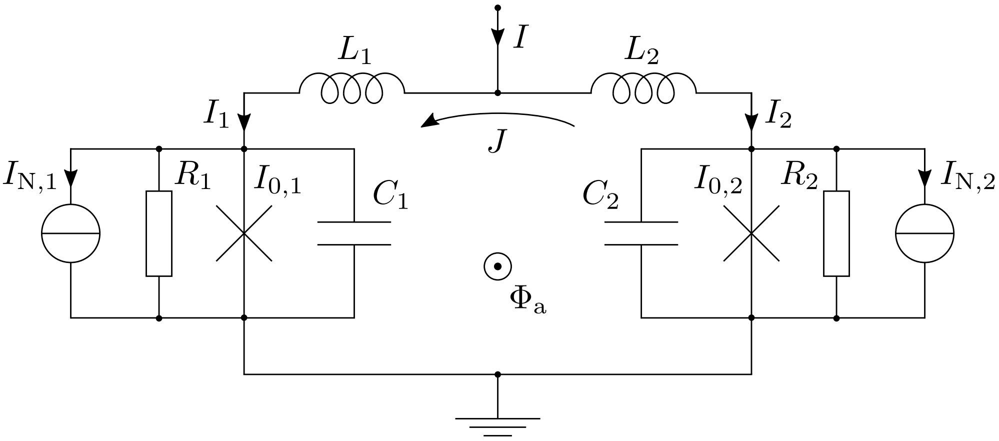

Figure 2.3: Schematics of the RCSJ model of the DC SQUID.

The currents in the two arms of the SQUID loop, I_1 and I_2, can be expressed as a superposition of the externally applied bias current I and the circulating ring current J by

$$I_1 = \frac{I}{2} + J \qquad \text{and} \qquad I_2 = \frac{I}{2} - J.$$

With the nodal rule for each junction, we can further decompose this into

$$\begin{aligned} \frac{I}{2} \pm J &= I_{\mathrm{J},k} + I_{\mathrm{R},k} + I_{\mathrm{C},k} + I_{\mathrm{N},k} = \\ &= I_{0,k} \sin(\delta_k) + \frac{\Phi_0}{2\pi R_k}\dot{\delta}_k + \frac{\Phi_0}{2\pi} C_k \ddot{\delta}_k + I_{\mathrm{N},k}, \end{aligned} \tag{2.2.3}$$

where we used the junction supercurrent $I_{\mathrm{J},k}$ from eq. (2.1.4), the quasiparticle current $I_{\mathrm{R},k} = U_{\mathrm{J},k}/R_k$, the displacement current $I_{\mathrm{C},k} = C_k \dot{U}_{\mathrm{J},k}$ and the thermal noise current $I_{\mathrm{N},k}$. The junction voltage $U_{\mathrm{J},k}$ is defined in eq. (2.1.5).

In eq. (2.2.2), we found that the two junction phases are connected via the total magnetic flux Φ_T through the SQUID loop. This can also be expressed as

$$\delta_2 - \delta_1 = 2\pi \frac{\Phi_\mathrm{T}}{\Phi_0} = \frac{2\pi}{\Phi_0}\left(\Phi_\mathrm{a} + LJ - \alpha_\mathrm{L} L \frac{I}{2}\right) \tag{2.2.4}$$

with the loop inductance $L = L_1 + L_2$ and the inductance asymmetry parameter $\alpha_\mathrm{L} = (L_2 - L_1)/L$. We see that Φ_T is the sum of the externally applied magnetic flux Φ_a, the flux caused by the ring current $\Phi_\mathrm{J} = LJ$ and the self-flux $\Phi_\mathrm{I} = -\alpha_\mathrm{L} LI/2$ created by the bias current. This expression can be used to calculate the circulating current J for a given combination of externally applied parameters (I, Φ_a).

For the purpose of comparability, it makes sense to convert the SQUID parameters to normalised quantities. To this end, we divide currents in eq. (2.2.3) by the average critical current $I_0 = (I_{0,1} + I_{0,2})/2$ and time t by $\omega_\mathrm{c}^{-1} = \Phi_0/2\pi I_0 R$. With the introduction of the asymmetry parameters

$$\alpha_\mathrm{I} = \frac{I_{0,2} - I_{0,1}}{I_{0,1} + I_{0,2}} \qquad \alpha_\mathrm{R} = \frac{R_1 - R_2}{R_1 + R_2} \qquad \alpha_\mathrm{C} = \frac{C_2 - C_1}{C_1 + C_2} \qquad \alpha_\mathrm{L} = \frac{L_2 - L_1}{L_1 + L_2} \tag{2.2.5}$$

we find the normalised version of the RCSJ model:

$$\frac{i}{2} + j = (1 - \alpha_\mathrm{I})\sin(\delta_1) + (1 - \alpha_\mathrm{R})\dot{\delta}_1 + \beta_\mathrm{C}(1 - \alpha_\mathrm{C})\ddot{\delta}_1 + i_{\mathrm{N},1}, \tag{2.2.6}$$

$$\frac{i}{2} - j = (1 + \alpha_\mathrm{I})\sin(\delta_2) + (1 + \alpha_\mathrm{R})\dot{\delta}_2 + \beta_\mathrm{C}(1 + \alpha_\mathrm{C})\ddot{\delta}_2 + i_{\mathrm{N},2}, \tag{2.2.7}$$

$$\delta_2 - \delta_1 = 2\pi\phi_\mathrm{T} = 2\pi\left(\phi_\mathrm{a} + \frac{\beta_\mathrm{L}}{2}j - \frac{\alpha_\mathrm{L}\beta_\mathrm{L}}{4}i\right). \tag{2.2.8}$$

The lower-case flux variables ϕ_i are normalised to the flux quantum Φ_0 and we introduced the important Stewart-McCumber parameter β_C and the screening parameter β_L, defined by:

$$\beta_\mathrm{C} = \frac{2\pi I_0 R^2 C}{\Phi_0} \qquad \beta_\mathrm{L} = \frac{2LI_0}{\Phi_0} \qquad \phi_\mathrm{a} = \frac{\Phi_\mathrm{a}}{\Phi_0}$$

$$R = \frac{2R_1R_2}{R_1 + R_2} \qquad C = \frac{C_1 + C_2}{2} \qquad L = L_1 + L_2$$

Finally, we can also formulate the voltage across the SQUID in terms of the junction voltages

$$u = \frac{(1 + \alpha_\mathrm{L})u_1 + (1 - \alpha_\mathrm{L})u_2}{2}, \tag{2.2.9}$$

with u normalised to I_0R_0 and $u_k = \dot{\delta}_k = U_{\mathrm{J},k}/I_0R_0$.

2.3 Mechanical oscillator

As already mentioned, the aim of this thesis is to detect the motion of a micromechanical oscillator via its inductive coupling to a SQUID. In this section we discuss some key concepts of such oscillators, with a special focus on the cantilever beam as we use it in our experiment. The analysis closely follows the introductions in refs. [9, 10]. We restrict our description to a purely classical treatment in this section. A quantum-mechanical extension follows in section 2.4.

2.3.1 Eigenmodes and -frequencies

A mechanical oscillator features multiple bending and torsional modes with different mode shapes $u_n(x)$ and resonance frequencies ω_n. Each of these modes can individually be described as a harmonic oscillator. For a cantilever beam as we use it in our experiment, the mode shapes take the form [9]

$$\begin{aligned} u_n(x) = C \Bigg\{ \sin\left(\alpha_n \frac{x}{l}\right) - \sinh\left(\alpha_n \frac{x}{l}\right) - \\ - \frac{\sin(\alpha_n) + \sinh(\alpha_n)}{\cos(\alpha_n) + \cosh(\alpha_n)} \left[\cos\left(\alpha_n \frac{x}{l}\right) - \cosh\left(\alpha_n \frac{x}{l}\right)\right] \Bigg\}, \end{aligned} \tag{2.3.1}$$

with l the length of the beam, α_n a numerical coefficient listed for the first few modes in table 2.1 and C a normalisation constant. Figure 2.4 illustrates the shape of the fundamental mode $u_0(x)$. The corresponding (angular) eigenfrequencies are

$$\omega_n = 2\pi f_n = \frac{\alpha_n^2}{l^2} \sqrt{\frac{D}{\rho A}}. \tag{2.3.2}$$

Here, $A = wh$ denotes the cross-sectional area of the beam with width w and height h, $D = EI/(1-\nu)$ the bending rigidity, $I = h^3 w/12$ the moment of inertia, E the Young's modulus, ν the Poisson's ratio and ρ the mass density. For silicon, these material properties are [11, 12]

$$E = 170\,\mathrm{GPa}, \qquad \nu = 0.064, \qquad \rho = 2330\,\mathrm{kg/m^3}.$$

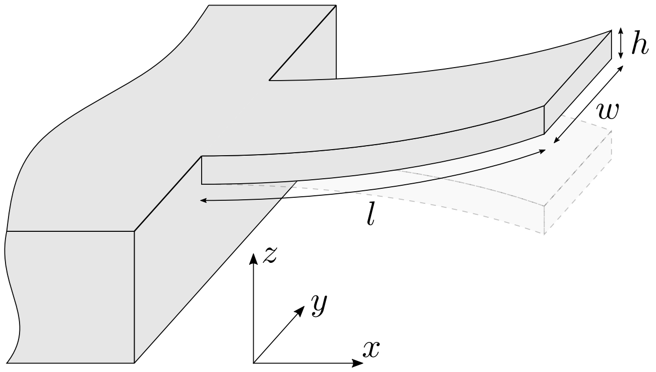

Figure 2.4: Sketch of the mode shape $u_0(x)$ for the fundamental mode of a cantilever beam.

The cantilever displacement $u(x,t)$ can hence be decomposed into the eigenmodes according to

$$u(x,t) = \mathrm{Re}\left\{\sum_n c_n(t) u_n(x) e^{i\omega_n t}\right\}, \tag{2.3.3}$$

with $c_n(t)$ being the amplitude of the n-th eigenmode component.

n	0	1	2	3	4
α_n	1.875	4.694	7.855	10.996	14.137

Table 2.1: Coefficients α_n for the first five eigenmodes [9]. The values are obtained by numerically solving the equation $\cos(\alpha_n)\cosh(\alpha_n) + 1 = 0$.

2.3.2 Harmonic oscillator

We would like to describe the response of a mechanical oscillator to a force of a certain frequency $F(\omega)$. To this end, we start with the equation of motion of a damped harmonic oscillator that is driven by an external force $F(t)$

$$m\ddot{u} = -k_\mathrm{R} u - m\gamma_\mathrm{R}\dot{u} + F(t), \tag{2.3.4}$$

where m is the effective mass, k_R is the spring constant and γ_R the damping constant of the oscillator. With the Fourier transformation $x(\omega) = \int_{-\infty}^{\infty} e^{-i\omega t} x(t) \mathrm{d}t$, we can rewrite this in frequency space as

$$- m\omega^2 u(\omega) = -k_\mathrm{R} u(\omega) - i m\omega\gamma_\mathrm{R} u(\omega) + F(\omega). \tag{2.3.5}$$

This allows us to define the mechanical susceptibility $\chi_\mathrm{HO}(\omega)$. If we express the spring constant $k_\mathrm{R} = m\omega_\mathrm{R}^2$ by the oscillator resonance frequency ω_R and the damping constant $\gamma_\mathrm{R} = \omega_\mathrm{R}/Q$ via the quality factor Q, we obtain [9, 10]

$$\chi_\mathrm{HO}(\omega) = \frac{u(\omega)}{F(\omega)} = \frac{1}{m(\omega_\mathrm{R}^2 - \omega^2 - i\omega\omega_\mathrm{R}/Q)}. \tag{2.3.6}$$

We can interpret $\chi_\mathrm{HO}(\omega)$ as a transfer function. Its magnitude

$$|\chi_\mathrm{HO}(\omega)|^2 = \frac{1}{m^2\left[\left(\omega_\mathrm{R}^2 - \omega^2\right)^2 + \omega^2\omega_\mathrm{R}^2/Q^2\right]} \tag{2.3.7}$$

describes the response of the displacement u to a force at a certain frequency $F(\omega)$. For low frequencies this expression is constant with $|\chi_{\mathrm{HO}}(\omega)|^2 \approx (m\omega_{\mathrm{R}}^2)^{-2} = k_{\mathrm{R}}^{-2}$ and for frequencies $\omega \gg \omega_{\mathrm{R}}$ it tends to 0. Further, for high Q resonators the line shape around $\omega \approx \omega_{\mathrm{R}}$ can be approximated by a Lorentzian of the form

$$|\chi_{\mathrm{HO}}(\omega \approx \omega_{\mathrm{R}})|^2 = \frac{\omega_{\mathrm{R}}^{-2}}{m^2\left[(\omega_{\mathrm{R}} - \omega)^2 + \omega_{\mathrm{R}}^2/Q^2\right]}. \tag{2.3.8}$$

On resonance, i.e. $\omega = \omega_{\mathrm{R}}$, we obtain $|\chi_{\mathrm{HO}}(\omega_{\mathrm{R}})|^2 \approx Q^2/(m\omega_{\mathrm{R}}^2)^2 = Q^2/k_{\mathrm{R}}^2$. This illustrates the strong enhancement by a factor of Q^2 with respect to the low frequency value.

2.3.3 Thermal motion

Instead of a dedicated external driving force, the $F(t)$ term in eq. (2.3.4) can also describe the thermal excitation of the motion of the mechanical oscillator. The drive is then represented by the thermal Langevin force $F_{\mathrm{n}}(t)$, which is described by a stochastic process and is typically modelled as a white noise source. Hence, we can characterise it by the spectral noise density $S_{F_{\mathrm{n}}F_{\mathrm{n}}}$, which is constant for white noise, see section 2.5.2.

Consequently, also the thermal motion of the oscillator has to be described as a stochastic process. We can determine the spectral noise density S_{uu} for the displacement u with the help of the mechanical susceptibility χ_{HO} from eq. (2.3.6) according to

$$S_{uu}(\omega) = |\chi_{\mathrm{HO}}|^2\, S_{F_{\mathrm{n}}F_{\mathrm{n}}}. \tag{2.3.9}$$

The displacement u is a zero mean process, i.e. $\langle u \rangle = 0$. Therefore, we can use eq. (2.5.13) to calculate the mean square displacement of the oscillator:

$$\langle u^2 \rangle = \int_0^\infty S_{uu}(\omega)\frac{\mathrm{d}\omega}{2\pi} = \frac{1}{4}\frac{Q}{m^2\omega_{\mathrm{R}}^3} S_{F_{\mathrm{n}}F_{\mathrm{n}}}. \tag{2.3.10}$$

In thermal equilibrium, the equipartition theorem states that each degree of freedom has a mean energy of $k_{\mathrm{B}}T/2$, where k_{B} is the Boltzmann constant and T is the temperature. For the one-dimensional motion of the mechanical oscillator, this results in

$$\frac{1}{2}k_{\mathrm{R}}\langle u^2 \rangle = \frac{1}{2}m\langle \dot{u}^2 \rangle = \frac{1}{2}k_{\mathrm{B}}T, \tag{2.3.11}$$

with the potential energy $k_\mathrm{R}\langle u^2\rangle/2$ and the kinetic energy $m\langle\dot{u}^2\rangle/2$. Combining eqs. (2.3.10) and (2.3.11), we can finally quantify the spectral noise density $S_{F_\mathrm{n}F_\mathrm{n}}$ of the thermal Langevin force F_n:

$$S_{F_\mathrm{n}F_\mathrm{n}} = \frac{4k_\mathrm{B}Tm\omega_\mathrm{R}}{Q} = 4k_\mathrm{B}Tm\gamma_\mathrm{R}. \tag{2.3.12}$$

2.4 Strong magnetic coupling

In this section, we are going to investigate the proposal [5] that motivated the work for this master thesis. We try to combine superconducting circuit elements with a micromechanical oscillator and facilitate the inductive coupling between those components. Our ultimate goal would be to enter the strong single photon coupling regime. This represents a key requirement for coherent state transfer in quantum information applications, where these so called hybrid devices could e.g. act as storage for quantum states [2, 4] or as quantum interfaces between qubits and optical fibres [3, 13].

In the proposal, the flux sensitive component is represented by a so called transmon qubit instead of the simple DC SQUID that we used. The transmon is a parallel circuit of a large shunt capacitance with either a single Josephson junction or a DC SQUID if it should be flux tunable. It can also be described as a LC circuit with a non-linear inductance that can be tuned via the externally applied flux. The associated qubit Hamiltonian $\hat{H}_\mathrm{qb}$ is the one of a harmonic oscillator with an additional anharmonicity term:

$$\hat{H}_\mathrm{qb} = \hbar\omega(\Phi)\hat{a}^\dagger\hat{a} - \frac{E_\mathrm{C}}{2}\hat{a}^\dagger\hat{a}^\dagger\hat{a}\hat{a} \tag{2.4.1}$$

$$\hbar\omega(\Phi) = \sqrt{8E_\mathrm{J}(\Phi)E_\mathrm{C}} - E_\mathrm{C} \tag{2.4.2}$$

$$E_\mathrm{J}(\Phi) = 2E_\mathrm{J,0}\cos\left(\frac{\pi\Phi}{\Phi_0}\right) \tag{2.4.3}$$

Here, $E_\mathrm{J}(\Phi)$ is the flux-tunable Josephson energy of the SQUID with $E_\mathrm{J,0}$ the equivalent for a single Josephson junction. E_C denotes the charging energy.

A simple cantilever beam is used as mechanical oscillator and is aligned to the SQUID loop of the transmon. The magnetic coupling is achieved via a strip of superconducting (SC) material on the tip of the beam. If this strip is placed in a magnetic field, surface currents are induced due to the Meissner effect, which screen the interior of the superconductor from the magnetic field. Those screening currents cause a magnetic field themselves, which can be detected by the SQUID. If the cantilever oscillates in a homogeneous field, the induced currents remain constant, but the varying distance to the transmon causes a change in the induced flux in the SQUID loop. Hence, we can use this mechanism to couple the motion of the cantilever to the transmon frequency. Figure 2.5 illustrates the experimental setup with the modification of using a gradiometric layout for the SQUID loop instead of the magnetometer design proposed in ref. [5].

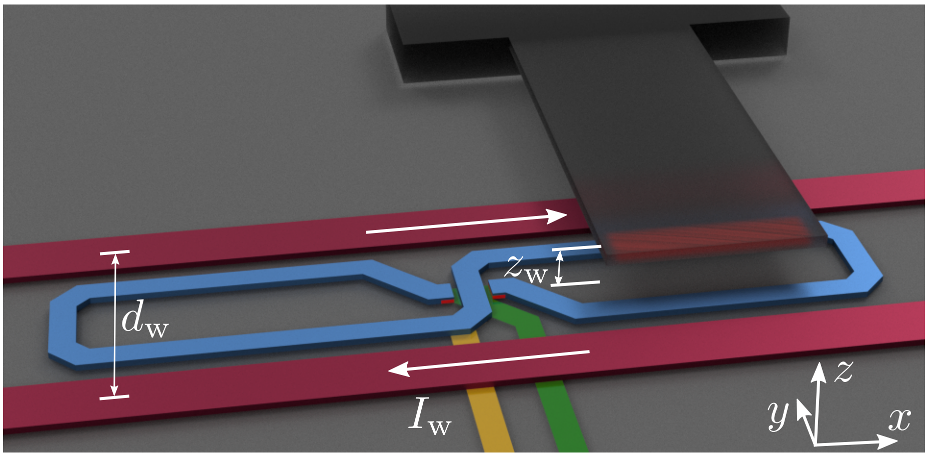

Figure 2.5: Experimental setup with the gradiometer SQUID (blue) in the centre and the cantilever (black) aligned on top of one loop half with a vertical distance of z_w. The SC strip is placed on the bottom of the cantilever tip, which is indicated in red and shines through the transparently rendered beam. A pair of wires (pink) encloses the SQUID loop, which are used to create the quadrupole magnetic field. The wire distance is d_w and a current I_w flows through the wires in opposing orientation.

The flux that threads the SQUID loop depends on the cantilever deflection z_m, i.e. $\Phi = \Phi(z_\mathrm{m})$. We can therefore develop $\omega[\Phi(z_\mathrm{m})]$ from eq. (2.4.2) to first order in z_m for small deviations around the cantilever resting position $z_\mathrm{m} = 0$. Making use of the quantum mechanical expression for the displacement $z_\mathrm{m} = z_\mathrm{zp}(\hat{b}^\dagger + \hat{b})$ with the zero point fluctuation amplitude z_zp and the mechanical and electromagnetic (transmon) annihilation operators $\hat{b}$ and $\hat{a}$, we obtain the standard micromechanics

Hamiltonian

$$\hat{H} = \hbar\omega\hat{a}^\dagger\hat{a} + \hbar\Omega\hat{b}^\dagger\hat{b} - \hbar g_0\hat{a}^\dagger\hat{a}(\hat{b}^\dagger + \hat{b}). \tag{2.4.4}$$

The anharmonicity term of the qubit Hamiltonian $\hat{H}_{\mathrm{qb}}$ was neglected in this expression. We can identify the harmonic oscillator terms for the transmon with $\omega = \omega[\Phi(0)]$ and the mechanical oscillator with the corresponding resonance frequency Ω. A straightforward calculation leads to the following result for the coupling strength g_0 [5]:

$$g_0 = z_{\mathrm{zp}} \left.\frac{\partial\omega[\Phi(z_{\mathrm{m}})]}{\partial z_{\mathrm{m}}}\right|_{z_{\mathrm{m}}=0} = \omega_0\phi\eta \tag{2.4.5}$$

$$\hbar\omega_0 = \sqrt{8E_{\mathrm{J},0}E_{\mathrm{C}}} \tag{2.4.6}$$

$$\phi = \frac{\pi\sin[\pi\Phi(0)/\Phi_0]}{\sqrt{2\cos[\pi\Phi(0)/\Phi_0]}} \tag{2.4.7}$$

$$\eta = \frac{z_{\mathrm{zp}}}{\Phi_0}\left.\frac{\partial\Phi(z_{\mathrm{m}})}{\partial z_{\mathrm{m}}}\right|_{z_{\mathrm{m}}=0} \tag{2.4.8}$$

By tuning $\Phi(0)$, one can set ϕ such that the coupling can be switched on or off. The key parameter to change the coupling strength is the magnetomechanical (MM) coupling η. It describes the change in the induced flux in the SQUID for a zero point motion displacement z_{zp} of the mechanical oscillator.

The strong single photon coupling regime is characterised by $g_0 \gtrsim \Gamma_{\mathrm{m}}, \kappa$ where Γ_{m} is the mechanical and κ the electromagnetic decoherence rate. A further requirement for being able to perform sideband cooling of the mechanical motion to the ground state is the resolved sideband regime $\Omega/\kappa \gtrsim 1$. Assuming that the conditions $g_0 > \Gamma_{\mathrm{m}}$ and $\Omega > \kappa$ are fulfilled, as it was already demonstrated in multiple experiments [10], the proposal describes a possible way to also achieve the challenging requirement $g_0 > \kappa$.

The key idea for increasing the MM coupling η is changing the magnetic field pattern from a homogeneous to a quadrupole field of the form

$$\vec{B}_{\mathrm{qp}}(y, z) = b(-y\vec{e}_y + z\vec{e}_z), \tag{2.4.9}$$

which has a zero at the resting position $z = 0$ of the cantilever tip and a constant gradient b along the z-direction. The change of the induced flux in the SQUID loop is hence not only a result of the changing cantilever displacement, but also a change in the intensity of the screening currents of the SC strip. For zero deflection of the cantilever those currents vanish and no flux is induced in the SQUID loop. In conclusion, for the case of a homogeneous field $\eta \propto 1/z_{\mathrm{w}}^2$, whereas in the quadrupole field case $\eta \propto 1/z_{\mathrm{w}}$.

We can further quantify the MM coupling strength by

$$\eta = \chi\eta^*, \tag{2.4.10}$$

$$\eta^* = \frac{z_{\mathrm{zp}} b l_{\mathrm{s}} w_{\mathrm{s}}}{\Phi_0} = f(t_{\mathrm{s}}/w_{\mathrm{s}}) \frac{2 z_{\mathrm{zp}} B_{\mathrm{crit}} l_{\mathrm{s}}}{\Phi_0}, \tag{2.4.11}$$

with $f(x) = \left[1 + (\sqrt{2x} + x)(1+x)\right]^{-1/2}$, the strip length l_{s}, width w_{s} and thickness t_{s} (with $l_{\mathrm{s}} > w_{\mathrm{s}} > t_{\mathrm{s}}$ cf. fig. 2.5) and B_{crit} the critical field of the SC strip material. χ represents a geometry factor, which is on the order of 0.1 for the quadrupole field case, but almost an order of magnitude lower for a homogeneous field, see ref. [5].

The desired quadrupole field pattern can be achieved by combining the field $\vec{B}_{\mathrm{w}}$ of a pair of wires with counter propagating currents I_{w} (see fig. 2.5) with a bias field $\vec{B}_{\mathrm{bias}}$:

$$\vec{B}_{\mathrm{qp}} = \vec{B}_{\mathrm{w}} + \vec{B}_{\mathrm{bias}} \tag{2.4.12}$$

$$\vec{B}_{\mathrm{w}}(y,z) = \frac{\mu_0 I_{\mathrm{w}}}{2\pi}\left[\frac{-(z+z_{\mathrm{w}})\vec{e}_y + (y - d_{\mathrm{w}}/2)\vec{e}_z}{(z+z_{\mathrm{w}})^2 + (y-d_{\mathrm{w}}/2)^2} - \frac{-(z+z_{\mathrm{w}})\vec{e}_y + (y + d_{\mathrm{w}}/2)\vec{e}_z}{(z+z_{\mathrm{w}})^2 + (y+d_{\mathrm{w}}/2)^2}\right] \tag{2.4.13}$$

$$\vec{B}_{\mathrm{bias}} = \frac{\mu_0 I_{\mathrm{w}}}{2\pi} \frac{d_{\mathrm{w}}}{z_{\mathrm{w}}^2 + d_{\mathrm{w}}^2/4} \vec{e}_z \tag{2.4.14}$$

The optimal distance for the wire pair is given by $d_{\mathrm{w}} = 4z_{\mathrm{w}}$ [5]. By adding the bias field, the field strength equals zero at the resting position of the cantilever tip at $z = 0$. Furthermore, the gradient along the z-direction can be linearised around $z = 0$, where one obtains

$$\left.\frac{\partial B_{\mathrm{qp,z}}}{\partial z}\right|_{z=0} = b\left\{1 + \frac{18}{25}\left(\frac{y}{z_{\mathrm{w}}}\right)^2 + \mathcal{O}\left[\left(\frac{y}{z_{\mathrm{w}}}\right)^4\right]\right\}, \tag{2.4.15}$$

$$b = \frac{4\mu_0 I_{\mathrm{w}}}{25\pi z_{\mathrm{w}}^2}. \tag{2.4.16}$$

The field strength at the SC strip position has to be smaller than the first critical field of the SC material in order to maintain the field screening properties. For niobium this is approx. $B_{\text{crit}} = 140\,\text{mT}$ [14]. The magnetic field pattern that results from eqs. (2.4.12) to (2.4.14) is illustrated in fig. 2.6.

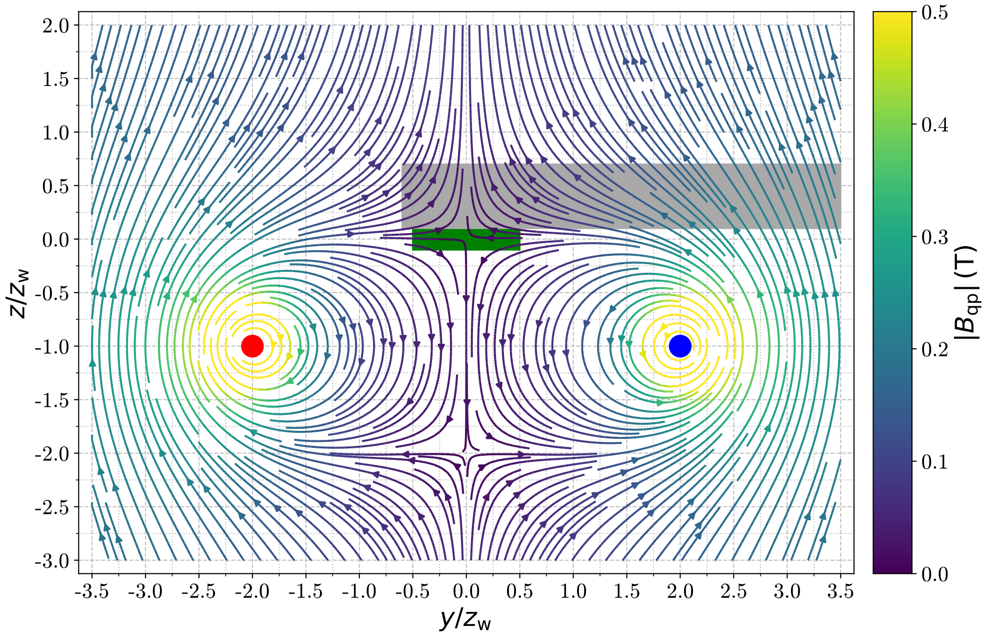

Figure 2.6: Quadrupole magnetic field $\vec{B}_{\text{qp}}$ pattern in a y-z cross-section, cf. fig. 2.5. The field is generated by two wires with currents I_{w} of opposing orientation, indicated by the red and blue circles, in combination with a homogeneous external bias field. The quadrupole approximation holds for the region around the SC strip (green rectangle) on the tip of the cantilever (grey rectangle). Field strengths are only reflected by the colour coding and not by the density of the field lines.

With feasible parameters of $z_{\text{w}} \approx 5\,\mu\text{m}$, a quadrupole wire current of $I_{\text{w}} = 1\,\text{A}$ and a quality factor of the transmon of $Q = \omega_0/\kappa = 1 \times 10^6$, one can achieve a coupling strength of $g_0/\kappa = 3.5$, which is well within the single photon strong coupling regime.

2.5 Stochastic differential equations - SDE

The following section treats the basics of stochastic differential equations (SDEs) and two important noise processes, Gaussian white noise and the Ornstein-Uhlenbeck (OU) process. Section 2.5.1 is a short description based on ref. [15] of the numerical

SDE solver following the Heun method. The discussion about noise processes is motivated by the instructive paper of Gillespie [16].

2.5.1 Heun method

In the following, we want to develop a method to numerically solve a stochastic differential equation. Our aim is to integrate a SDE of the general form

$$\dot{x}(t) = q(t, x(t)) + g(t, x(t))\xi(t), \tag{2.5.1}$$

where $x(t)$ is the variable we want to solve for, $q(t, x(t))$ is the deterministic and $g(t, x(t))\xi(t)$ the stochastic term. As indicated, in a very general case both q and g can depend explicitly on time t as well as on the value of the variable x at that point. Typically, we also call q the drift term and g the diffusion term, the origin of these terms will be clarified later. $\xi(t)$ denotes the noise process, which would in our case either be Gaussian white noise or Ornstein-Uhlenbeck noise. We treat those different types of noise in the subsequent sections.

By formally integrating eq. (2.5.1) and introducing the discretised time steps $t_i = i \cdot h$ with a constant step size of h, we can obtain an update formula for x of the form

$$x(t_{i+1}) = x(t_i) + \int_{t_i}^{t_{i+1}} q(s, x(s))\mathrm{d}s + \int_{t_i}^{t_{i+1}} g(s, x(s))\xi(s)\mathrm{d}s. \tag{2.5.2}$$

To get rid of the integral expressions, we can Taylor expand q and g and only keep terms up to first order in h. By following a similar approach to the standard Runge-Kutta method, we finally end up with the so called Heun method, which is described by eq. (2.5.3). A thorough derivation can be found e.g. in ref. [15].

$$\begin{aligned} k &= hq(t_i, x(t_i)), \\ l &= w(t_i)g(t_i, x(t_i)), \\ x(t_{i+1}) &= x(t_i) + \frac{h}{2}\left[q(t_i, x(t_i)) + q(t_{i+1}, x(t_i) + k + l)\right] + \\ &\quad + \frac{w(t_i)}{2}\left[g(t_i, x(t_i)) + g(t_{i+1}, x(t_i) + k + l)\right] + \mathcal{O}(h^{3/2}). \end{aligned} \tag{2.5.3}$$

This result combines the forward propagated Taylor expansion for q and g around the point $(t_i, x(t_i))$ with the backward propagated one around $(t_{i+1}, x(t_{i+1}))$. The

$x(t_{i+1})$ term that would appear in the argument of q and g is itself approximated by the forward propagated expression $x(t_{i+1}) = x(t_i) + k + l$. For the stochastic term we end up with the noise integral

$$w(t_i) = \int_{t_i}^{t_{i+1}} \xi(s)\mathrm{d}s. \tag{2.5.4}$$

It is the subject of section 4.1 to discuss the practical implementation of this expression in our numerical simulations.

2.5.2 Gaussian white noise

We shall now turn to the investigation of noise processes. Most often we encounter so called (Gaussian) white noise. The term *white* should indicate that the noise signal is composed of a wide range of frequencies, that all contribute equally. In fact the frequency spectrum of white noise would theoretically be infinitely wide, as we will see later. This also means, that the noise signal $\xi_{\mathrm{w}}(t)$ is not differentiable at any point t. It may seem that this is a purely theoretical construct. There are however many applications where we can use the white noise process as a useful model. The problem of restoring the correct physical behaviour is then simply shifted to the response of a system, which will not follow arbitrarily fast changes.

We also require, that our noise process should be Gaussian. This means, that if we analyse a large number of sample noise traces, we should for any time t obtain a Gaussian distribution of the sample values $\xi_{\mathrm{w}}(t)$. This property allows us to fully characterise the noise process with only two measures, the expectation value $\langle\xi_{\mathrm{w}}(t)\rangle$ and the auto-covariance $\mathrm{cov}\left[\xi_{\mathrm{w}}(t), \xi_{\mathrm{w}}(t')\right]$. The latter is defined via the covariance

$$\mathrm{cov}\left[x, y\right] = \big\langle (x - \langle x\rangle)(y - \langle y\rangle)\big\rangle = \langle xy\rangle - \langle x\rangle\langle y\rangle \tag{2.5.5}$$

For the Gaussian white noise, we get

$$\langle\xi_{\mathrm{w}}(t)\rangle = 0, \tag{2.5.6}$$

$$\mathrm{cov}\left[\xi_{\mathrm{w}}(t), \xi_{\mathrm{w}}(t')\right] = D\ \delta(t - t'). \tag{2.5.7}$$

The brackets $\langle\ldots\rangle$ indicate an average over a large number of sample traces, D is the diffusion constant and $\delta(t-t')$ represents the Dirac delta function. Accordingly, perfect white noise ξ_w is a zero mean, infinite variance process. With the notation $\mathcal{N}[\mu, \sigma^2]$ for a random variable that we pick from a normal distribution of mean μ and variance σ^2, this can formally be written as

$$\xi_\mathrm{w}(t) = \lim_{\mathrm{d}t \to 0} \mathcal{N}\left[0, \frac{D}{\mathrm{d}t}\right]. \tag{2.5.8}$$

This formulation also explains the role of the diffusion constant D. If we model a white noise process with a discrete and finite sampling time Δt instead of the infinitesimal $\mathrm{d}t$, we effectively limit the considered frequency range. Consequently, the variance of ξ_w is no longer infinite, but given by $D/\Delta t$.

To be able to characterise a process $x(t)$, we shall define the two important quantities auto-correlation function C_{xx} and power spectral density S_{xx}. In this context, the latter is usually also called noise spectral density. According to the Wiener-Khinchin theorem, these measures are related via the Fourier transform and are defined by

$$\begin{aligned} C_{xx}(t') &= \langle x(t)x(t+t')\rangle = \\ &= \int_0^\infty S_{xx}(\nu)\cos(2\pi\nu t')\mathrm{d}\nu, \qquad (2.5.9) \\ S_{xx}(\nu) &= 4\int_0^\infty C_{xx}(t')\cos(2\pi\nu t')\mathrm{d}t'. \qquad (2.5.10) \end{aligned}$$

The auto-correlation function $C_{xx}(t')$ describes the self-similarity between the original signal $x(t)$ and a copy $x(t+t')$ that is shifted by a time lag t'. For the noise spectral density $S_{xx}(\nu)$, the one-sided definition with $\nu \geq 0$ is used throughout this thesis. In the case of Gaussian white noise, we find

$$C_{\xi_\mathrm{w}\xi_\mathrm{w}}(t') = D\ \delta(t'), \tag{2.5.11}$$

$$S_{\xi_\mathrm{w}\xi_\mathrm{w}}(\nu) = 2D. \tag{2.5.12}$$

The noise signal ξ_w is completely uncorrelated even for smallest time shifts t'. Under the Fourier transform, the Dirac delta of the auto-correlation function is translated to a constant noise spectral density up to arbitrarily large frequencies. The relation of S_{xx} to the variance of a process $x(t)$,

$$\sigma_x^2 = \int_0^\infty S_{xx}(\nu)\mathrm{d}\nu \tag{2.5.13}$$

demonstrates the initially mentioned infinite variance for ξ_{w}, where all frequency components contribute equally to the noise variance with a magnitude of $S_{\xi_{\mathrm{w}}\xi_{\mathrm{w}}}(\nu)\mathrm{d}\nu = 2D\mathrm{d}\nu$.

2.5.3 Ornstein Uhlenbeck process

Another type of noise, which is in some sense more practically oriented, is the so called Ornstein Uhlenbeck (OU) noise. Its main difference to white noise is the effectively bounded frequency spectrum. This leads to a well defined variance for the OU noise process $\xi_{\mathrm{ou}}(t)$ but does not change the fact that it is not differentiable. Typically, the OU process is itself described by a SDE.

$$\frac{\mathrm{d}\xi_{\mathrm{ou}}(t)}{\mathrm{d}t} = -\frac{1}{\tau_{\mathrm{ou}}}\xi_{\mathrm{ou}}(t) + c^{1/2}\xi_{\mathrm{w}}(t) \tag{2.5.14}$$

Compared to eq. (2.5.1), we can identify the drift term as $q(t, \xi_{\mathrm{ou}}(t)) = -\tau_{\mathrm{ou}}^{-1}\xi_{\mathrm{ou}}(t)$ and the diffusion term as $g(t, \xi_{\mathrm{ou}}(t)) = c^{1/2}$. The parameters that describe the OU process are the relaxation time τ_{ou} and the diffusion constant c. It should be mentioned that the notation in eq. (2.5.14) is not very rigorous, because the time derivative of ξ_{ou} is in fact not defined. A way to circumvent this is to express the SDE by an update formula of the following form:

$$\xi_{\mathrm{ou}}(t + \mathrm{d}t) = \xi_{\mathrm{ou}}(t) - \frac{1}{\tau_{\mathrm{ou}}}\xi_{\mathrm{ou}}(t)\mathrm{d}t + c^{1/2}N(t)(\mathrm{d}t)^{1/2}. \tag{2.5.15}$$

Here, $N(t) = \mathcal{N}[0, 1]$ denotes a unit normal random variable. The peculiar notation for the diffusion term is mostly a matter of convenience, we could also rewrite it as $c^{1/2}N(t)(\mathrm{d}t)^{1/2} = \mathcal{N}[0, c\ \mathrm{d}t]$. It is however useful to keep track of the order in $\mathrm{d}t$ explicitly, especially if we calculate correlations where we can neglect terms with higher order than one.

The OU process is also a Gaussian process. If we consider eq. (2.5.15) and form expectation values over a set of sample realisations of ξ_{ou}, we can determine the mean $\langle\xi_{\mathrm{ou}}(t)\rangle$ and auto-covariance $\mathrm{cov}\left[\xi_{\mathrm{ou}}(t), \xi_{\mathrm{ou}}(t')\right]$ [16]. With the initial condition $\xi_{\mathrm{ou}}(t_0) = \xi_0$, one obtains

$$\langle\xi_{\mathrm{ou}}(t)\rangle = \xi_0 e^{-(t-t_0)/\tau_{\mathrm{ou}}}, \tag{2.5.16}$$

$$\mathrm{cov}\left[\xi_{\mathrm{ou}}(t), \xi_{\mathrm{ou}}(t')\right] = \frac{c\tau_{\mathrm{ou}}}{2}e^{-|t'-t|/\tau_{\mathrm{ou}}}(1 - e^{-2(t-t_0)/\tau_{\mathrm{ou}}}). \tag{2.5.17}$$

This fully describes the OU process and we can express ξ_{ou} by

$$\xi_{\mathrm{ou}}(t) = \mathcal{N}\left[\xi_0 e^{-(t-t_0)/\tau_{\mathrm{ou}}}, \frac{c\tau_{\mathrm{ou}}}{2}(1 - e^{-2(t-t_0)/\tau_{\mathrm{ou}}})\right]. \tag{2.5.18}$$

In most cases the transient period from the initial condition to a steady-state is of no interest. Hence, one defines the fully relaxed OU process as

$$\xi^*_{\mathrm{ou}}(t) = \lim_{t_0 \to -\infty} \xi_{\mathrm{ou}}(t) = \mathcal{N}\left[0, \frac{c\tau_{\mathrm{ou}}}{2}\right]. \tag{2.5.19}$$

For this we determine the properties

$$\langle \xi^*_{\mathrm{ou}}(t) \rangle = 0, \tag{2.5.20}$$

$$\operatorname{cov}\left[\xi^*_{\mathrm{ou}}(t), \xi^*_{\mathrm{ou}}(t')\right] = \frac{c\tau_{\mathrm{ou}}}{2} e^{-|t'-t|/\tau_{\mathrm{ou}}}. \tag{2.5.21}$$

We can use those results to calculate the auto-correlation $C_{\xi^*_{\mathrm{ou}}\xi^*_{\mathrm{ou}}}$ and noise spectral density $S_{\xi^*_{\mathrm{ou}}\xi^*_{\mathrm{ou}}}$ according to eqs. (2.5.9) and (2.5.10).

$$C_{\xi^*_{\mathrm{ou}}\xi^*_{\mathrm{ou}}}(t') = \frac{c\tau_{\mathrm{ou}}}{2} e^{-|t'|/\tau_{\mathrm{ou}}}, \tag{2.5.22}$$

$$S_{\xi^*_{\mathrm{ou}}\xi^*_{\mathrm{ou}}}(\nu) = \frac{2c\tau_{\mathrm{ou}}^2}{1 + (2\pi\tau_{\mathrm{ou}}\nu)^2}. \tag{2.5.23}$$

These outcomes highlight the key differences of the OU process compared to white noise. The noise signal shows significant auto-correlation also for time shifts $t' > 0$ and describes an exponential decay with the relaxation time τ_{ou} as time constant. Further, we can see that the noise spectral density falls off $\propto 1/\nu^2$ for ν larger than the corner frequency $\nu_{\mathrm{c}} = 1/2\pi\tau_{\mathrm{ou}}$. This means that the relaxation time sets the upper limit for the range of frequencies that contribute to the noise signal ξ_{ou}. Below the corner frequency, $S_{\xi^*_{\mathrm{ou}}\xi^*_{\mathrm{ou}}}$ is approximately constant as in the white noise case, with a magnitude of $2c\tau_{\mathrm{ou}}^2$. Hence, for a given value of τ_{ou}, the diffusion constant c sets the white noise level for low frequencies.

Chapter 3

Design and experimental setup

This chapter describes how the ideas of the proposal in ref. [5] are realised in our experiment. We work our way from the inner to the outer components of our experimental setup, starting from the SQUID and finishing with the cryostat wiring. Manufacturing processes are explained and design issues and fabrication flaws are highlighted for possible future improvements.

3.1 SQUID chip

In the following, we will discuss the key ideas in the design of our SQUID sensors. Subsequently, their microfabrication process is explained. Finally, we provide illustrations of the resulting devices along with a description of encountered fabrication issues.

3.1.1 Design considerations

In this section, we present some design features of our SQUID samples. The Innsbruck (IBK) SQUID layout was designed by Christian Schneider from our research group with the aid of Matthias Rudolph from the University of Tuebingen, who provided useful input on process capabilities and limitations at the cleanroom of the PTB Braunschweig. Fabrication details can be found in section 3.1.2. Matthias is also responsible for the design of the Tuebingen SQUID layout.

Both designs realise a gradiometer SQUID, see section 2.2.1, in order to suppress the influence of background magnetic fields. Further, in both versions each chip is equipped with 8 SQUIDs. Their dimensions vary in part, with SQUID loops optimized for different spacings to the cantilever chip (IBK design) or designed to obtain different characteristic parameters (Tuebingen design). This is also a precaution with the intention of ensuring that we have working SQUIDs on each chip.

IBK design

The geometry of the IBK SQUID layout is designed to maximize the signal that is picked up from the cantilever. We adopt the key ideas from the proposal in ref. [5]. As described in section 2.4, the quadrupole field is generated by a pair of straight wires in combination with a bias coil. In contrast to the proposal, these wires are placed on the same chip as the SQUID structures. The basic layout of the IBK design is shown in fig. 3.1.

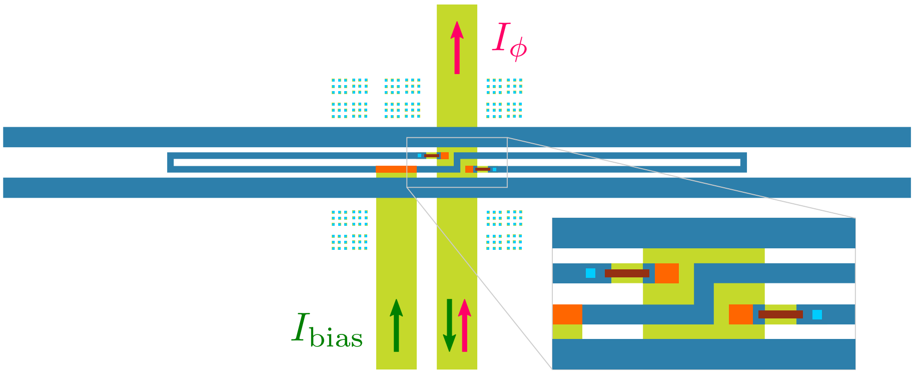

Figure 3.1: Basic IBK SQUID layout. An inset shows the region with the JJs (light blue) in detail. The top and bottom Nb layers are drawn in dark blue and light green, shunt resistors in red and VIAs in orange. Arrows indicate the paths for the SQUID bias current I_{bias} and flux bias I_ϕ.

In the centre of fig. 3.1 we find the gradiometer loop of the SQUID on the top Nb layer. It is enclosed by the quadrupole wires, which stretch across the full width of the chip (only a section is shown) and are also placed on the top layer. The plot inset illustrates the position of the JJs and shunt resistors.

Adjacent to the quadrupole wires, we find multiple arrays of small squares. These represent supporting structures that enable better control of the chemical-mechanical polishing step in the junction fabrication process, see section 3.1.2.

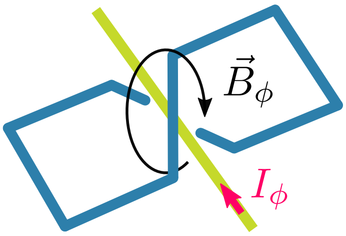

Figure 3.2: Flux biasing.

The SQUID is contacted via the bottom Nb layer. Here we encounter another feature of the design. The bias current I_{bias} and flux bias I_ϕ are applied as indicated in fig. 3.1 and share one of the connecting wires. This reduces the number of bond pads on the chip. The flux bias is induced by the magnetic field of the current carrying wire as indicated in fig. 3.2.

Another feature is presented in fig. 3.3. Half of the SQUIDs are surrounded by an additional loop. It is intended to use this structure for feedback cooling of the mechanical oscillator. This can be achieved by either moving the zero position of the quadrupole magnetic field opposite to the direction of the velocity (direct feedback cooling) or keeping the zero at a fixed point and changing the quadrupole field gradient (parametric cooling). Both require a homogeneous magnetic field that can be changed quickly. The feedback loop can provide this due to its small inductance.

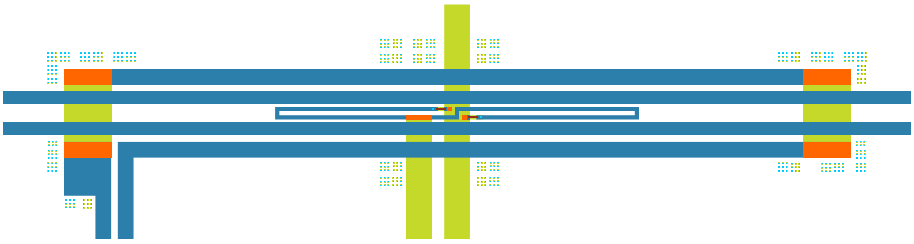

Figure 3.3: IBK SQUID layout with feedback loop.

Tuebingen design

The main purpose of the Tuebingen SQUID design was, to use it as a test bed for some ideas for future SQUID layouts. Even though the dimensions were changed considerably, the design is still suitable for our experiment, albeit not with optimum signal yield. The layout differs in some aspects from the IBK design. Figure 3.4 illustrates the main features of the Tuebingen SQUID.

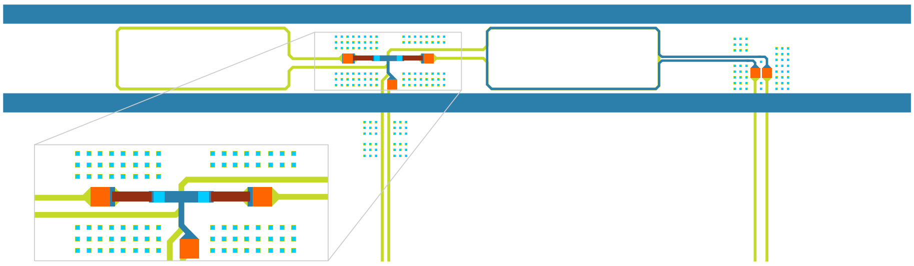

Figure 3.4: Tuebingen SQUID layout. The colour scheme is the same as in fig. 3.1. In the inset, we show the JJ section.

In contrast to the IBK layout, the gradiometer loop is moved to the bottom Nb layer. The loops are much wider, which can lead to a signal reduction if the cantilever is placed very close to the SQUID.

In the Tuebingen design, the SQUID is contacted via four wires, two each for the bias I_{bias} and the flux bias I_ϕ current. Hence, these two circuits are completely decoupled, which however comes with an increased number of bond pads. For the flux bias, a separate loop is placed on top of one half of the gradiometer loop, indicated in fig. 3.4 on the top Nb layer.

The Tuebingen design is equipped with a few additional features that have proven very useful in the the operation of the experiment. In fig. 3.5 we show the complete layout of one SQUID on the Tuebingen chip.

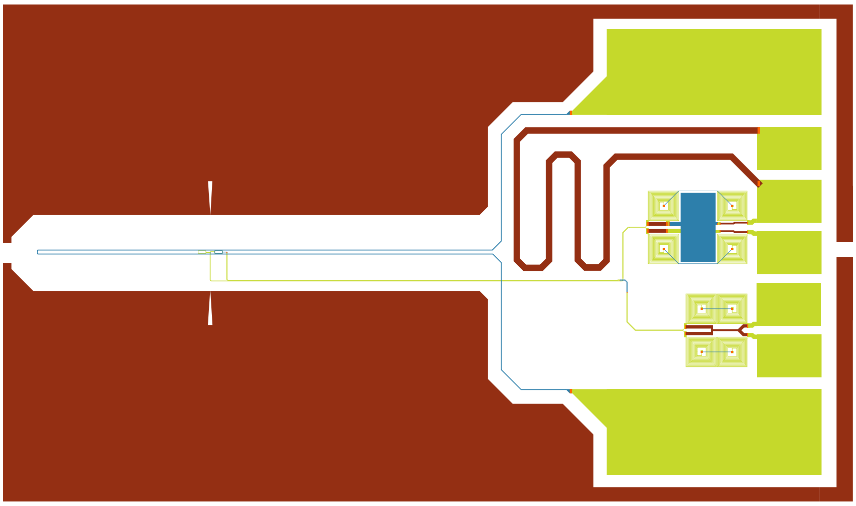

Figure 3.5: Complete Tuebingen SQUID layout with auxiliary features. Red structures are placed on the resistive AuPd layer and dark blue and light green elements on the SC top and bottom Nb layer.

The red patches in fig. 3.5 that surround the structure represent thermalisation pads, where left out marks indicate the SQUID position. On the right, the two large bond pads are connections to the quadrupole line, the narrow blue loop in the centre. The additional red meander shaped line is a resistive heater, that can be used to warm up the SQUID beyond the SC transition temperature if trapped flux is an issue. Connections to the SQUID are established via the first four small bond pads from the bottom, with the lower two for the flux bias and the upper two for the bias current. Each of these lines is equipped with an on-chip RF filter [17], used to reduce high frequency noise of the control currents. Their layout and current transfer function $G_\mathrm{I} = |I_\mathrm{out}/I_\mathrm{in}|$ is described in fig. 3.6.

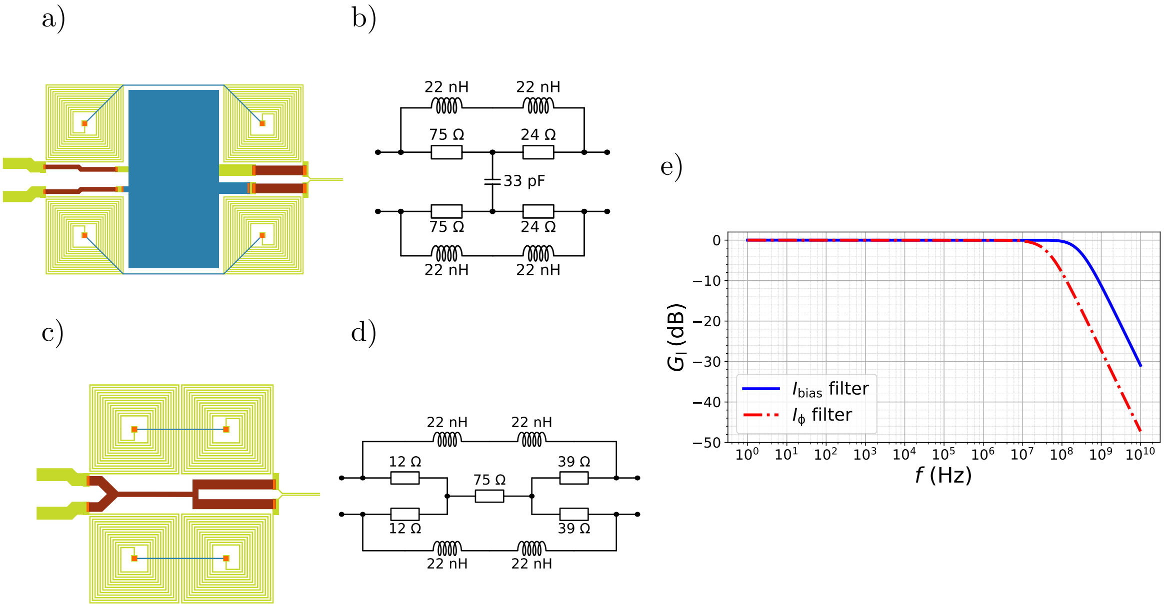

Figure 3.6: Tuebingen SQUID RF filters. Figures a) and c) show the layout and b) and d) the corresponding equivalent circuit of the bias and flux bias current filters, respectively. The colour scheme is identical to fig. 3.5. In fig. e), we plot the Bode diagram of the current transfer functions G_I.

The filters have corner frequencies of approximately 300 MHz for the bias and 40 MHz for the flux bias current. These values are obtained, by modelling the SQUID in the form of a 15 Ω load at the filter output and the flux bias loop as a short.

3.1.2 Fabrication process

Our SQUID samples were produced at the cleanroom facility of the PTB Braunschweig. They are the result of a collaboration with the group of Dieter Kölle at the University of Tuebingen and were designed by Matthias Rudolph, whose PhD thesis [17] gives a detailed description of the manufacturing process in chapter 3. The most important fabrication steps are summarised in the following.

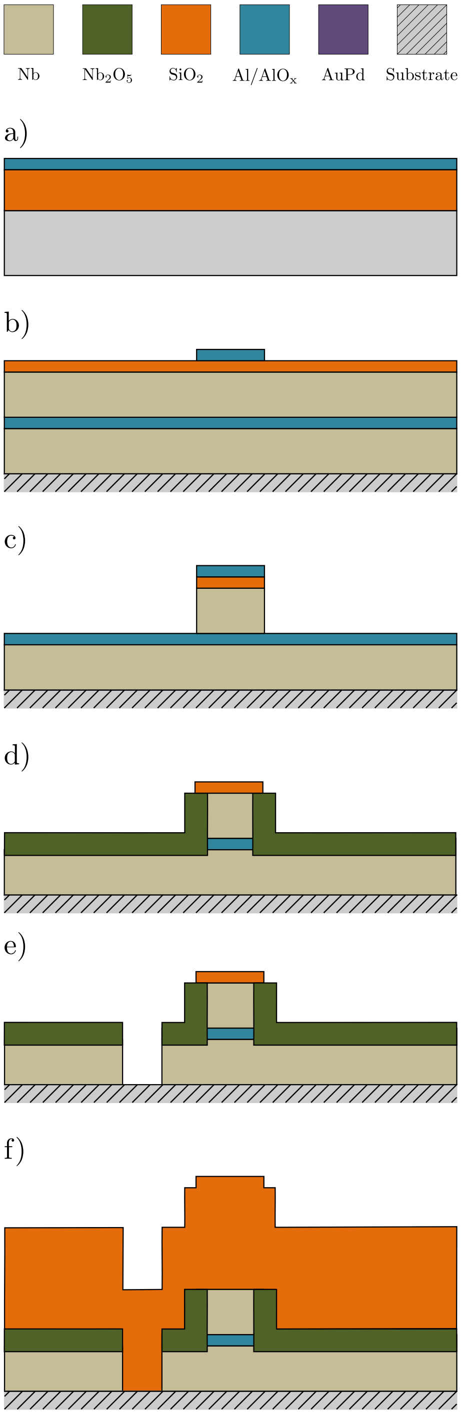

The process starts with a 3" Si wafer with a thickness of 350 µm that was thermally oxidised to create a 300 nm SiO_2 isolation layer on its surface. On top of that, a 30 nm Al_2O_3 etch stop layer is deposited. This stack (a) is labelled as *Substrate* in fig. 3.7.

Next, the junction Nb/Al-AlO_x/Nb trilayer (b) is deposited by DC magnetron sputtering. The Nb layers have a thickness of 150 nm, interrupted by a 10 nm thick Al layer. The latter is oxidised in an intermediate step to form an 1-2 nm AlO_x barrier on the surface. Subsequently, a 100 nm SiO_2 film and a 30 nm Al layer are deposited on top of the trilayer by plasma enhanced chemical vapor deposition (PECVD) and thermal evaporation, which are used as masks. The Al is patterned by electron beam lithography (EBL) and defines the junction.

The SiO_2 and the top Nb layer are etched (c) by reactive ion etching (RIE) in CHF_3 and CF_4, respectively, which automatically stops at the Al layer. An ion beam etch (IBE) with Ar ions finally strips the Al mask.

The SiO_2 layer is used as a mask for an electrochemical anodization (d) that oxidises the Nb.

This improves the junction properties and compensates a growth of the junction size in the prior etching step.

The bottom Nb layer is patterned by EBL and a subsequent RIE using SF_6 (e), which etches both the Nb and the Nb_2O_5.

Another PECVD step buries the junction under a 600 nm thick layer of SiO_2 (f), that isolates the top from the bottom Nb layer.

This is followed by a chemical-mechanical polishing (CMP) step (g) used to planarize the structure. Careful timing is essential, because the process has to stop as soon as the top Nb layer is released. Typically, a removal of less than 50 nm of Nb can be achieved.

Next, the vertical interconnect access (VIA) openings are patterned by EBL, followed by an ICP-RIE (inductively coupled plasma RIE) with CHF_3 (h), that removes the SiO_2 and Nb_2O_5.

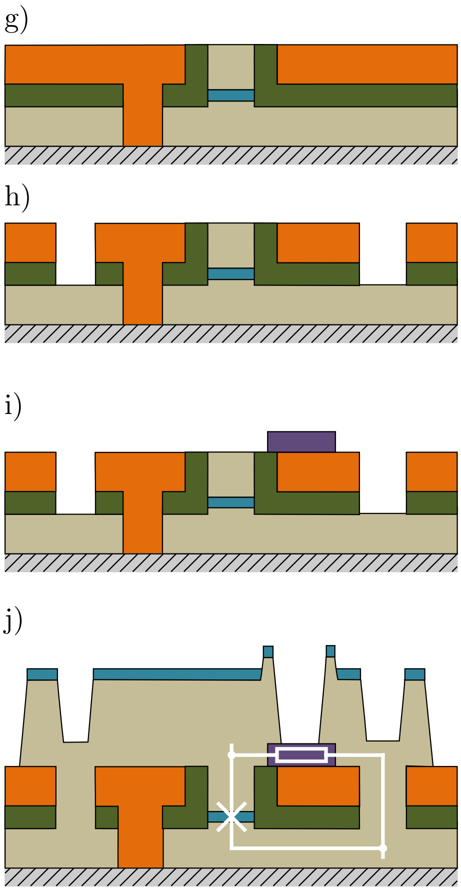

Figure 3.7: SQUID fabrication process flow diagram. With kind permission adapted from ref. [17].

Patterns for the AuPd shunt resistors are generated by EBL. The metal is deposited by DC magnetron sputtering with a prior deposition step of $2-3$ nm Al that acts as adhesion promoter. The AuPd structures are released by a lift-off process (i).

In a last step, the thick 750 nm top Nb layer is deposited (j) by DC magnetron sputtering, followed by a 300 nm Al mask. The latter is patterned by EBL and used to define the structure of the top Nb layer, etched in an SF_6 RIE. This e.g. removes the Nb on the top layer that would bypass the AuPd shunt resistor. An equivalent circuit diagram (white lines in fig. 3.7 (j)) indicates the position of the relevant JJ elements in the final structure.

3.1.3 Inspection and microfabrication flaws

The manufacturing of our SQUID samples is very demanding and requires a complex and lengthy fabrication process that usually takes multiple weeks. Each processing step underlies certain variations, even if the technician operates the machine properly. Therefore, a detailed inspection of the chips is essential to identify possible flaws in the microfabrication process. This can save time in debugging the setup and provides valuable information for improvements to future designs.

IBK design

In a first inspection with an optical microscope, illustrated in fig. 3.8, we cannot identify any major defects of the structures. All patterns appear well defined and there are no apparent residuals from the etching and lift-off processes visible. We can discriminate between top and bottom Nb layer by their colour difference and one can identify VIAs and shunt resistors.

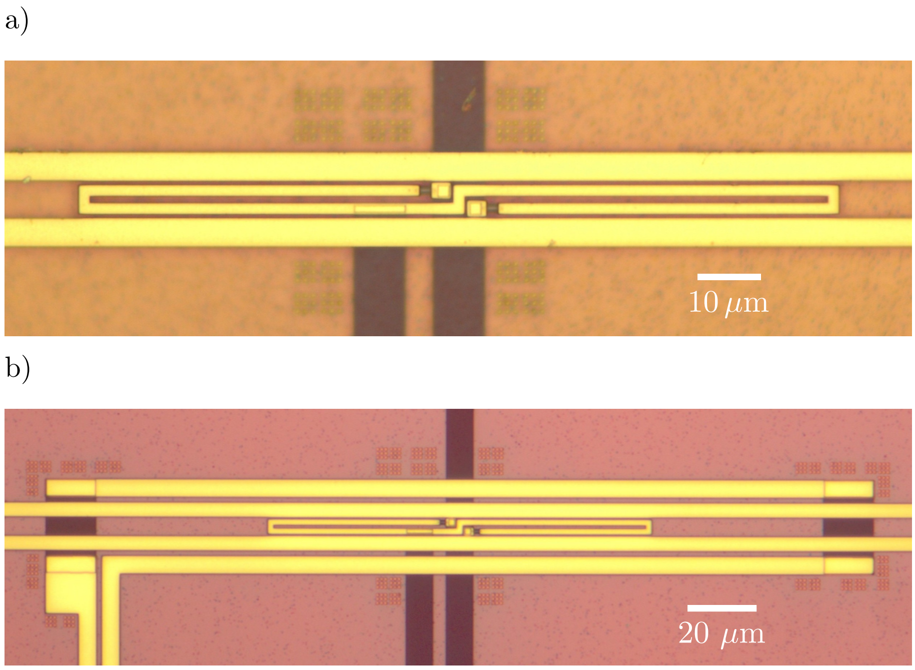

Figure 3.8: Optical microscope inspection of IBK SQUID samples. Fig. a) shows a basic IBK SQUID layout and fig. b) a SQUID with feedback loop. Compare figs. 3.1 and 3.3 for details on the design.

Even though the optical inspection is promising, the experiment reveals that our samples are corrupted. We are not able to find a properly functioning device on two sample chips with 8 SQUIDs each. Instead, the SQUIDs appear to be shorted. A simple optical microscope does not provide the necessary resolution to rule out possible unwanted connections. Hence, we switch to a scanning electron microscope (SEM) to examine the structures in more detail. Our findings are shown in fig. 3.9.

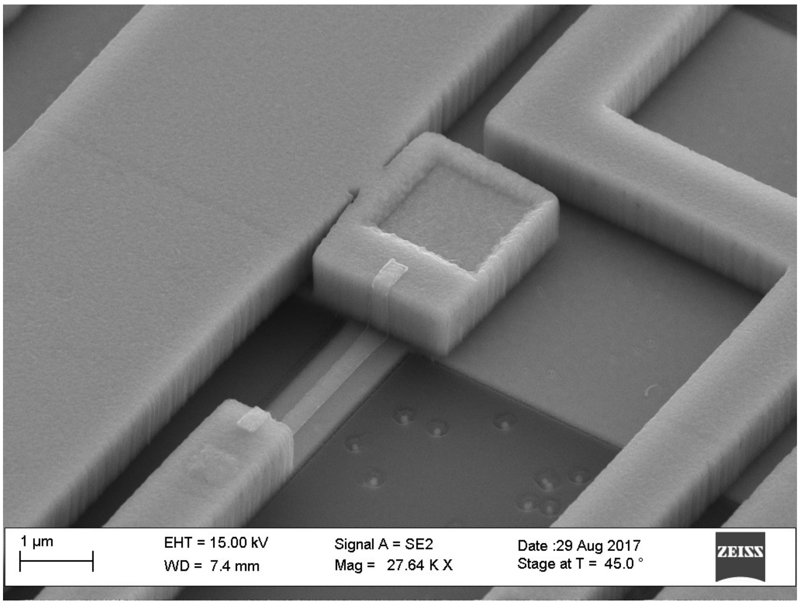

Figure 3.9: SEM inspection of an IBK SQUID sample. The plot shows the central section of the gradiometer. In the middle, we see the VIA that connects the top and bottom Nb layer, indicated by the large square-shaped recess. Adjacent, we find the thin strip of the shunt resistor that bridges the gap between VIA and SQUID loop. At the bottom end of the resistor, we can identify a small bump on the top Nb layer, which represents the JJ. The large structure on the left is the quadrupole wire.

We can see in fig. 3.9 that the VIA structure is connected with the quadrupole wire, which is clearly a flaw in the microfabrication. Such defects are observed for every VIA in the centre of a SQUID structure. The remaining connection is likely the result of an issue in the final EBL step, which did not open the Al mask properly for the subsequent SF_6 etch. We suspect connections of this kind to be responsible for the shorted SQUIDs.

Tuebingen design

The Tuebingen and IBK samples are both manufactured in the same fabrication run. Also the minimum spacing in the design is comparable. However, the process performance can vary noticeably depending on the position of the sample on the wafer. Hence, it is not guaranteed that the Tuebingen sample suffers from the same problems as the IBK sample. We repeat the inspections from the prior section for the Tuebingen chip. The optical microscope images are shown in fig. 3.10.

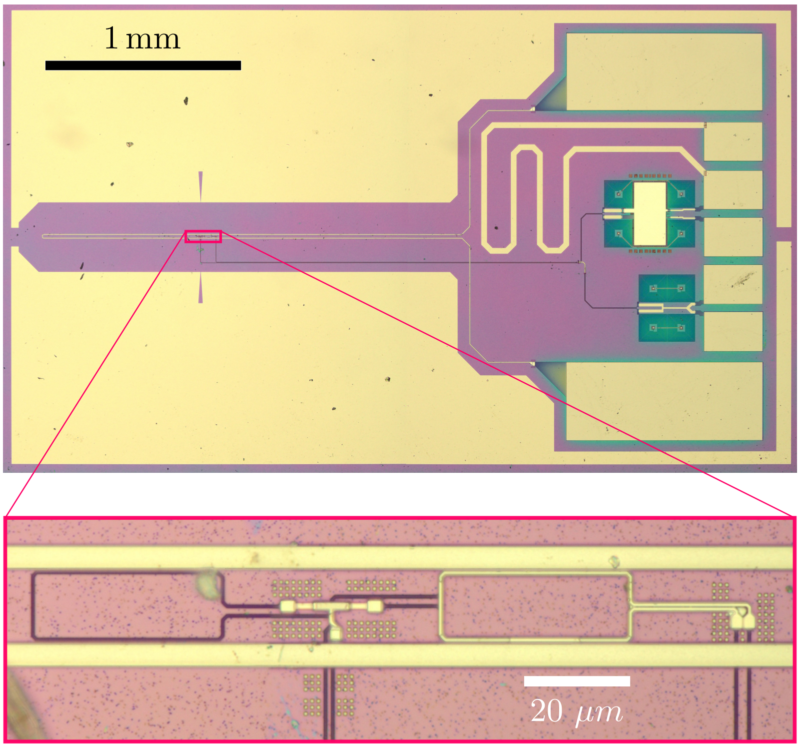

Figure 3.10: Optical microscope inspection of Tuebingen SQUID samples. The main figure illustrates the auxiliary features of the design, see fig. 3.5 for comparison. In the inset on the bottom, a close-up of the SQUID is shown, c.f. fig. 3.4.

As in the case of the IBK sample, the first inspection does not indicate any major issues in the microfabrication. We change to the SEM for a detailed check for possible defects. The result is illustrated in fig. 3.11.

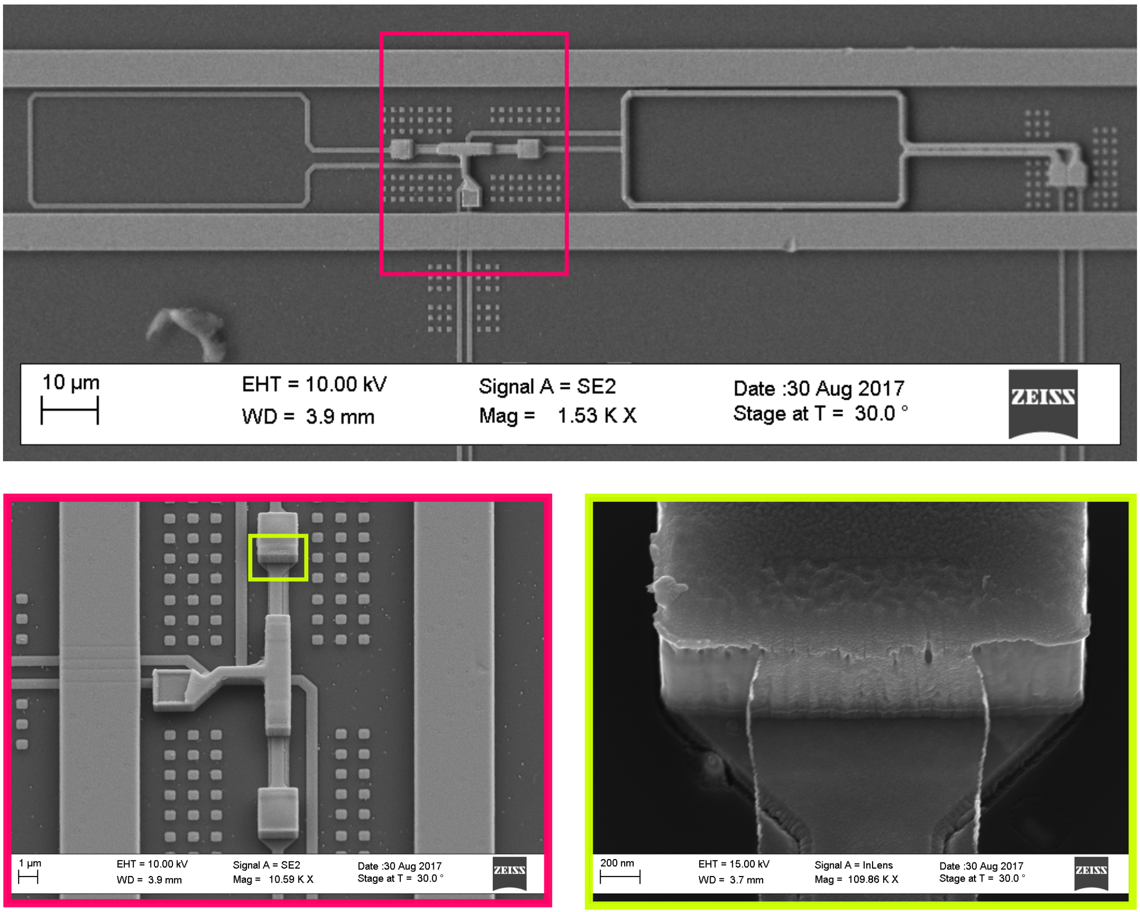

Figure 3.11: SEM inspection of a Tuebingen SQUID sample. The top plot shows an overview of the SQUID. In the bottom row, we show close-ups of the JJ section (pink box, rotated by 90°) and the step coverage of the shunt resistor (green box). The JJs can be identified by small bumps in the top Nb layer.

Most SQUIDs that we tested on two Tuebingen chips are fully functional. The close-ups in fig. 3.11 prove that there are no unwanted connections. Also the step coverage of the shunt resistor is satisfying, despite the thick 750 nm Nb top layer. The resistance should therefore be close to the nominal value.

Besides those positive findings, we also identify a manufacturing flaw in the Tuebingen samples. We can see from fig. 3.12 that the space between the feed lines of the flux bias loop is not fully cleared. This is a consequence of a too narrow line spacing of nominally 300 nm. The SF_6 etch cannot clear the Nb either due to residuals from the Al mask or other contaminations that can lead to micro-masking. The result is similar to the case of the IBK SQUID. All flux bias loops on the two tested chips are shorted and can not be used for flux tuning. The SQUID is however not affected by this flaw, as the gradiometer loop on the bottom Nb layer is isolated from the flux bias loop. As described in section 5.1.2, we also find a workaround for flux tuning, represented by the bias coil. The large inductance of the coil however prevents the use of a standard SQUID readout technique, the so called flux-locked-loop (FLL), which is a substantial drawback for our experiment.

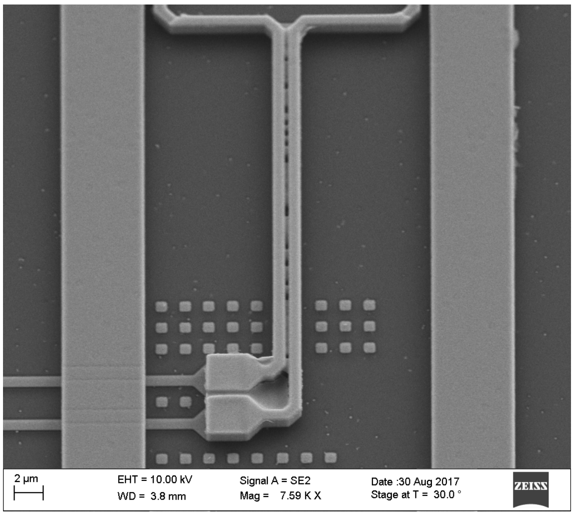

Figure 3.12: SEM image of a shorted flux bias line on a Tuebingen sample.

3.2 Cantilever chip

In this section, we first explain the microfabrication process of our cantilever chips. After that, we describe our attempt of depositing magnetic nanoparticles on the cantilever tip. The section concludes with illustrations of the alignment procedure of cantilever and SQUID chip.

3.2.1 Fabrication process

The cantilever chips for our experiment result from a collaboration with Michael Trupke from the University of Vienna (UNIVIE). They were fabricated at the "Zentrum für Mikro- und Nanostrukturen (ZMNS)" of the Vienna University of Technology (TU Wien). In the process flow in fig. 3.13, the strip on the cantilever tip is made of the SC material Nb as proposed in ref. [5]. For our first iteration of the experiment we however used process development samples, equipped with a Cr strip instead. Besides that, the process flow is identical.

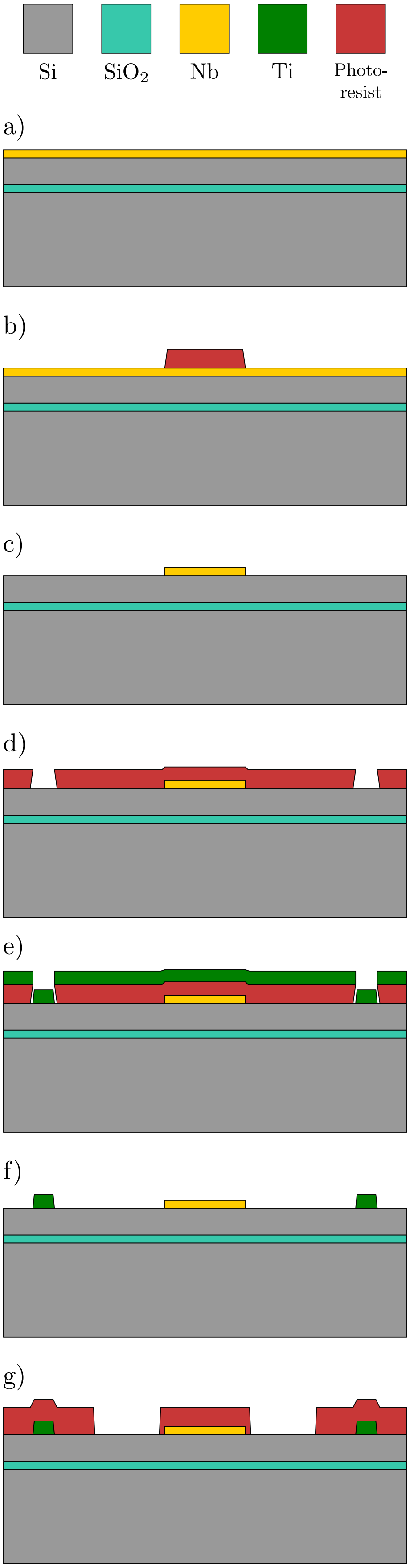

The starting point is a silicon-on-insulator (SOI) wafer, which consists of a Si handling layer with 400 µm thickness, a 1 µm SiO_2 insulating layer and a Si device layer with a thickness of 4 µm. In a first step, the metal coating (a) of 200 nm is done in-house in an electron beam evaporator for Cr or externally in the case of Nb.

The pattern of the Nb strip on the cantilever tip is defined by photolithography (b) with a positive resist.

It is subsequently etched in an RIE with SF_6 (c) and the photoresist is stripped.

A second photolithography step (d) is used to define the position of the Ti pillars, that act as spacers between the cantilever and SQUID chip. Here, a negative resist is used in order to create negative sidewall profiles for the later lift-off process.

The 1 µm thick Ti layer is deposited (e) by e-beam evaporation.

Next follows a lift-off process (f) by immersing the wafer in acetone and applying ultra-sound to release the excess Ti.

After finishing the patterning of the metal structures, the cantilever shape has to be defined on the SOI wafer. For this purpose, another photolithography step (g) on the device layer defines the rectangular U-shaped opening for the cantilever beam.

The Si device layer is etched in an RIE Bosch process (h) with SF_6. With this, one achieves

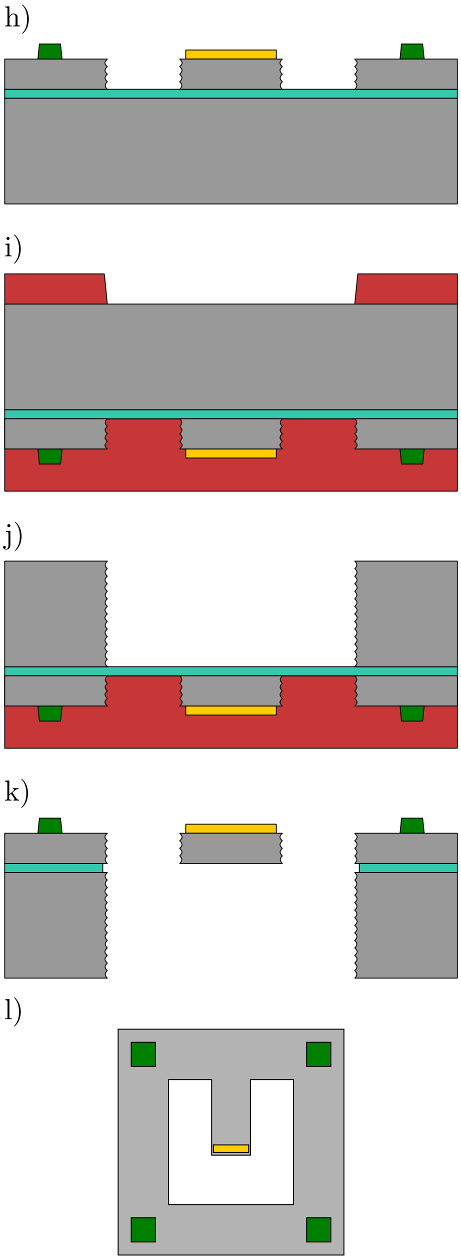

Figure 3.13: Cantilever fabrication process flow diagram.

vertical sidewalls with the characteristic scallops of the Bosch process for the cantilever profile. The etch process automatically stops at the SiO_2 layer.

Next, the device layer is coated in photoresist to protect the sensitive structures. The back side of the wafer, i.e. the Si handling layer, can now be patterned. To this end, a photolithography step (i) defines the windows for the cantilevers.

Another RIE Bosch process step (j) with SF_6 is used to etch the structures into the handling layer.

In a final process step, the photoresist that protects the device layer is stripped and the wafer is subsequently immersed in an HF solution. This wet etching process removes the SiO_2 insulation layer (k) and releases the cantilever beam.

Figure 3.13 (l) illustrates the resulting device in top view. Attached to the tip of the cantilever beam is the SC Nb strip and the Ti spacers are placed outside the corners of the opening. The wafer is finally diced into chips with 8 cantilevers each.

3.2.2 Nanoparticle application

The cantilever samples we received from the TU Wien are equipped with Cr strips. This metal was chosen for testing purposes to check the alignment of the lithography steps. Cr is however an anti-ferromagnet. Hence, its spin magnetic moment vanishes, which is an issue for our detection schemes, see sections 5.4.1 and 5.4.2.

Nonetheless, the fact that Cr is a good conductor might result in a detectable signal. This is enabled by the eddy-currents that are induced when the metal experiences a changing magnetic field due to the cantilever oscillation.
We do not want to solely rely on this mechanism for generating a cantilever signal. Therefore we try to deposit material that can be magnetised on a cantilever sample that does not have any Cr applied. We choose magnetite Fe_3O_4 nanoparticles, which can have a large magnetisation due to their superparamagnetic properties [18]. An estimation of the achieved magnetic moment is presented in section 5.4.1.
The nanoparticles come in an aqueous solution. We further dilute the liquid to reduce the nanoparticle concentration and use a nebulizer ("OMRON U22 MicroAIR") to dispense it on the chip. To this end, we mask the regions of the chip that should not be covered with nanoparticles. The result is illustrated in fig. 3.14.

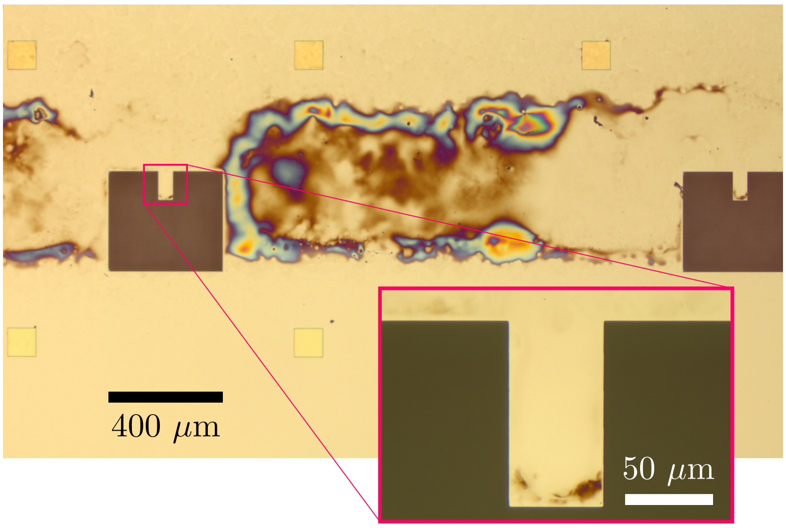

Figure 3.14: Cantilever chip with magnetic nanoparticles. In the main plot we see a section of the chip, with the square-shaped Ti pillars arranged around the windows for the cantilever beams. The inset shows a close-up of the cantilever that is selected for our experiment.

We can see that the improvised deposition is not confined to the cantilever tip, but a large portion of the nebulized nanoparticle solution accumulates in the region between the cantilever windows. On the other hand, the beam remains mostly uncovered and only on the tip we find a region with high nanoparticle concentration, which meets our intention.

3.2.3 Assembly/Alignment procedure

Our experimental setup requires a relatively accurate alignment of cantilever and SQUID chip. The SC strip on the cantilever should be centred between the quadrupole lines and aligned to one of the loop halves of the SQUID gradiometer, ideally with an accuracy better than 10 µm.

We use a linear translation stage to achieve those positioning accuracies. As indicated in fig. 3.15, a piece of standard optical fibre is glued to the cantilever chip. The cladding is stripped from the bottom of the fibre, such that we can easily break it with a wire cutter after the alignment procedure. Therefore, we can pick up the chip via the attached fibre and move it to the desired position with the translation stage.

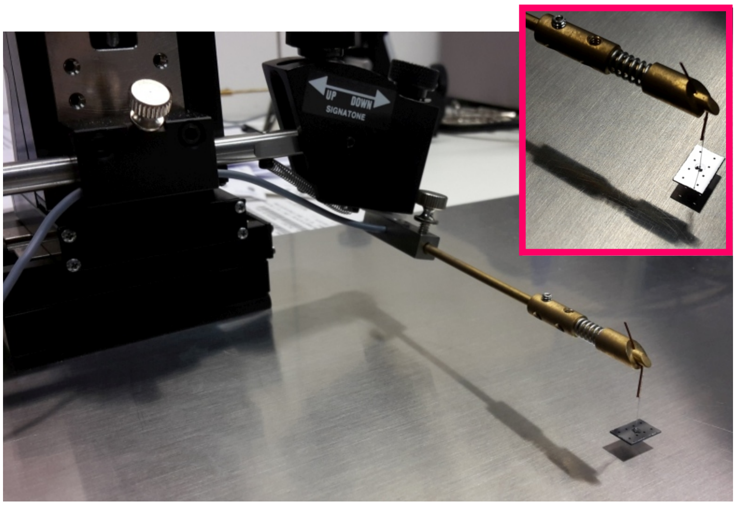

Figure 3.15: Translation stage for the alignment of the cantilever chip. In the inset, we can see the windows for the cantilever beams, which are used as viewports for the alignment procedure.

The alignment procedure is performed under an optical microscope. We use the opening for the cantilever beam to see the SQUID on the chip below. In this way, we achieve a sufficing alignment accuracy, as indicated in fig. 3.16.

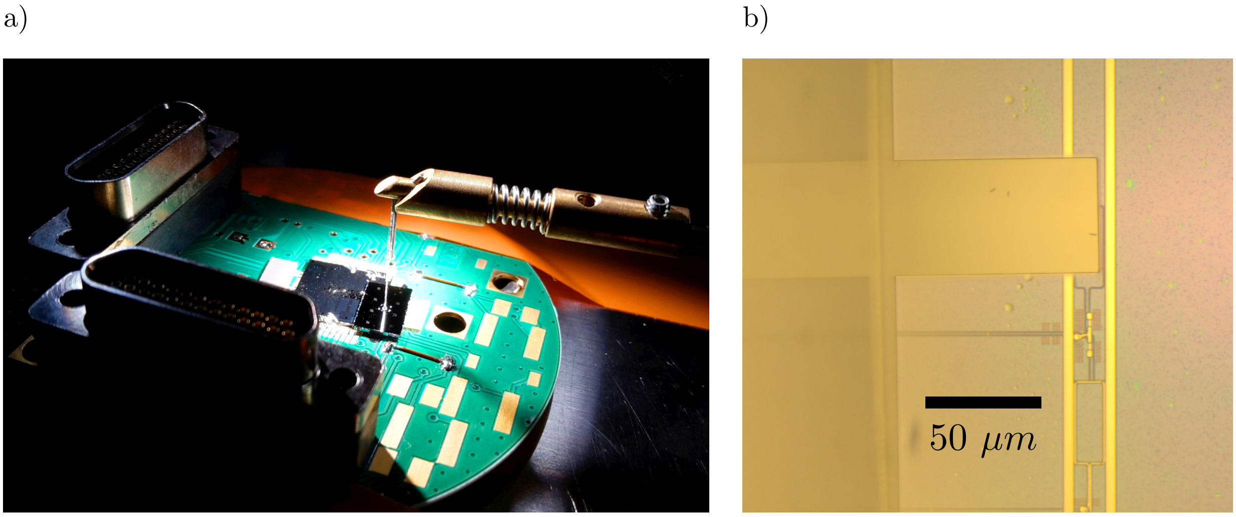

Figure 3.16: Cantilever alignment procedure. In fig. a) we show the arrangement for aligning the cantilever to the SQUID chip, which is mounted on the PCB. Fig. b) illustrates the achieved alignment accuracy.

When the alignment is satisfying, we use the fibre to carefully apply some pressure on the chip to hold it in place. The cantilever chip is finally glued to the PCB using small drops of "Stycast 2850 FT" epoxy. We let the epoxy rest for 1-2 h before we apply it, to increase its viscosity and thereby prevent it from creeping into the gap between the two chips. The Stycast has to cure for approximately 12 h.

3.3 Printed Circuit Board

The connection to our SQUID chip is provided by a printed circuit board (PCB). To reduce the effect of resistive heating, we use 50 µm Al wire to bond the chip to the PCB. For the same purpose, the cross-section of the Cu tracks on the circuit board is designed as large as possible. We use 25-pin Micro-D connectors for the signal lines of 4 SQUIDs and screw terminals for the high current connections to the quadrupole lines. A sketch of the PCB design is shown in fig. 3.17 along with pictures of the wire bonded chip.

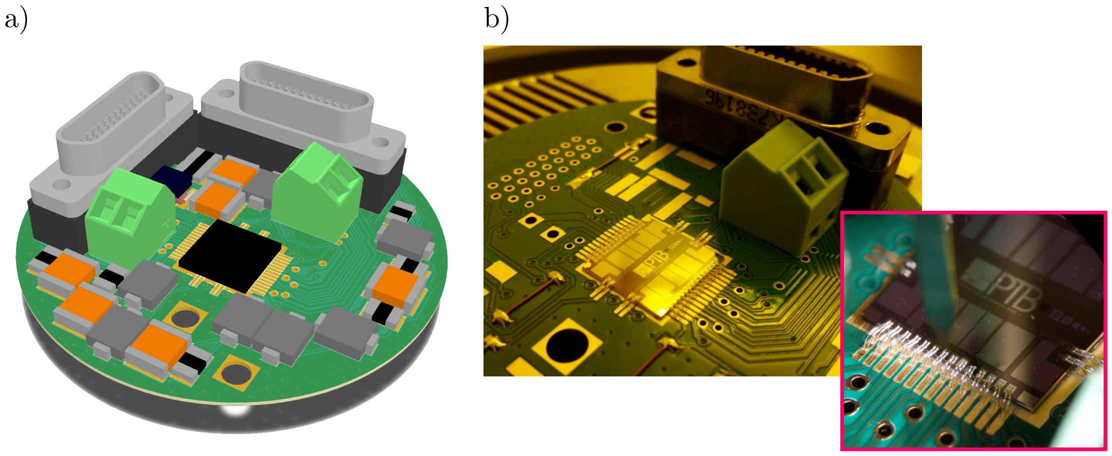

Figure 3.17: PCB design and wire bonding. Fig. a) shows a CAD drawing of the fully equipped PCB. In b), we see the chip after it was wire bonded to the PCB.

It was further intended to equip the PCB with filters for the different SQUID signals, as indicated in fig. 3.17 a). This is essential for the IBK design, due to the missing on-chip RF filters. However, as discussed in section 3.1.3 the IBK samples could not be used in the experiment. Consequently, no filters were used in the first iteration with the Tuebingen samples. The filter designs are nonetheless presented in fig. 3.18 as a reference for possible later use.

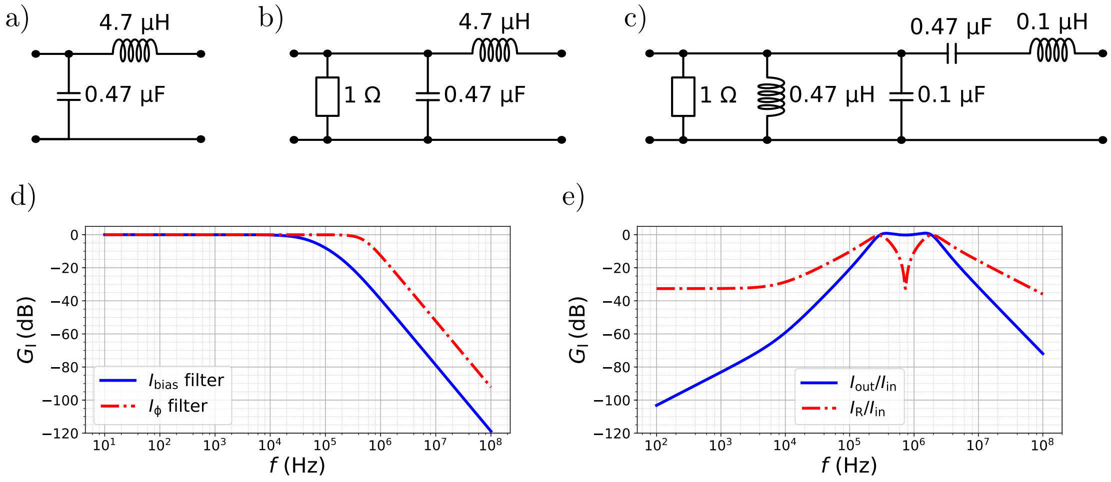

Figure 3.18: SQUID filters for IBK design. Fig. a) and b) show low pass filters for the bias I_{bias} and flux bias current I_ϕ, respectively. In c), a bandpass design for the feedback loops is illustrated. Plots d) and e) show Bode diagrams of the current transfer function $G_{\mathrm{I}} = I_{\mathrm{out}}/I_{\mathrm{in}}$. In d) we compare the I_{bias} and I_ϕ filters. Fig. e) shows G_{I} for the bandpass filter and the component $I_{\mathrm{R}}/I_{\mathrm{in}}$ of the shunt resistor.

The transfer functions in fig. 3.18 are obtained with a shorted output for the filters in b) and c) that represents the SC loops and with a $8.5\,\Omega$ load in a), which models the SQUID. With the cryogenic temperatures of our setup, we are limited to passive components for the filter designs. We choose to work with capacitors with NP0/C0G dielectrics and inductors with molypermalloy powder (MPP) core, because they retain their nominal capacitance [19] and inductance [20] also at cryogenic temperatures.

The bias filter is designed to achieve an as low as possible corner frequency with the available components to ensure a stable working point. For the flux bias filter, we choose a corner frequency in the range of the mechanical frequency to allow the use of the FLL readout. Finally, the mechanical frequency should be in the pass band for the bandpass filter, such that direct feedback cooling is possible. A certain bandwidth should be available for quicker response and ideally the dip in the $I_\mathrm{R}/I_\mathrm{in}$ curve in fig. 3.18 e) should be tuned to the mechanical resonance frequency to prevent warming up the cryostat.

3.4 Bias coil

With the bias coil, we intend to create large magnetic field strengths that should be homogeneous across the area of the SQUID chip. This requires large currents and winding numbers. We use thin superconducting NbTi wire to combine both. Our coils are wound on a lathe, see fig. 3.19, and the windings are coated with "Stycast 1266" epoxy after each layer. The latter is optimised for cryogenic applications and provides good thermal conductivity at low temperatures. After curing, it also serves as protection of the fragile insulation of the SC wires.

The coil body has a height of $h = 9\,\mathrm{mm}$ and an inner radius of $r_\mathrm{in} = 5\,\mathrm{mm}$. Together with the windings, the outer radius results in $r_\mathrm{out} = 8.5\,\mathrm{mm}$.

In the course of the experiment, we fabricated three different coils. A first attempt with single SC filament wire of $67\,\mu\mathrm{m}$ thickness results in a winding number of $N = 5240$. The coil wire however shows a connection to the coil body and the SC breaks down at too low currents. These issues are attributed to the fragility of the wire. During the winding process it is put under tension, which presumably causes the SC filament to break and damages the wire insulation at sharp corners. Consequently, we switch to a thicker 254 µm multi-filament wire with 54 SC filaments for a proof-of-principle attempt. A second coil with $N = 440$ turns is hand-wound and is able to withstand the desired high currents, as explained in section 5.2.2. In a final iteration, we use a 127 µm thick wire with 54 SC filaments. A third coil with $N = 1680$ turns is wound on the lathe. The fragile insulation is damaged in the winding process, which can however be repaired by also coating the coil body with Stycast epoxy.

The wires that leave the coil are finally twisted to a pair and coated with "GE varnish" for better protection. They are connected to the dedicated high current lines, described in section 3.5.2.

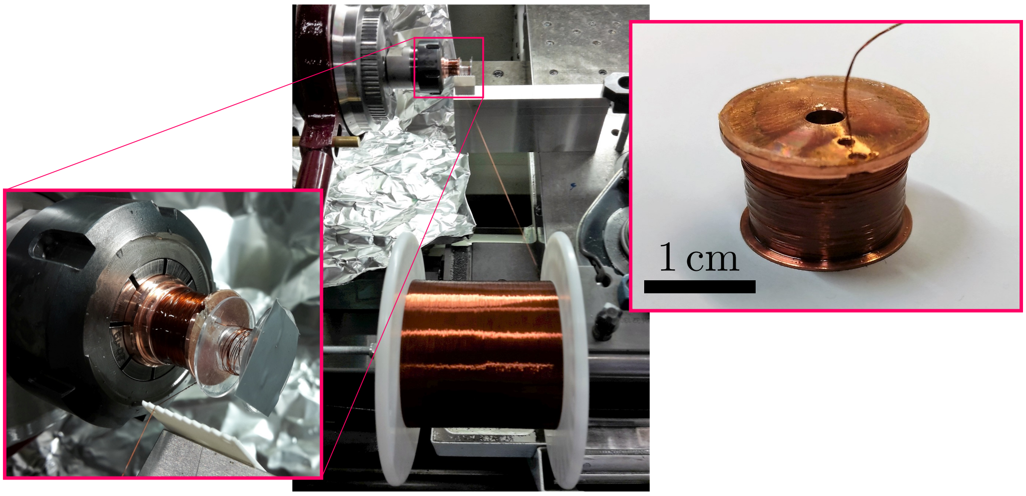

Figure 3.19: Coil winding process and resulting bias coil. In the inset, we show the first generation bias coil.

3.5 Sample mount and electronic connectivity

This section describes the remaining components of our experimental setup. They provide the connection to our SQUID samples and take care of the alignment of the individual elements and the thermalisation with the cryostat.

3.5.1 Sample holder and magnetic shielding

The PCB is placed in a copper box for electromagnetic shielding. At the same time, this box is part of the connection between cryostat plate and sample. Therefore, when mounting the sample, the contact area of the joints should be cleaned with sandpaper and coated with "GE 7031 low temperature varnish" or "Apiezon® high vacuum N grease" for better thermal conductivity.

The copper box is suspended from a T-beam that also carries the bias coil, see fig. 3.20. Box and T-beam are finally bolted to the cryostat via an adapter plate made of copper.

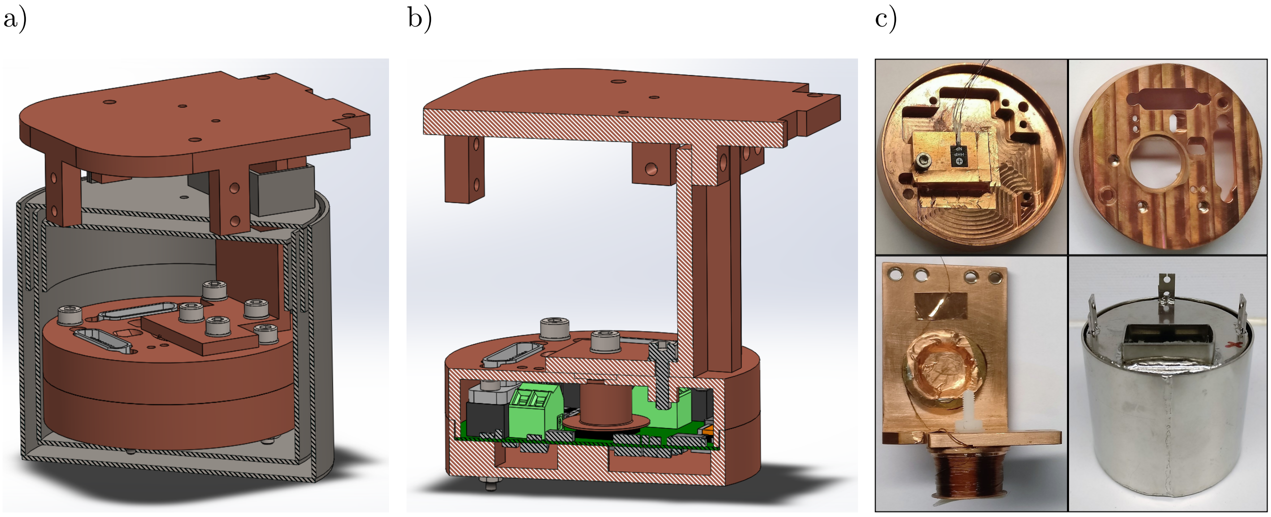

Figure 3.20: Sample box and magnetic shield. Fig. a) and b) show CAD drawings of the sample holder in sectional view. In a), we can see the magnetic mu-metal shield that surrounds the copper box and in b) the assembly with the PCB is illustrated. Plot c) shows pictures of the individual components.

As illustrated in fig. 3.20 a), the sample box is enclosed in a magnetic shield. The latter is manufactured of so called mu-metal. This is a material with an exceptionally high permeability in the range of $\mu_\mathrm{r} = 7 \times 10^4$ for static fields [21]. Due to that, external magnetic fields are attracted by the shield and effectively guided around the sample box. Our shield is composed of two layers of 1 mm mu-metal and should achieve a magnetic field suppression of $B_\mathrm{int}/B_\mathrm{ext} < 1 \times 10^{-5}$.

In a final step of the fabrication, the shields are annealed in a H-atmosphere. After that, they have to be treated with care, as they are highly sensitive to shock or stress. Otherwise, the high permeability properties can be lost.

3.5.2 Wiring scheme

In our experiment, we have to supply the quadrupole line and bias coil with currents in the range of 1 A. The structures on our sample chips are all fabricated with Nb, which can achieve supercurrent densities $j_c > 1 \times 10^{11}\,\mathrm{A/m^2}$ [22]. For 1 A we require $j_c = 3.3 \times 10^{11}\,\mathrm{A/m^2}$. As discussed in section 5.3, a fabrication flaw prevents a measurement of the critical current for the quadrupole line on our chip.

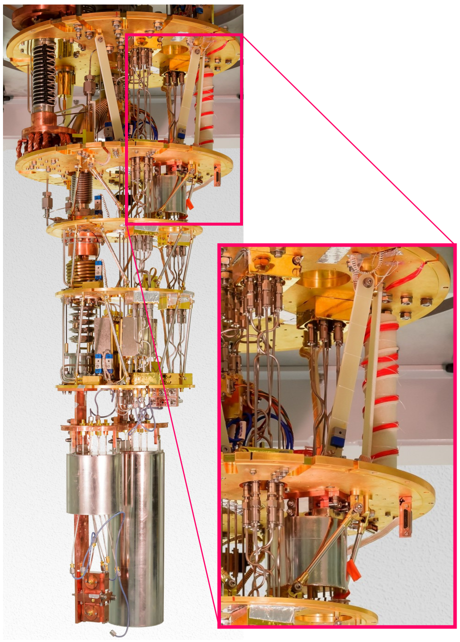

Figure 3.21: Cryostat wiring. Here, the sample box is placed on the 4 K plate, as can be seen in the bottom of the inset.

Handling such high currents in a cryostat environment is a delicate task. The normal conducting part of the cryostat wiring requires large cross sections, which presents an issue for maintaining the thermal isolation of the individual cryostat plates. We equipped our cryostat with a set of 10 dedicated high current lines, represented by the red wires in fig. 3.21. The lines are thermally anchored by large copper blocks and span the section from the cryostat top to the 4 K PT2 stage. Despite the increased thermal load on those plates, we are able to reach a final base temperature of roughly 15 mK without a noticeable slowdown in the cool-down procedure.

An illustration of the full wiring scheme of our experimental setup is provided in fig. 3.22. Two pairs of high current wires are used to supply the bias coil and quadrupole line. The section from the PT2 plate to the sample on the 1 K still plate is connected by SC NbTi loom wires.

Bias and flux bias lines on the SQUID chip are connected by Cu loom wires with 12 twisted pairs from top to PT2. The remaining section to the still plate is wired with SC NbTi looms.

Outside the cryostat, we use a triply shielded cable with 12 copper wire pairs. The cable connects the SQUID lines to a breakout box, from where we then use BNC cables for the connection to current sources (Keysight B2902A SMU) and measurement devices (LabJack T7-PRO DAQ board and R&S FSV spectrum analyser). We use low pass filters to reduce RF noise on the SQUID lines. For the measurements in chapter 5, the cut-off frequencies of these filters are 1 kHz for the bias current and 5 kHz for the coil current (Thorlabs EF110 and EF114). The flux bias loop and quadrupole line can not be used with our samples, see sections 3.1.3 and 5.3.

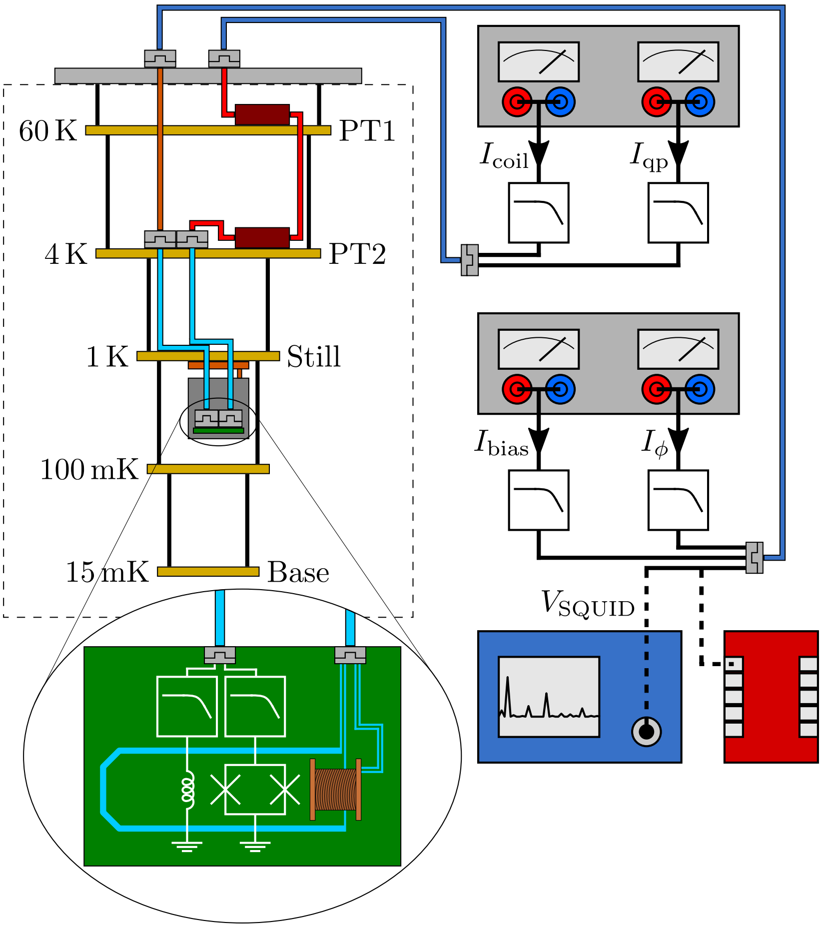

Figure 3.22: Simplified schematic of the experimental setup. The dashed contour marks the interior of the cryostat and on the bottom a sketch of the connections to PCB and bias coil is shown. Interfaces between wire sections are indicated by grey rectangles. The copper blocks for thermalisation of the high current lines are placed on the PT1 and PT2 stage, shown in dark red. We use current sources to supply the SQUID bias and coil current and analyse the SQUID output voltage V_{SQUID} with either a DAQ board (red) or a spectrum analyser (blue).

Chapter 4

Numerical simulations

We use a numerical approach to model characteristic curves of the SQUID. This chapter first discusses, how we can simulate the Johnson current noise from section 2.2.2. Later, we demonstrate the influence of various SQUID parameters on the I-Φ-V curve.

The results are finally used in section 5.1.4, where I try to fit the simulation model to an actual characteristic curve of one of the SQUIDs in our experiment. This will enable us to extract valuable information about its characteristic parameters and give us some insights in imperfections of the fabrication process.

4.1 Noise modelling

In this section, we are going to develop a practical realisation of the noise processes in section 2.5 that we can use for our numerical SQUID simulations. The procedure closely follows the descriptions in ref. [15], but a more general version of the Ornstein-Uhlenbeck noise process according to ref. [16] is implemented. A verification of the properties of our noise modelling is presented at the end of each section.

4.1.1 Gaussian white noise

We want to determine how a variable evolves according to a SDE that is subject to white noise. Therefore, we have to express the noise integral of eq. (2.5.4) in a way, that it can be implemented in a numerical simulation. If we realise that the noise integral describes a Gaussian process, we can fully describe it with the two parameters mean and auto-covariance (see eq. (2.5.5)). For discretised time steps $t_i = i \cdot h$ in our simulation, we obtain

$$\langle w_{\mathrm{w}}(t_i) \rangle = 0, \tag{4.1.1}$$

$$\operatorname{cov}\left[w_{\mathrm{w}}(t_i), w_{\mathrm{w}}(t_j)\right] = Dh\delta_{ij}. \tag{4.1.2}$$

This behaviour can be modelled by a unit normal random variable u_i with $\langle u_i \rangle = 0$ and $\langle u_i u_j \rangle = \delta_{ij}$, i.e. $u_i \in \mathcal{N}[0,1]$. The noise integral for a Gaussian white noise process can hence be described by the simple relation

$$w_{\mathrm{w}}(t_i) = \sqrt{Dh} u_i. \tag{4.1.3}$$

Thus, all we have to do in our numerical simulation routine in eq. (2.5.3) is generating a new sample from a unit normal distribution for each iteration.

What is left is to determine the constant D, which sets the magnitude of the noise variance. In our SQUID simulations, we would like to implement the thermal Johnson current noise I_{N} that is created by the junction shunt resistors. Its magnitude can be expressed by the spectral noise density

$$S_{I_{\mathrm{N}}I_{\mathrm{N}}}(f) = \frac{4k_{\mathrm{B}}T}{R}. \tag{4.1.4}$$

Here f denotes the frequency, k_{B} the Boltzmann constant, T the temperature and R the shunt resistance. As described in section 2.2.2, our model for the numerical simulations works with normalised variables. For the spectral noise density this normalisation results in

$$S_{i_{\mathrm{N}}i_{\mathrm{N}}}(\nu) = \frac{\omega_{\mathrm{c}}}{I_0^2} S_{I_{\mathrm{N}}I_{\mathrm{N}}} = 4\Gamma, \tag{4.1.5}$$

where $\nu = f\frac{2\pi}{\omega_{\mathrm{c}}}$ is the normalised frequency, ω_{c} the characteristic frequency, I_0 the mean critical current of the junctions and Γ the noise parameter. If we compare this to the result from eq. (2.5.12), we find

$$D = 2\Gamma. \tag{4.1.6}$$

We validate the correct behaviour of our white noise model by analysing time recordings of the normalised noise current i_{N} in our simulations. To this end, we generate

100 samples with a total simulation time of $T = 5000$ and a sampling step size of $h = 0.02$ for a noise parameter of $\Gamma = 1 \times 10^{-3}$. T and h are normalised quantities in units of $\omega_{\mathrm{c}}^{-1} = 3.3 \times 10^{-12}\,\mathrm{s}$. We perform a characterisation of the noise properties by calculating the auto-correlation function $C_{i_{\mathrm{N}}i_{\mathrm{N}}}$ and the spectral noise density $S_{i_{\mathrm{N}}i_{\mathrm{N}}}$. The results are presented in fig. 4.1.

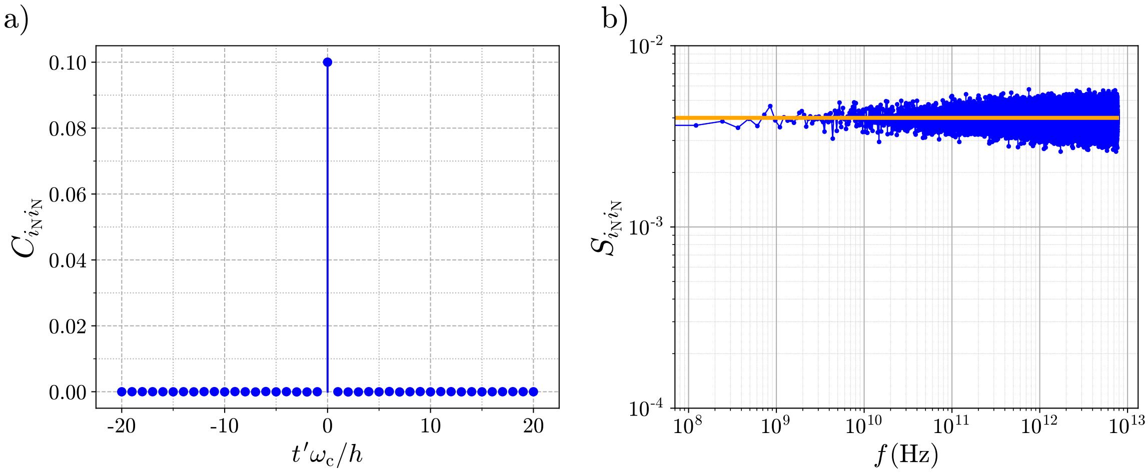

Figure 4.1: Characterisation of the implemented Gaussian white noise model for i_{N}. In a) we plot a section of the auto-correlation function $C_{i_{\mathrm{N}}i_{\mathrm{N}}}$ with respect to time t'. The latter is normalised to ω_{c}^{-1} and expressed in units of the simulation step size h. Plot b) shows the corresponding spectral noise density $S_{i_{\mathrm{N}}i_{\mathrm{N}}}$ vs. the true frequency f. The orange line marks the $S_{i_{\mathrm{N}}i_{\mathrm{N}}} = 4\Gamma$ level. The curves are obtained by averaging over $n = 100$ samples.

If we focus on fig. 4.1 b) first, we can see that the result for $S_{i_{\mathrm{N}}i_{\mathrm{N}}}$ agrees very well with the expected white noise level from eq. (4.1.5). The increasing spread of the data points results from their even frequency spacing. The logarithmic plot collects more points at higher frequencies and therefore shows a larger portion of the underlying Gaussian distribution.

In fig. 4.1 a), we also find good agreement with the predicted Dirac delta function for $C_{i_{\mathrm{N}}i_{\mathrm{N}}}$ in eq. (2.5.11). We can furthermore determine the nominal peak height of $C_{i_{\mathrm{N}}i_{\mathrm{N}}}(0)$. The generated noise current traces are sampled with a step size of $h = 0.02$. According to the Nyquist-Shannon sampling theorem, the maximum frequency component in our noise spectrum will be $\nu_{\mathrm{max}} = 1/2h$. If we consider eq. (2.5.13) and integrate the constant spectral noise density $S_{i_{\mathrm{N}}i_{\mathrm{N}}} = 4\Gamma$ over the frequency range $\nu = [0, \nu_{\max}]$, we obtain

$$C_{i_{\mathrm{N}}i_{\mathrm{N}}}(0) = \sigma^2_{i_{\mathrm{N}}} = \frac{4\Gamma}{2h} = 0.1, \tag{4.1.7}$$

which is also the peak height we find in fig. 4.1 a).

4.1.2 Ornstein-Uhlenbeck noise

Analogue to section 4.1.1, we start with searching for an expression for the noise integral in eq. (2.5.4) of the Ornstein-Uhlenbeck (OU) process, that is suitable to be implemented in our numerical simulations. For this purpose, we define the function

$$W(t) = \int_{t_0}^{t} \xi_{\mathrm{ou}}(s)\mathrm{d}s, \tag{4.1.8}$$

where we integrate the noise term starting from t_0 with $\xi_{\mathrm{ou}}(t_0) = \xi_0$. Hence, the noise integral $w_{\mathrm{ou}}(t_i)$ can be expressed as

$$w_{\mathrm{ou}}(t_i) = W(t_{i+1}) - W(t_i). \tag{4.1.9}$$

Due to the fact that $\frac{\mathrm{d}W}{\mathrm{d}t} = \xi_{\mathrm{ou}}(t)$, we can make use of eq. (2.5.14) and find a solution for $W(t)$ with the initial conditions $W(t_0) = 0$ and $\frac{\mathrm{d}W}{\mathrm{d}t}\big|_{t=t_0} = \xi_0$,

$$W(t) = \tau_{\mathrm{ou}}\xi_0\left(1 - e^{-(t-t_0)/\tau_{\mathrm{ou}}}\right) + c^{1/2}\tau_{\mathrm{ou}}\left[\int_{t_0}^{t}\xi_{\mathrm{w}}(s)\mathrm{d}s - e^{-(t-t_0)/\tau_{\mathrm{ou}}}\int_{t_0}^{t} e^{s/\tau_{\mathrm{ou}}}\xi_{\mathrm{w}}(s)\mathrm{d}s\right]. \tag{4.1.10}$$

As in section 2.5.3, τ_{ou} denotes the relaxation time and c the diffusion constant. Note that our expression for $W(t)$ now only includes integrals of the white noise process ξ_{w} instead of the OU process ξ_{ou}.

This result allows us to determine an update formula for the noise integral w_{ou}. Making use of the definitions

$$\begin{aligned} p &= e^{-h/\tau_{\mathrm{ou}}}, \\ f_1(t) &= c^{1/2}\tau_{\mathrm{ou}}\int_{t}^{t+h}\xi_{\mathrm{w}}(s)\mathrm{d}s, \\ f_2(t) &= -c^{1/2}\tau_{\mathrm{ou}}\, p\, e^{-(t-t_0)/\tau_{\mathrm{ou}}}\int_{t}^{t+h} e^{s/\tau_{\mathrm{ou}}}\xi_{\mathrm{w}}(s)\mathrm{d}s, \end{aligned} \tag{4.1.11}$$

and by discretising the time as $t_i = i \cdot h$, we find the relation

$$w_{\mathrm{ou}}(t_{i+1}) = p w_{\mathrm{ou}}(t_i) - p f_1(t_i) + f_1(t_{i+1}) - f_2(t_i) + f_2(t_{i+1}). \tag{4.1.12}$$

These expressions might still look very complicated, but if we take a closer look at the properties of f_1 and f_2 in eq. (4.1.11), we can greatly simplify the calculation. First of all, f_1 and f_2 describe Gaussian processes, which implies, that we can fully characterise them by their expectation value and auto-correlation. We find for both terms, that $\langle f_1(t_i)\rangle = \langle f_2(t_i)\rangle = 0$. Furthermore, one can calculate the following auto- and cross-correlations:

$$\begin{aligned}\langle f_1(t_i)f_1(t_j)\rangle &= c\tau_{\text{ou}}^2 h\ \delta_{ij},\\ \langle f_2(t_i)f_2(t_j)\rangle &= \frac{c\tau_{\text{ou}}^3}{2}(1-p^2)\ \delta_{ij},\\ \langle f_1(t_i)f_2(t_j)\rangle &= -c\tau_{\text{ou}}^3(1-p)\ \delta_{ij}.\end{aligned} \tag{4.1.13}$$

In contrast to section 4.1.1, we now have two correlated Gaussian processes. This behaviour can be modelled with two unit normal random variables u_i and v_i, with $\langle u_i\rangle = \langle v_i\rangle = 0$, $\langle u_i u_j\rangle = \langle v_i v_j\rangle = \delta_{ij}$ and $\langle u_i v_j\rangle = 0$. To create the correlation between f_1 and f_2, we can simply set

$$\begin{aligned}f_1(t_i) &= \alpha u_i,\\ f_2(t_i) &= \beta u_i + \gamma v_i.\end{aligned} \tag{4.1.14}$$

The weights can then be calculated with the help of eq. (4.1.13). One finds

$$\begin{aligned}\alpha &= \tau_{\text{ou}}\sqrt{ch},\\ \beta &= \tau_{\text{ou}}^2(p-1)\sqrt{\frac{c}{h}},\\ \gamma &= \sqrt{\frac{c\tau_{\text{ou}}^3}{2}\left[1-p^2-\frac{2\tau_{\text{ou}}}{h}(1-p)^2\right]}.\end{aligned} \tag{4.1.15}$$

In summary, to implement an OU noise source we have to update the noise integral term w_{ou} with each iteration according to eq. (4.1.12). This involves two correlated variables f_1 and f_2, which we can model as weighted sums of two unit normal random variables u_i and v_i. To calculate $w_{\text{ou}}(t_{i+1})$ we also require the knowledge of $w_{\text{ou}}(t_i)$, $f_1(t_i)$ and $f_2(t_i)$ of the former iteration. The simulation is therefore not self-starting and we have to initialise w_{ou} with

$$w_{\text{ou}}(t_0) = \sqrt{\frac{c\tau_{\text{ou}}^3}{2}}(1-p)u_{\text{s}} + f_1(t_0) + f_2(t_0), \tag{4.1.16}$$

with u_s being another unit normal random variable independent of u_0 and v_0.

We also generated OU noise traces and carried out an analysis equivalent to the one in section 4.1.1. A total number of 100 samples was simulated for the following parameters (quantities without physical units are normalised to ω_c or ω_c^{-1}):

$$\begin{array}{lll} T = 5000 & h = 0.02 & \Gamma = 1 \times 10^{-3} \\ I_0 = 10\,\mathrm{\mu A} & R_0 = 10\,\Omega & \omega_\mathrm{c} = 3.04 \times 10^{11}\,\mathrm{s}^{-1} \\ f_\mathrm{max} = 100\,\mathrm{GHz} & \tau'_\mathrm{ou} = 0.484 & c' = 8.55 \times 10^{-3} \end{array}$$

We set the relaxation time τ_ou and the diffusion constant c, which fully characterise the OU noise process, according to

$$\tau_\mathrm{ou} = \frac{\tau'_\mathrm{ou}}{\omega_\mathrm{c}} = \frac{1}{2\pi f_\mathrm{max}} \qquad \text{and} \qquad c = \omega_\mathrm{c} c' = \frac{2\Gamma}{\omega_\mathrm{c}\tau_\mathrm{ou}^2}. \tag{4.1.17}$$

These relations are especially convenient for our noise current modelling. They translate the fundamental noise properties to practical measurable quantities. Their meaning is best described with the help of fig. 4.2, where the results of the OU noise analysis are presented.

As indicated in fig. 4.2 b), τ_ou is related to the corner frequency of the spectral noise density $S_{i_\mathrm{N}i_\mathrm{N}}$. This effectively determines the maximum frequency that contributes to the noise, higher frequencies are increasingly suppressed. Furthermore, we find that c is related to the asymptotic value of $S_{i_\mathrm{N}i_\mathrm{N}}$ for low frequencies. As we are interested in modelling Johnson current noise, we have to inherit the corresponding low frequency behaviour. This is described as Gaussian white noise with magnitude 4Γ, see eq. (4.1.5). Thus, by picking a maximum frequency f_max for the OU current noise we fix the relaxation time τ_ou and with our choice for the noise parameter Γ we also set the diffusion constant c. We see that the generated noise is in excellent agreement with the associated theoretical model from eq. (2.5.23).

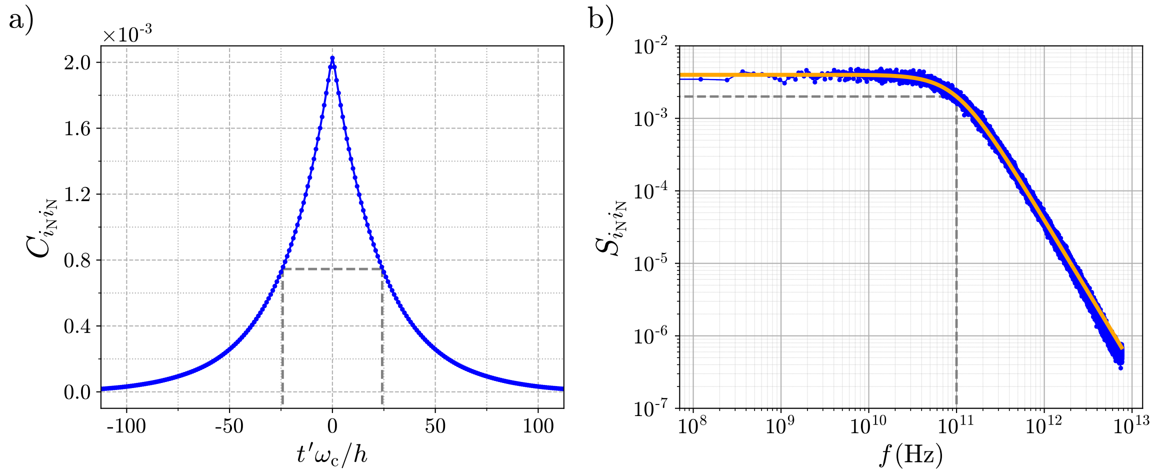

Figure 4.2: Characterisation of the Ornstein-Uhlenbeck noise implementation for i_N. Figure a) shows the auto-correlation function $C_{i_\mathrm{N}i_\mathrm{N}}$ with respect to time t', which is normalised to ω_c^{-1} and expressed in units of the simulation step size h. The vertical grey dashed lines mark points with $t'\omega_\mathrm{c} = \tau'_\mathrm{ou}$, where $C_{i_\mathrm{N}i_\mathrm{N}}$ has dropped to $1/e \cdot C_{i_\mathrm{N}i_\mathrm{N}}(0)$, marked by the horizontal line. In b), the corresponding spectral noise density $S_{i_\mathrm{N}i_\mathrm{N}}$ is plotted vs. frequency f. The theoretical expression from eq. (2.5.23) is shown by the orange line. A grey dashed line marks the corner frequency f_max, where the amplitude of $S_{i_\mathrm{N}i_\mathrm{N}}$ is reduced by a factor 1/2 of the low frequency asymptotic value. The curves are obtained by averaging over $n = 100$ samples.

In fig. 4.2 a), we see how the noise signal is strongly correlated for small values of t' and that the auto-correlation function follows an exponential decay when t' is increased. The decay constant is given by $1/\tau_\mathrm{ou}$. We can further calculate the magnitude of the noise variance $\sigma^2_{i_\mathrm{N}}$, which is equivalent to the auto-correlation function at $t' = 0$, according to eq. (2.5.22). We obtain

$$\sigma^2_{i_\mathrm{N}} = C_{i_\mathrm{N}i_\mathrm{N}}(0) = \frac{c\tau_\mathrm{ou}}{2} = 2.07 \times 10^{-3}, \qquad (4.1.18)$$

which is in good agreement with the peak height in fig. 4.2 a).

4.2 SQUID simulations

In this section, I want to illustrate the influence of various parameters on the SQUID I-Φ-V characteristic curve. First we are going to compare different configurations for the Stewart-McCumber parameter β_C and the screening parameter β_L to get an intuition for their respective effect. This is followed by a study on the individual impact of SQUID asymmetries, defined in section 2.2.2. With that we should be able to decide whether our fitting routine in section 5.1.4 provides meaningful results.

4.2.1 Characteristic curve β_C & β_L dependence

The Stewart-McCumber parameter β_C and the screening parameter β_L describe the junction shunt capacitance and the loop inductance of a SQUID, respectively. Their influence on the SQUID characteristic curve is substantial. But especially its dependence on β_C is intricate and usually investigated by numerical simulations. Hence, I will try to give an overview by illustrating exemplary SQUID characteristic curves for varying β_C and β_L in the following.

The Johnson current noise created by the junction shunt resistors is modelled by a white noise process with $\Gamma = 0.01$. A total simulation time of $T_\mathrm{tot} = 1 \times 10^4$ is used for averaging the resulting SQUID voltage at each point (I_bias, Φ) and the simulation step size is $h = 0.2$. Figure 4.3 presents the obtained SQUID I-Φ-V for $\beta_\mathrm{C} \in \{0.2, 1.0, 2.0\}$ and $\beta_\mathrm{L} \in \{0.5, 1.0, 4.0\}$.

With an increasing screening parameter β_L, the inductance L of the SQUID loop becomes more and more important. For large L, already a small ring current J in the loop is able to generate a substantial amount of flux

$$\frac{\Phi_\mathrm{J}}{\Phi_0} = \frac{LJ}{\Phi_0} = \frac{\beta_\mathrm{L} J}{2I_0} \tag{4.2.1}$$

that will screen the externally applied flux Φ_a. From this follows, that the total flux through the SQUID $\Phi_\mathrm{T} = \Phi_\mathrm{a} + \Phi_\mathrm{J}$ only reaches a maximum value $\Phi_\mathrm{max} < \Phi_0/2$ [23]. We can quantify this behaviour by examining the effective critical current $I_\mathrm{c,eff}$. This is the maximum bias current for a selected external flux Φ_a at which the SQUID is still in the superconducting state with $V = 0$. For $\Phi_\mathrm{T} = \Phi_0/2$, which implies $\beta_\mathrm{L} = 0$, the effective critical current would be $I_\mathrm{c,eff} = 0$ and the modulation depth

$$\frac{\Delta I_\mathrm{c,eff}}{I_\mathrm{c,max}} = \frac{I_\mathrm{c,max} - I_\mathrm{c,min}}{I_\mathrm{c,max}} = \frac{I_\mathrm{c,eff}(\Phi_\mathrm{T} = 0) - I_\mathrm{c,eff}(\Phi_\mathrm{T} = \Phi_\mathrm{max})}{I_\mathrm{c,eff}(\Phi_\mathrm{T} = 0)} \tag{4.2.2}$$

would be maximal with $\Delta I_\mathrm{c,eff}/I_\mathrm{c,max} = 1$. With a screening parameter $\beta_\mathrm{L} \gtrsim 10$ and perfectly symmetric SQUID junctions, the modulation depth scales as [24, 25]

$$\frac{\Delta I_{\mathrm{c,eff}}}{I_{\mathrm{c,max}}} \approx \frac{1}{\beta_{\mathrm{L}}}. \tag{4.2.3}$$

In fig. 4.3, it is easy to see that the modulation depth is continuously reduced with increasing β_{L}, irrespective of the choice for β_{C}.

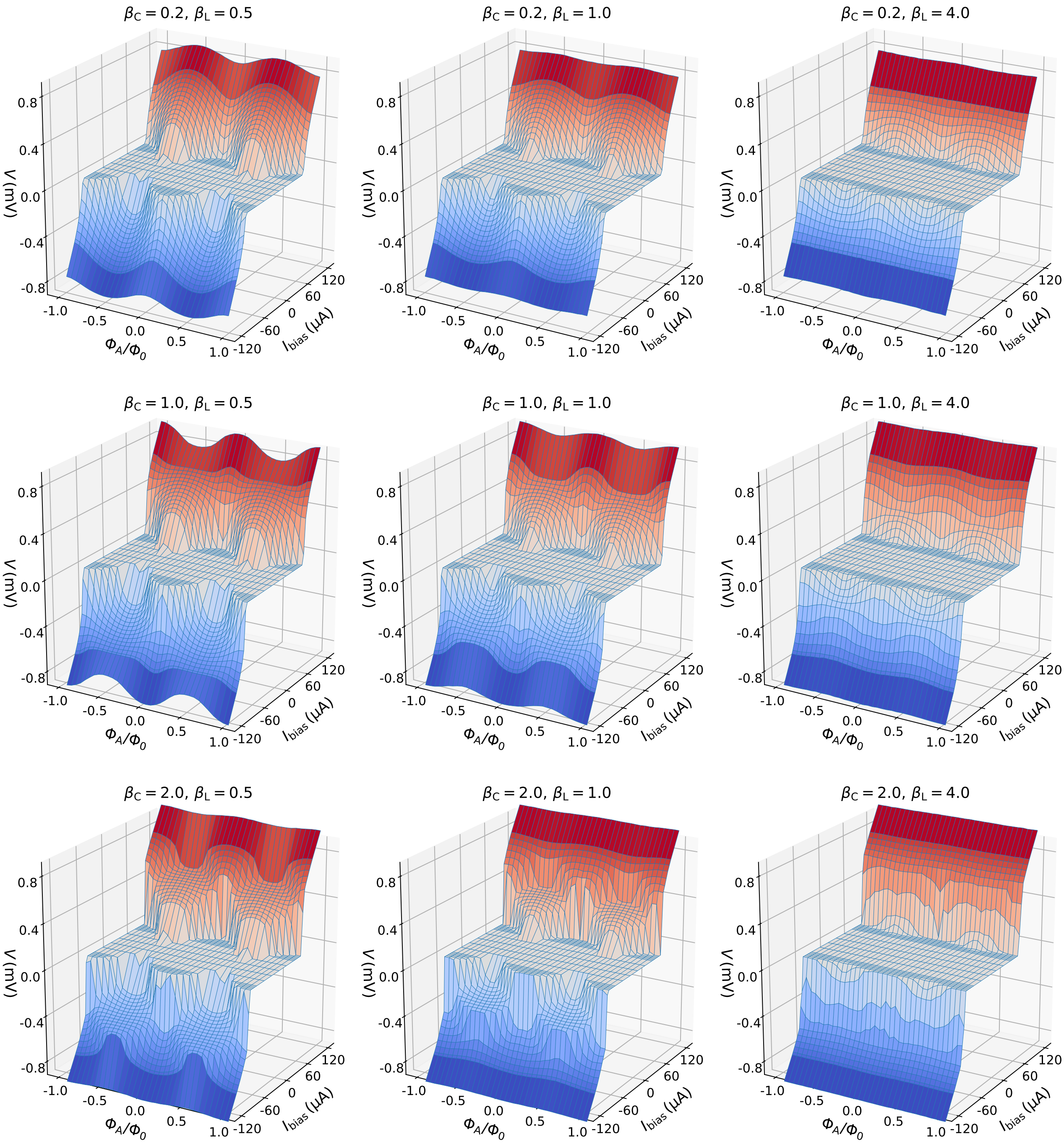

Figure 4.3: SQUID I-Φ-V characteristic curves for varying β_{C} and β_{L}. The plot labels indicate the respective configuration.

The systematics in the SQUID behaviour for different values of β_{C} are less obvious. By increasing β_{C} from small values to $\beta_{\mathrm{C}} \simeq 1$, we can observe a change in the phase of the Φ-V curves for bias currents slightly above the critical point. This is a result of the ring current in the SQUID loop, that excites the resonance of the loop inductance L and the junction capacitance C [26].
Furthermore, without the effect of thermal noise, a SQUID would have a hysteretic I-V curve for values of $\beta_{\mathrm{C}} \gtrsim 0.8$ [27]. My simulation model does not take this effect into account. However, the thermal noise smears out hysteresis effects [26], which means that also the characteristic curves for $\beta_{\mathrm{C}} = 2$ are meaningful. In those, we observe the formation of additional plateaus besides the superconducting region. Also the transition from the superconducting to the normal conducting state becomes more and more pronounced for increasing β_{C}.

4.2.2 Asymmetry studies

Our numerical simulations allow us to generate SQUID I-Φ-V characteristic curves for all relevant parameter combinations. This is especially interesting for analysing the influence of the individual asymmetry parameters defined in section 2.2.2. We simulate SQUID characteristic curves for the parameters $I_0 = 40\,\mu\mathrm{A}$, $R_0 = 17\,\Omega$, $\beta_{\mathrm{C}} = 1.0$, $\beta_{\mathrm{L}} = 4.0$ and $\Gamma = 0.01$ and vary one asymmetry parameter at a time.

Critical current asymmetry α_{I}

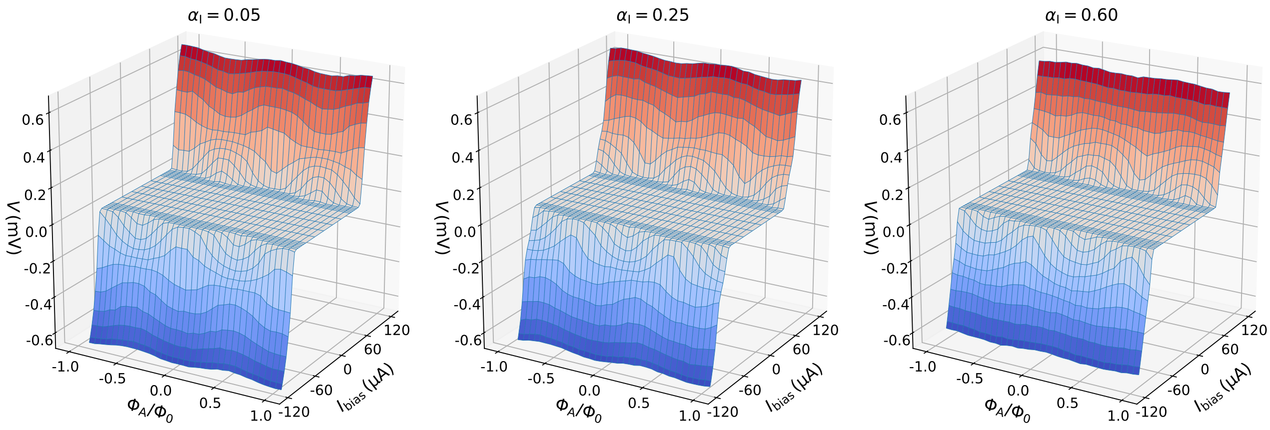

Figure 4.4: Effect of an asymmetry α_{I} in the critical currents of the SQUID junctions.

For increasing values of α_I, we observe a relative shift of the Φ-V curves for positive and negative bias currents. The plot for $\alpha_\mathrm{I} = 0.6$ is close to the extreme case. Here we can e.g. find a SQUID I-V curve, where the magnitude of the effective critical current $|I_\mathrm{c,eff}|$ is maximal for $I_\mathrm{bias} > 0$ and minimal for $I_\mathrm{bias} < 0$. We can define this shift $\Delta\Phi$ with respect to the points of maximum $|I_\mathrm{c,eff}|$ for positive ($I^\mathrm{pos}_\mathrm{c,max}$) and negative bias currents ($I^\mathrm{neg}_\mathrm{c,max}$) as

$$\Delta\Phi = \Phi_\mathrm{a}(I^\mathrm{pos}_\mathrm{c,max}) - \Phi_\mathrm{a}(I^\mathrm{neg}_\mathrm{c,max}). \tag{4.2.4}$$

Studies based on similar numerical simulations lead to the result [24, 25]

$$\frac{\Delta\Phi}{\Phi_0} = \beta_\mathrm{L}(\alpha_\mathrm{I} + \alpha_\mathrm{L}), \tag{4.2.5}$$

with α_L being the inductance asymmetry of the two SQUID loop halves.

In addition, large values of α_I cause a noticeable skew in the Φ-V curves and lead to a reduction of the modulation depth by increasing $I_\mathrm{c,min}$, cf. section 4.2.1. The right most plot illustrates both of these effects.

Shunt resistance asymmetry α_R

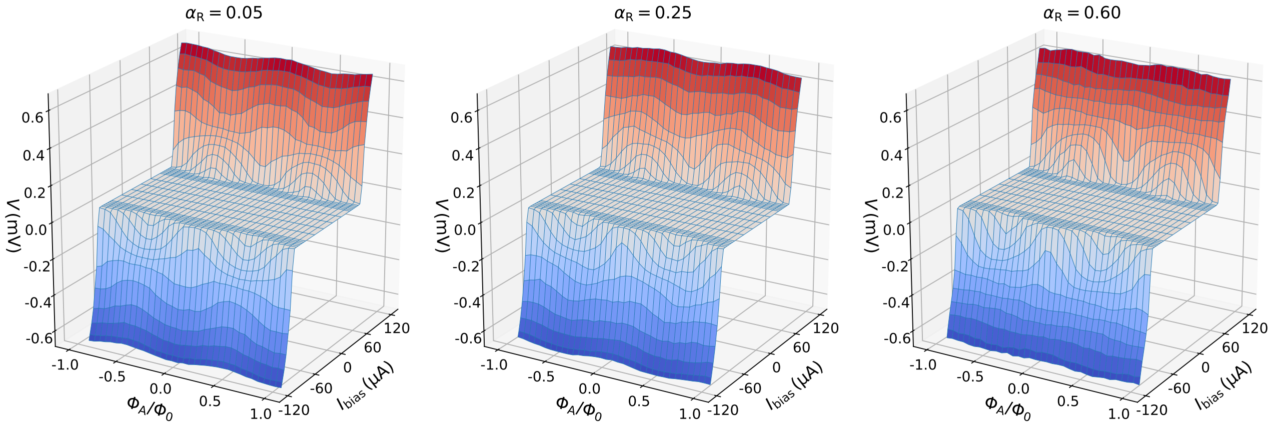

Figure 4.5: Effect of an asymmetry α_R in the shunt resistances of the SQUID junctions.

An asymmetry in the shunt resistors of the two Josephson junctions α_R mostly causes a distortion of the Φ-V curves. For large α_R the modulation depth appears suppressed, especially for bias currents that are clearly above the critical point. We can also observe a slight skewing effect of the characteristic curves. However, there is no relative shift of Φ-V curves for positive and negative bias currents apparent. This is an indicator by which we can discriminate α_R asymmetries from an α_I or α_L imbalance.

Junction capacitance asymmetry α_C

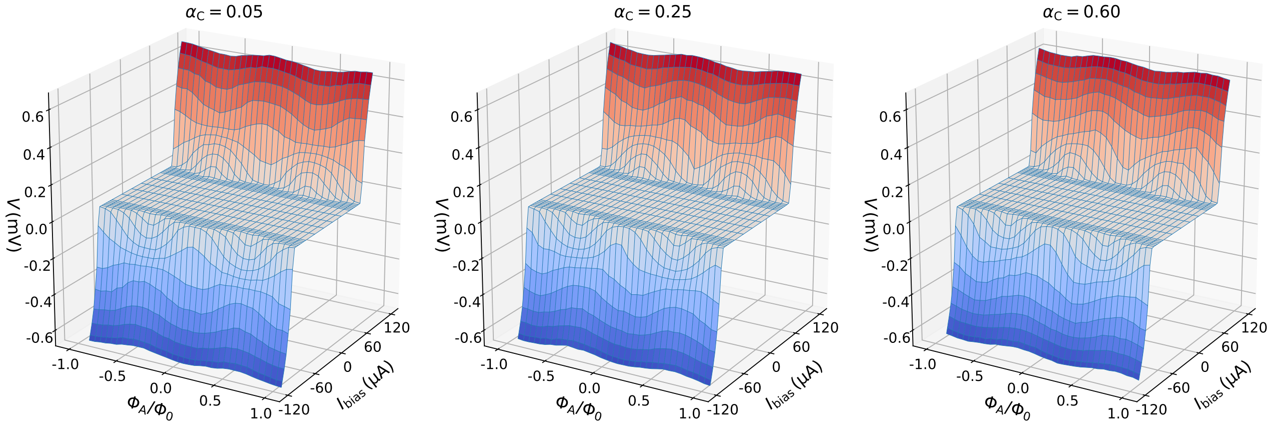

Figure 4.6: Effect of an asymmetry α_C in the junction capacitances of the SQUID.

The characteristics of an imbalance in the junction capacitances α_C are very similar to those of an α_R asymmetry. As before, there is no $\Delta\Phi$ shift apparent. We also find that the Φ-V curves are clearly skewed and that the modulation depth is suppressed for large values of α_C. In our example plots, the former effect is more pronounced and the latter one less than in the prior α_R analysis. It is difficult to discriminate α_C from α_R asymmetries. For a fit procedure as in section 5.1.4 it may be helpful to restrict the capacitance asymmetry to $\alpha_\mathrm{C} = \alpha_\mathrm{I}$. This assumes, that the imbalance is purely of geometric origin and results from a deviation in the size of the two Josephson junctions [28].

Loop inductance asymmetry α_{L}

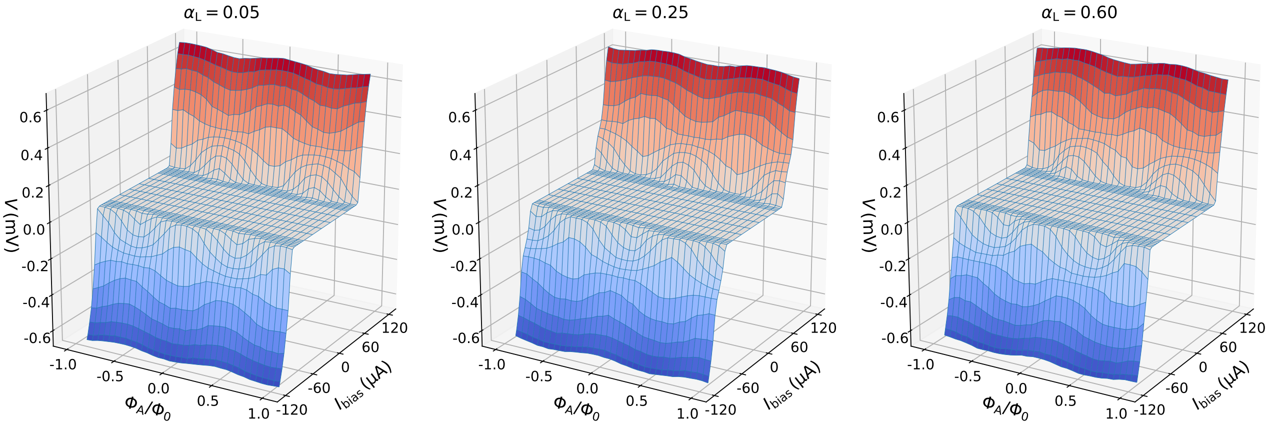

Figure 4.7: Effect of an asymmetry α_{L} in the inductances of the two SQUID loop halves.

As described in eq. (4.2.5), we observe a shift $\Delta\Phi$ between Φ-V curves for positive and negative bias currents if we increase α_{L}. In contrast to the critical current asymmetry α_{I}, we practically cannot observe skewing. Only for the very large value of $\alpha_{\mathrm{L}} = 0.6$ we see the onset of the effect. The inductance asymmetry also does not affect the modulation depth. Hence, we have clear indicators to differentiate between an α_{I} and α_{L} asymmetry.

Chapter 5

Experimental results

This chapter covers the characterisation of components of our experimental setup as well as measurement results. First, we describe the behaviour of our DC SQUID magnetic field sensor. This is followed by performance studies of the elements that create the magnetic field pattern explained in section 2.4 and chapter 3. Finally, we try to detect the thermal motion of the oscillator at a temperature around 1 K in the response of our SQUID.

5.1 DC SQUID characterisation

In the following, we describe the characterisation procedure of the main component of our experiment, the DC SQUID. Its excellent sensitivity to changes in the magnetic field makes it the perfect sensor for detecting the minuscule magnetic distortions induced by the mechanical oscillator. Characterising the performance of our SQUID and extracting characteristic parameters will be the main subject in this chapter. I split this procedure into smaller portions and progressively set bounds on the parameters. At the same time, the behaviour of the SQUID is further illustrated on the basis of actual measurement results.

5.1.1 Current voltage characteristics

The characteristic curve of the voltage V across a SQUID for a chosen bias current I_{bias} describes one important aspect of the functional principle of a SQUID.

The transition point from the superconducting to the resistive state is mainly determined by the critical current I_0 and the shunt resistance R_0 of the Josephson junctions. These quantities refer to the parameters of a single Josephson junction. The parallel arrangement of two junctions in the DC SQUID therefore leads to a superconducting region of the I-V curve that spans $[-2I_0, +2I_0]$ and has a normal conducting asymptote for large bias currents of $V_{\text{normal}} = I_{\text{bias}}R_0/2$. A simplified model of a SQUID I-V curve, neglecting the junction capacitance and thermal noise and assuming perfectly symmetrical junctions is described by

$$v = \begin{cases} 0 & \text{if } |i| \leq 1 \\ \text{sign}(i)\ \sqrt{i^2 - 1} & \text{otherwise.} \end{cases} \tag{5.1.1}$$

Here v is the SQUID voltage normalised to I_0R_0 and i the bias current normalised to $2I_0$.

Figure 5.1 shows a typical curve obtained from SQUID #1 on a Tuebingen sample. In this case, the sample was placed on the still plate of the cryostat with a nominal temperature of roughly 1 K. We performed the measurement by sweeping through a set of bias current values and averaging the SQUID voltage for $t_{\text{avg}} = 0.5\,\text{s}$ for every bias current set point.

From the raw data in fig. 5.1 we can extract an apparent resistance for low bias current values of $R_{\text{wire}} = 1.83(2)\,\Omega$. The limited amount of loom wires in our cryostat prevented a four wire connection. Therefore, the measurements also include the resistance of the connecting wires. Calibrating the line resistance from the cryostat top plate to the 1 K still plate compensates for $R_{\text{loom}} = 1.2(1)\,\Omega$. A temperature check with a ruthenium oxide resistance probe placed inside the sample box yielded a temperature of 1.8(1) K, which is clearly lower than the critical temperature of niobium of roughly 9 K [29]. Due to that, it is fair to assume that the SQUID reached the superconducting state for low bias currents and the slope of the characteristic curve around $I_{\text{bias}} = 0$ should be 0. The remaining discrepancy of approx. $0.6\,\Omega$ is attributed to the rest of the wiring. This includes the section on the cold end, consisting of connectors, PCB and bonding wires, as well as the connection to the measurement devices on the warm end outside the cryostat.

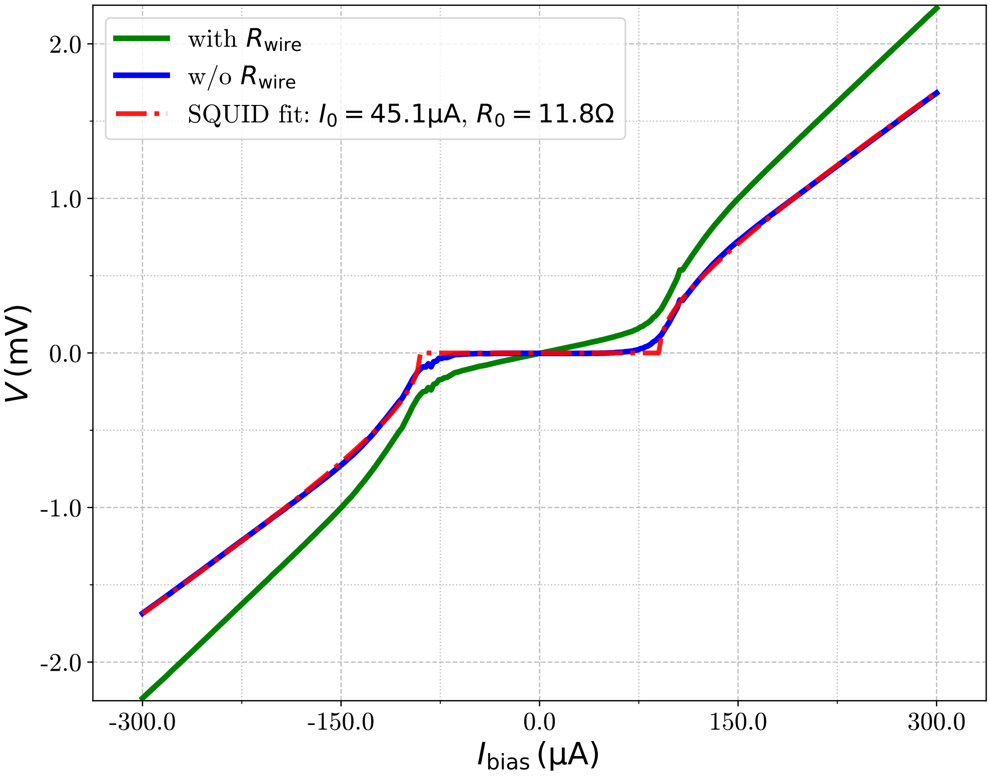

Figure 5.1: SQUID I_{bias}-V curve with wire resistance correction. From the raw data for SQUID #1 represented by the green line, we subtract the resistance of the wiring, resulting in the corrected I-V curve shown in blue. A simplified model for the current-voltage characteristics of a SQUID is fit to the corrected curve. The result is presented by the dash-dotted red line and the obtained fit parameters are listed in the plot legend.

The blue line in fig. 5.1 shows a corrected I-V curve, where the contribution of the wire resistance was subtracted. In addition, the red broken line represents a simple model fit according to eq. (5.1.1). The following parameters are determined from the fit for SQUID #1 on the Tuebingen sample:

$$I_0 = 45.1(1)\,\mu\mathrm{A},$$
$$R_0 = 11.80(2)\,\Omega.$$

The strongly simplified model used in this section only provides a quick estimate for the SQUID parameters. However, the results serve as a good starting point for the more complex fitting procedure in section 5.1.4.

In the course of the experiment, we continuously improved the thermal anchoring of the sample and finally moved the sample box from the initial 4 K stage to the colder 1 K still plate in the cryostat. Hence, we can compare the I-V characteristic curves for different SQUID temperatures, as the experimental setup remained mostly unchanged for these measurements. The only difference results from changes in the cryostat wiring. We can eliminate this influence by comparing the normal conducting asymptote of the I-V curves, determined by the shunt resistance R_0 of the Josephson junctions. As these resistors are fabricated from an AuPd alloy (53 % Au, 47 % Pd) whose resistivity stays constant for the temperature range of interest [30], we can simply adjust the wire resistance such that the normal conducting asymptotes match. Figure 5.2 shows the comparison of the I-V characteristic for SQUID #5 on the Tuebingen sample for three different temperatures.

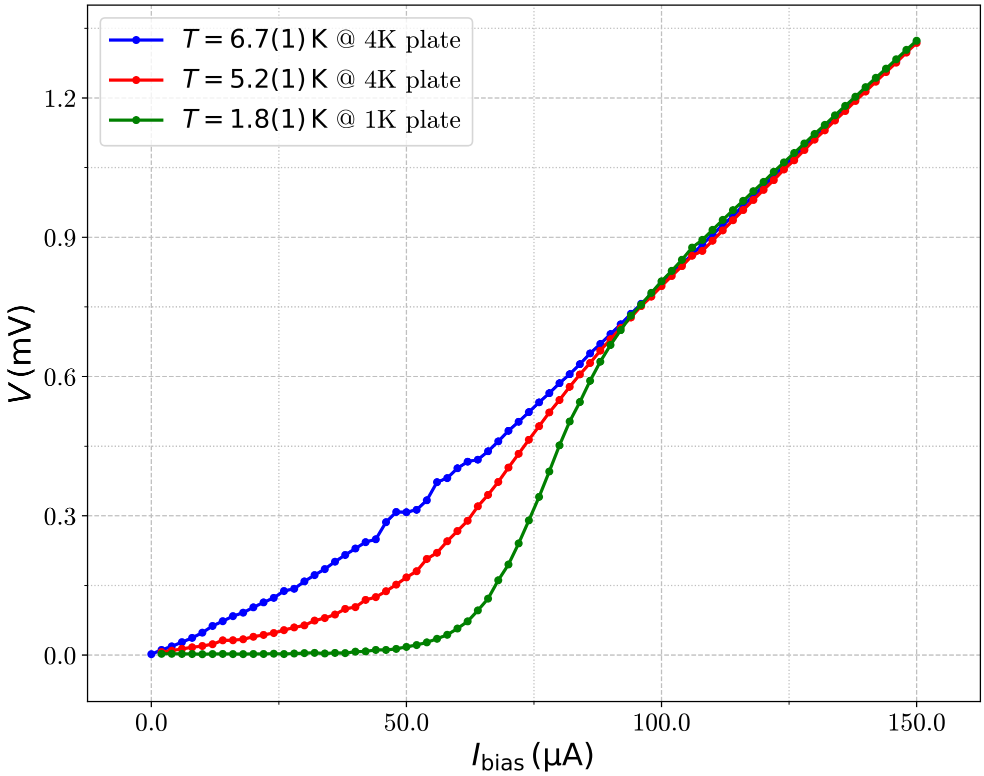

Figure 5.2: Temperature dependence of the SQUID I-V characteristics. The current voltage curves of SQUID #5 for three different cool-down runs are compared. Better thermal anchoring as well as improvements in the wiring lead to a reduced noise rounding of the SQUID I-V curves. Temperatures measured by a ruthenium oxide probe are listed in the legend.

As the temperature decreases, the transition from the normal conducting to the superconducting phase becomes more and more pronounced. The difference between the two measurements at the 4 K plate is related to the improved thermal anchoring. Every joint between the cryostat plate, the pieces of the sample box and the PCB that carries the sample was covered with "GE varnish" to increase the thermal conductivity. Furthermore, we reduced the heat intake from the loom wire by increasing the length of wire between adjacent cryostat plates. Also the thermal anchoring of the loom wire was improved by tightly clamping it at the entrance point to each plate and winding some wire around copper posts covered with "Apiezon® N grease" for better thermal contact. These methods were adopted from the helpful and extensive book on *Experimental Techniques for Low-Temperature Measurements* by J. Ekin [31].

All these improvements led to a temperature reduction from 6.7(1) K to 5.2(1) K between the two runs with the sample positioned on the 4 K plate. It is worth mentioning, that these temperatures were measured at the bottom of the sample box. This box is connected to the SQUID chip via the PCB, whose thermal conductivity is unknown. It is therefore not guaranteed that the SQUID reaches the same final temperature as the sample box. Especially in the first run at 6.7(1) K without the described improvements, the contact might have been too poor to fully thermalize the SQUID chip and the actual sample temperature might be even higher.

We maintained these improvements for the measurements at the 1 K plate and a final temperature of 1.8(1) K was determined. A more detailed characterisation procedure, together with an estimation of the effective temperature of the SQUID is presented in section 5.1.4.

5.1.2 Flux voltage characteristics

The main feature of a SQUID is the modulation of the voltage through applying an external magnetic field. As described in section 3.1.1, the flux bias loop designed to induce this magnetic flux was shorted on all the working SQUIDs of our Tuebingen samples. This could lead to difficulties in coupling flux to the SQUID loop, due to its gradiometric design.

Despite those imperfections, we were able to observe flux tunability for some SQUIDs by using the large bias coil above the sample. In principle this coil is designed to create a constant homogeneous bias field that should be invisible for all gradiometer SQUIDs on the chip. Against our expectations, we could also use it to create a static flux bias for the SQUIDs. This compromise solution has the drawback, that a powerful standard technique for SQUID readout, the so called flux locked loop (FLL), can not be used in the given experimental setup. This method would rely on a quick feedback mechanism that maintains a constant flux through the SQUID loop, which is not possible with the slow response of the bias coil due to its large inductance.

A map of flux voltage curves for SQUID #5 on a Tuebingen sample is shown in fig. 5.3. The data was obtained by acquiring the full I_{bias}-V curve of the SQUID for a set of currents through the bias coil I_{coil}. Due to the fact that the measurement procedure for this large number of points is very time consuming, the averaging time of the SQUID voltage V at each pair of $(I_{\mathrm{bias}}, I_{\mathrm{coil}})$ values was reduced to $t_{\mathrm{avg}} = 0.2\,\mathrm{s}$.

We find that the critical current of SQUID #5 exhibits a very small modulation depth. The voltage V only shows considerable modulation through I_{coil} in a relatively narrow bias current range of $|I_{\mathrm{bias}}| \approx 70..90\,\mu\mathrm{A}$, as illustrated in fig. 5.3(a). On top of that, the shape of the I_{coil}-V curves appears slightly skewed and its maxima and minima do not overlap perfectly for positive and negative bias currents. The latter can be an indication for an asymmetry in the critical currents of the two DC SQUID junctions [26]. This is further investigated in sections 5.1.3 and 5.1.4.

The magnetic field strength of the bias coil grows linearly with increasing bias coil current I_{coil}. Hence, the applied external flux through the SQUID loop Φ_{a} is a linear function of the coil current. We use a "skewed" sine fit to extract the period of the curves and determine the conversion factor $c_{\mathrm{I-\Phi}}$ between I_{coil} and Φ_{a},

$$y(x) = y_0 + \frac{A}{\arctan\left(t/\sqrt{1-t^2}\right)} \arctan\left(\frac{t\sin\left(2\pi\nu x + \phi\right)}{1 + t\cos\left(2\pi\nu x + \phi\right)}\right). \tag{5.1.2}$$

Here, y_0 is the offset, A the amplitude, ν the frequency, ϕ the phase and t the skewness factor with $t \in [-1, +1]$. For $t = 0$, i.e. no skew, this expression produces a sine function of the form $y(x) = y_0 + A\sin(2\pi\nu x + \phi)$. The extreme cases $t = \pm 1$

correspond to positively and negatively skewed sawtooth functions. An example I_{coil}-V curve together with the fitted skewed sine model is shown in fig. 5.3(b). We can determine the conversion factor $c_{\mathrm{I}-\Phi}$ with the period $1/\nu$ according to

$$c_{\mathrm{I}-\Phi} = \frac{1}{\nu\Phi_0} = 6.9(2) \times 10^{-4}\,\mathrm{A}/\Phi_0. \tag{5.1.3}$$

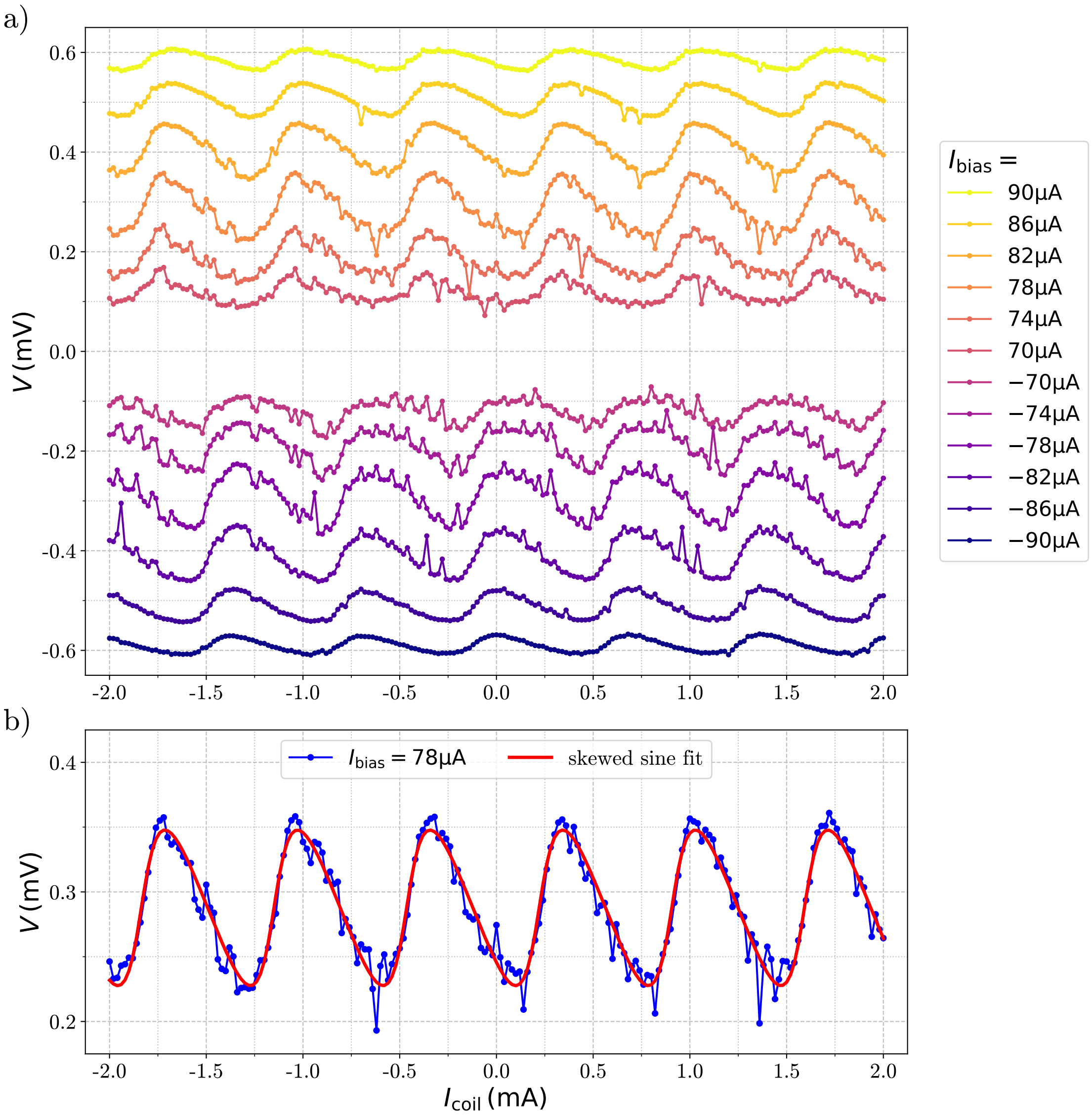

Figure 5.3: SQUID I_{coil}-V flux tuning curves for SQUID #5. Plot a) illustrates the modulation of the SQUID voltage V for varying induced flux in the SQUID loop, controlled via the coil current I_{coil}. The legend lists the I_{bias} set points at which the curves were extracted. In b), the I_{coil}-V characteristic for $I_{\mathrm{bias}} = 78\,\mu\mathrm{A}$ is shown along with a skewed sine model function. Fit parameters are described in the text below. We find the point with maximum flux sensitivity around $I_{\mathrm{coil}} = 0.22\,\mathrm{mA}$.

Another important parameter that we can extract from the I_{coil}-V curves is the flux-to-voltage transfer coefficient V_Φ. It characterises the performance of a SQUID and is determined at the point of maximum flux sensitivity, i.e. the point with the steepest slope in our set of curves. For SQUID #5 we find this point for the configuration $I_{\mathrm{bias}} = 78\,\mu\mathrm{A}$ and $I_{\mathrm{coil}} = 0.22\,\mathrm{mA}$ and obtain a value from our skewed sine fit of

$$V_\Phi = \max_{\Phi_\mathrm{a}} \left| \frac{\partial V}{\partial \Phi_\mathrm{a}} \right| = 6.6(4) \times 10^{-4}\,\mathrm{V}/\Phi_0. \tag{5.1.4}$$

The flux-to-voltage transfer coefficient V_Φ describes the minimum flux change that can be detected and therefore effectively sets the resolution limit of a SQUID.
Let us return to the considerations on the flux tunability. Recall that the flux bias loop is placed directly on top of one half of the gradiometer SQUID and might form a closed superconducting loop because it is shorted. This would act as a perfect shield for magnetic fields and effectively mask the underlying half of the gradiometer loop. Our SQUID design would in this case be reduced to a standard magnetometer layout with a single loop of the size of one gradiometer half. Considering this, we can calculate the necessary magnetic field strength for creating a flux of one Φ_0 at the SQUID loop position. The dimensions of the unmasked gradiometer loop are $A_{\mathrm{eff}} = 13\,\mu\mathrm{m} \times 36\,\mu\mathrm{m}$. Assuming that the magnetic field is homogeneous across the small loop area, its strength has to be

$$B_{\mathrm{z,SQ5}} = \Phi_0 / A_{\mathrm{eff}} = 4.5\,\mu\mathrm{T} \tag{5.1.5}$$

to create an excitation of one Φ_0. We can compare this with the strength of the magnetic field that is created by the bias coil. SQUID #5 is placed $z_{\mathrm{SQ5}} = 2\,\mathrm{mm}$ below the end of the coil and its radial distance from the coils symmetry axis is given by $\rho_{\mathrm{SQ5}} = 4\,\mathrm{mm}$. Plugging those values into eq. (5.2.2) together with the dimensions of the coil body (see section 3.4), the wire diameter $d_{\mathrm{wire}} = 127\,\mu\mathrm{m}$, the number of windings $N = 1680$ and, according to $c_{\mathrm{I}-\Phi}$, a coil current of $I = 0.69(2)\,\mathrm{mA}$, we calculate a field strength at the position of the loop of SQUID #5 of

$$B^{\mathrm{theo}}_{\mathrm{z,SQ5}} = 38.7\,\mu\mathrm{T}. \tag{5.1.6}$$

This is almost a factor 10 larger than the experimental result, thus the simple model that we assumed here does not describe the configuration in the experiment appropriately. In the following, I present two attempts to explain the observations qualitatively.

Hypothesis I: So far, we did not consider the effect of the cantilever chip that is placed directly above the SQUID. In case of SQUID #5, this cantilever is covered with magnetic nanoparticles, which was an attempt to deposit a magnetised material on the cantilever tip (described in detail in section 3.2.2). It can be seen in fig. 3.14 that the deposition also contaminated the region outside the opening for the cantilever. According to ref. [18], these particles show a superparamagnetic response to an applied magnetic field. Therefore, regions with high nanoparticle concentration can channel the magnetic field due to the high magnetic susceptibility and effectively reduce the magnetic field strength in regions without or with low nanoparticle concentration. On our chip, high concentrations are primarily found outside the window for the cantilever. There are also nanoparticles on the cantilever tip, but presumably in a lower concentration. Because the SQUID loop is placed in the centre of the opening for the cantilever, the magnetic field strength could be considerably reduced here. This possibly provides an explanation for the increased magnetic field strength necessary to create a Φ_0 flux excitation in the SQUID loop.

Hypothesis II: The fact that there was a short in the connection to the flux bias loop on all the tested SQUIDs does not imply that the loop forms a closed superconducting ring. If the structure on the chip is however open or only closed via a resistive path, the screening effect would disappear or at least be suppressed. Therefore the gradiometer could work as supposed and the net flux through the twisted SQUID loop would result from an inhomogeneity of the magnetic field. The coil does not create a perfectly homogeneous bias field, it was however checked that this aspect can not account for the large deviation. Hence the field distortion would have to be caused by the nanoparticles or slowly decaying eddy currents in the flux bias loop. Besides that, also an imperfectly balanced and asymmetric gradiometer loop would lead to a net flux even for a homogeneous external bias field. This should however be a minor effect in our case and is not sufficient to explain the observations on its own.

5.1.3 Critical current modulation curve

We can gain better knowledge about the SQUID parameters by viewing the flux voltage curve in a different fashion. Instead of looking at the flux modulation of the SQUID voltage, we can inspect the modulation of the effective critical current $I_{\mathrm{c,eff}}$ when changing the external flux Φ_{a}. If we neglect thermal noise, $I_{\mathrm{c,eff}}$ would be the maximum bias current for a given external flux that we can send through the SQUID without measuring a voltage drop, i.e. the point where the superconductivity of the Josephson junctions breaks down.

To extract a precise value for $I_{\mathrm{c,eff}}$ from an I-V characteristic curve, one would have to know the Stewart-McCumber parameter β_{C}, the screening parameter β_{L} and the noise parameter Γ of the SQUID. In our case these are all unknowns, but if we can determine the modulation depth of $I_{\mathrm{c,eff}}$ we can get a good estimate for β_{L}. We extract $I_{\mathrm{c,eff}}$ from every I-V curve in the data set that was used to construct the flux voltage characteristics in section 5.1.2. By using the simplified model from eq. (5.1.1) as a fit function, we get an estimate for the effective critical current. Our I-V curves show a clear rounding in the region where $I \approx I_{\mathrm{c}}$, due to the effect of thermal noise. The fit function does not account for that and therefore the $I_{\mathrm{c,eff}}$ values that we obtain are slightly biased towards a lower magnitude. However, we are mainly interested in the span of the range in which $I_{\mathrm{c,eff}}$ varies, which should be reproduced correctly by our model. Figure 5.4 shows the resulting modulation curves for positive and negative bias current orientation.

We already observed in section 5.1.2 that the modulation depth for $I_{\mathrm{c,eff}}$ is very small. This clearly indicates, that the screening parameter β_{L} is relatively large, see section 4.2.1. The modulation depth $\Delta I_{\mathrm{c,eff}}/I_{\mathrm{c,max}}$ is determined by fitting the absolute value[1] of the skewed sine function in eq. (5.1.2) to the $I_{\mathrm{c,eff}}$ modulation curves. Obtained results are illustrated by the red and orange line in fig. 5.4 and summarised in table 5.1.

---

[1] We take the absolute value of the oscillating term, offset y_0 and amplitude A are excluded.

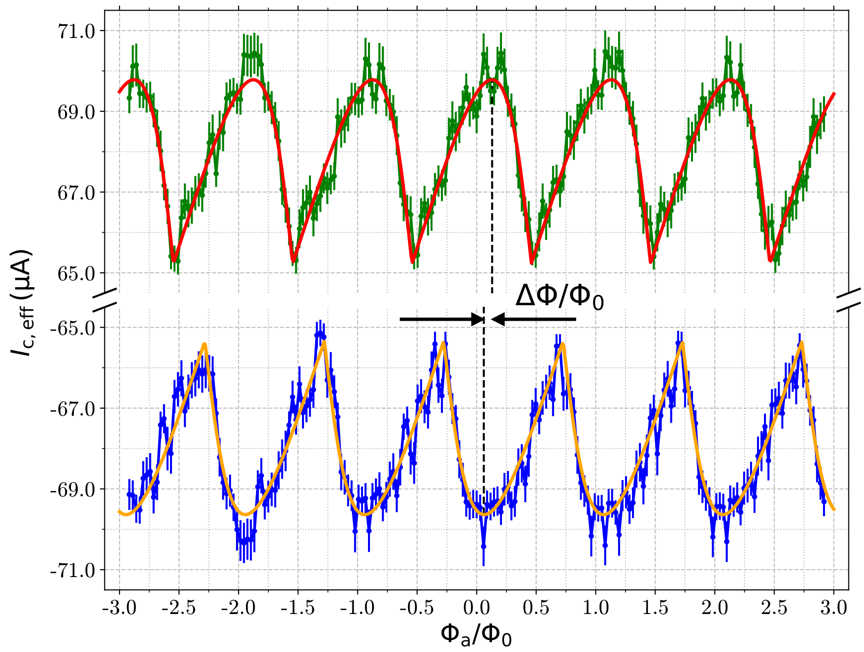

Figure 5.4: $I_{\mathrm{c,eff}}$-Φ modulation curve for positive (green) and negative (blue) bias currents. The data points are obtained from the I_0 fit parameter in the simplified I-V curve model. We fit a modified version of the skewed sine function to these values, shown by the red and orange line. The modulation depth and the relative shift $\Delta\Phi/\Phi_0$ of the $I_{\mathrm{c,eff}}$ curves are determined for positive and negative bias currents individually.

	$I_{\mathrm{c,max}}$ (µA)	$I_{\mathrm{c,min}}$ (µA)	$\Delta I_{\mathrm{c,eff}}/I_{\mathrm{c,max}}$	β_{L}
$I_{\mathrm{bias}} > 0$	69.8(1)	65.23(6)	$6.5(1) \times 10^{-2}$	15.3(3)
$I_{\mathrm{bias}} < 0$	-69.6(1)	-65.35(6)	$6.2(1) \times 10^{-2}$	16.2(3)

Table 5.1: Estimation of the screening parameter β_{L}. Results are calculated from $\beta_{\mathrm{L}} = (\Delta I_{\mathrm{c,eff}}/I_{\mathrm{c,max}})^{-1}$, according to eq. (4.2.3).

Such large values for β_{L} clearly limit the sensitivity of our SQUID. The suppressed critical current modulation directly leads to a lower amplitude in the flux voltage curves and therefore lowers the effective resolution we can achieve in measuring a flux change. For optimal SQUID sensitivity, the recommended parameters are $\beta_{\mathrm{L}} = 1$ and $\beta_{\mathrm{C}} \simeq 1$, see ref. [25]. Considering the fabrication issues we observed on all of our SQUIDs, it is likely that this problem is a consequence of a faulty production run.

Figure 5.4 illustrates other interesting effects that we already observed in section 5.1.2. We can see that the curves are clearly skewed and that there is a small shift between the maxima of the positive and negative $I_{\mathrm{c,eff}}$ curve, labelled with $\Delta\Phi/\Phi_0$. Both of these effects are indications for existent asymmetries in the SQUID, as explained in section 4.2.2. According to eq. (4.2.5), the shift can be caused by either an asymmetry in the critical currents of the junctions α_{I} or an imbalance in the inductances of the SQUID loop halves α_{L}. Both would explain the skewing effect, but the former also causes a reduction of the modulation depth of the $I_{\mathrm{c,eff}}$ curves. Consequently, we cannot decide whether our small modulation depth purely results from a very large screening parameter or is a combination of an α_{I} asymmetry with a lower, but probably still large value of β_{L}. A similar skewing effect can also emerge from an asymmetry in the shunt resistances α_{R} or in the capacitances α_{C} of the Josephson junctions, see section 4.2.2.

We determine a value of $\Delta\Phi/\Phi_0 = 0.07(2)$. The fact that we have an indication for a large value of β_{L} poses a problem, however. Assuming a value of $\beta_{\mathrm{L}} = 15$ we obtain $\alpha_{\mathrm{I}} + \alpha_{\mathrm{L}} = 5 \times 10^{-3}$. It seems unlikely that a close to perfect symmetry was achieved in the fabrication of the samples, considering the imperfections we observed so far. One possibility is, that the asymmetries cancel for the most part. However, it is also possible that we have to consider the distance between next-nearest maxima in the positive and negative $I_{\mathrm{c,eff}}$ curves as the actual shift. For example, a value of $\Delta\Phi/\Phi_0 = 1.07$ would still give a reasonable asymmetry of $\alpha_{\mathrm{I}} + \alpha_{\mathrm{L}} = 7 \times 10^{-2}$ for the same value of β_{L}.

In the following section 5.1.4 we attempt to fit the numerical model from sections 2.2.2 and 4.2 to the full DC SQUID I-Φ-V surface. This should provide further insights in the observed asymmetries and SQUID parameters.

5.1.4 Characteristic parameters

The analysis steps we took so far essentially pictured different cuts through one complex surface, which enabled us to break the characterisation problem into smaller portions and extract information about the DC SQUID parameters bit by bit. In this section we will now investigate the big picture by working with the full I-Φ-V

surface of characteristic curves. This will clarify the connection between the studies we already made and also allow us to gain insights about the characteristic parameters of our DC SQUID. The fit function we are going to use is derived from the RCSJ model in section 2.2.2. It accounts for all the possible asymmetries in the SQUID junctions as well as in the inductance of the two halves of the SQUID loop. Furthermore, the effect of thermal noise of the shunt resistors for the Josephson junctions is implemented by a gaussian white noise or an Ornstein-Uhlenbeck process (see sections 2.5.2 and 2.5.3) and the resulting stochastic differential equations are solved numerically.

The fact that a stochastic process is involved in calculating the SQUID I-Φ-V characteristics makes the fitting procedure more difficult. The calculated points are intrinsically noisy for reasonable simulation times. Hence, using a gradient based optimization algorithm to fit the model function to the data set is not possible, because the gradient will also be noisy. My choice for performing the model fit is a least squares minimisation by a simplex algorithm after Nelder and Mead [32]. This class of optimization algorithms is relatively insensitive to noise, which unfortunately has to be paid with a much larger number of function evaluations to reach an optimal point. The latter are quite costly in our case and therefore the fitting routine is very time consuming.

The starting point for the fit procedure is to create an I-Φ-V sample for a given set of SQUID parameters. A list of these variables together with a description follows in table 5.2. For each $(I_{\text{bias}}, \Phi_{\text{a}})$ configuration, I simulate the time evolution of the two Josephson junction phases δ_1 and δ_2 and the connected voltages $v_1 = \dot{\delta}_1$ and $v_2 = \dot{\delta}_2$. A simulation spans a total duration of $T_{\text{tot}} = 10^4$ with a step size of $h = 0.2$ (in units of $\omega_{\text{c}}^{-1} = \Phi_0/2\pi I_0 R$). The resulting voltage is then determined by forming the time average of eq. (2.2.9), for which I exclude an initial period of $T_{\text{trans}} = 10^3$ to eliminate transient residuals.

The simulated sample I-Φ-V surface now serves as the model function that is passed on to the optimization routine together with our measurement data set. Here the Nelder-Mead minimizer is used, which searches for trial SQUID parameters by using a simplex method. The objective function for the minimizer is a standard sum of squared residuals. Due to the complexity of the parameter space, the optimizer will typically get caught in a local minimum quite easily. As an attempt to find the global minimum, I use a so called ”basin-hopping” algorithm [33]. It essentially tries to find the true minimum by generating random perturbations of the initial guess for the SQUID parameters and uses the result as a new start value for running the minimization procedure.

Figure 5.5 shows a comparison of the fitted model function with the measured characteristics of SQUID #5, which was analysed in the earlier sections. In the top row, the plot illustrates the overall appearance of the I-Φ-V surface and in the bottom row some exemplary characteristic I-V and Φ-V curves are compared.

parameter	description
I_0	Average critical current of the two Josephson junctions (JJs). $I_0 = (I_{0,1} + I_{0,2})/2$
R_0	2 x parallel resistance of the shunt resistors for the two JJs. $R_0 = 2R_1R_2/(R_1 + R_2)$
β_C	Stewart-McCumber parameter. $\beta_\mathrm{C} = 2\pi I_0 R_0^2 C/\Phi_0$ with the average junction capacitance $C = (C_1 + C_2)/2$.
β_L	Screening parameter. $\beta_\mathrm{L} = 2LI_0/\Phi_0$ with the total SQUID loop inductance $L = L_1 + L_2$.
Γ	Noise parameter. $\Gamma = 2\pi k_\mathrm{B}T/I_0\Phi_0$
α_I	Relative asymmetry in the critical currents of the JJs. $\alpha_\mathrm{I} = (I_{0,2} - I_{0,1})/(I_{0,1} + I_{0,2})$
α_R	Relative asymmetry in the shunt resistances of the JJs. $\alpha_\mathrm{R} = (R_1 - R_2)/(R_1 + R_2)$
α_C	Relative asymmetry in the junction capacitances. $\alpha_\mathrm{C} = (C_2 - C_1)/(C_1 + C_2)$
α_L	Relative asymmetry in the inductances of the two halves of the SQUID loop. $\alpha_\mathrm{L} = (L_2 - L_1)/(L_1 + L_2)$

Table 5.2: Characteristic parameters of the DC SQUID. The definitions in this thesis are adopted from the expressions used in ref. [26].

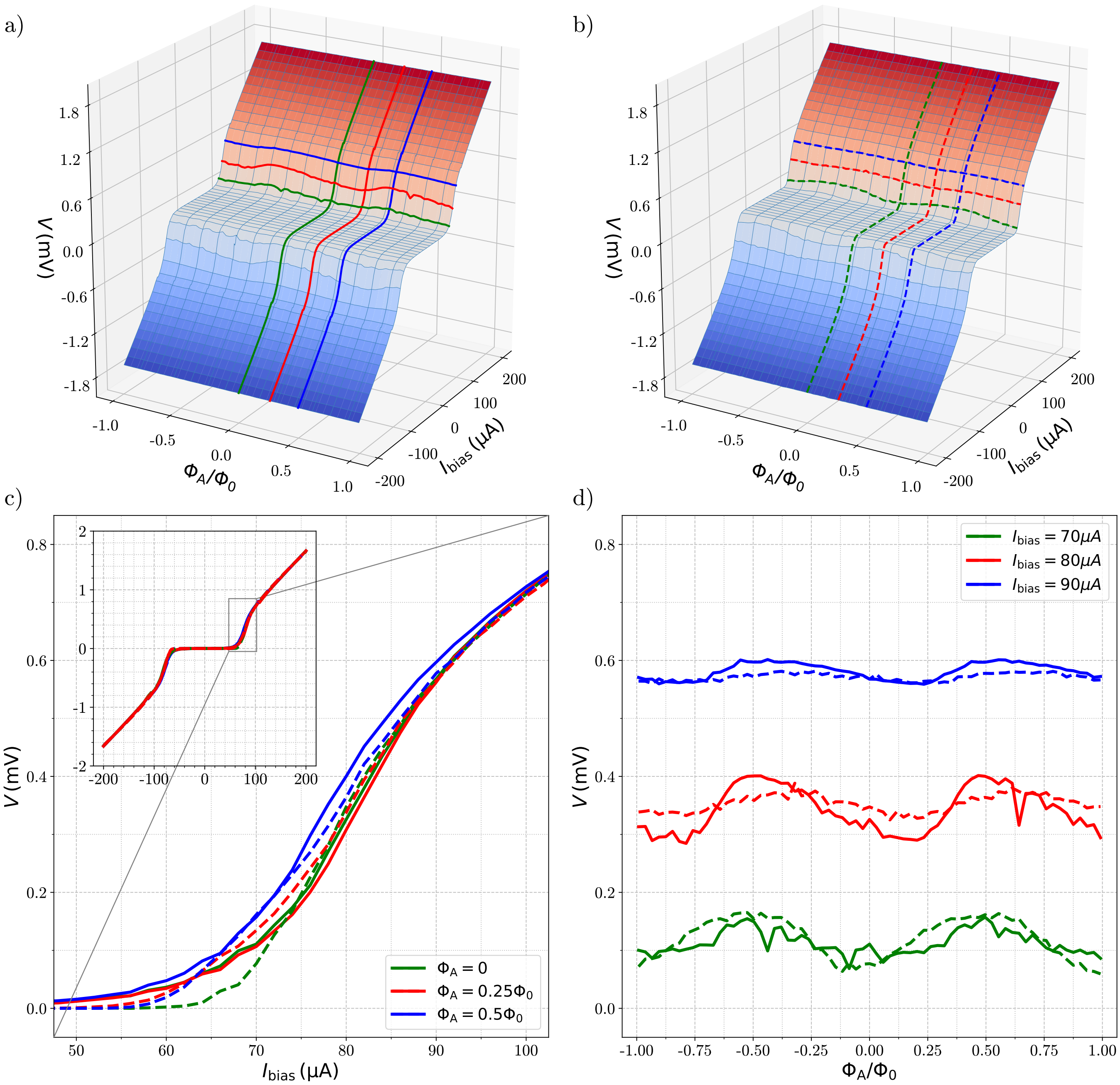

Figure 5.5: SQUID I-Φ-V surface modelling. We compare the experimental data in figure a) with the best fitting result in figure b). Selected lines for fixed flux values Φ_a/Φ_0 and bias currents I_{bias} are compared in figures c) and d), respectively. Measured data is represented by solid and simulation by dashed lines. The inset graph in c) indicates the overall good agreement of experiment and simulation, but deviations in the modulation depth and shifts in the flux curves are clearly visible.

The SQUID parameters for the best fit result obtained from the routine described above is presented in table 5.3.

parameter	value	parameter	value
I_0	$38.0\,\mu\mathrm{A}$	α_I	0.202
R_0	$16.68\,\Omega$	α_R	0.027
β_C	1.043	α_C	0.246
β_L	4.640	α_L	0.167
Γ	3.41×10^{-2}		

Table 5.3: Fit parameters obtained from the optimization procedure for the numerical simulations of the model in section 2.2.2. The target data is represented by the measured SQUID I-Φ-V surface for SQUID #5 on the Tuebingen sample.

Referring to section 5.1.3, we find a few deviations to the earlier estimates for the characteristic parameters. First, the average critical current of the junctions I_0 is larger. This was expected, because the noise rounding of the SQUID I-V biases critical currents of the simplified fit function of eq. (5.1.1) to lower values. Secondly, we obtain a much smaller value for β_L than expected. This can be caused by a combination of effects. On the one hand, we have neglected how asymmetries affect the $I_\mathrm{c,eff}$ modulation. Section 4.2.2 illustrates that α_I, α_R and α_C imbalances can lead to a suppression of the modulation depth. According to the fit result, all of these asymmetries are non negligible. On the other hand, the simple SQUID I-V fit cannot reproduce the modulation behaviour perfectly and likely smooths the obtained $I_\mathrm{c,eff}$ curve, which leads to an overestimation of β_L.

Our model also allows us to get a figure for the Stewart-McCumber parameter β_C and the noise parameter Γ. It is remarkable that the value for β_C is close to the optimal case of $\beta_\mathrm{C} = 1$ [25]. On the other hand, the result for the noise parameter illustrates a serious issue in our experimental setup. We obtain a value of $\Gamma = 3.41 \times 10^{-2}$ which translates to an effective temperature of the SQUID of $T = 30.9\,\mathrm{K}$. This is a lot higher than the 1.8(1) K measured in the sample box (see section 5.1.1) and even higher than the critical temperature of niobium, which can obviously not be correct. The root of this inapplicable result is that our model does not discriminate between actual thermal current noise (Johnson noise) caused by the shunt resistors, flux noise that induces a fluctuating ring current in the SQUID loop and bias current noise. The noise parameter Γ therefore describes the sum of these effects and cannot be used to directly calculate the SQUID temperature. As a consequence, we can draw the conclusion that our SQUID is subject to excessive noise, which is a major issue for its performance. The magnetic shielding of the sample box is presumably very good, therefore flux noise from external sources should not be a problem. However, if RF noise is picked up in the wiring outside the cryostat, it can be routed to the SQUID sample. This can either happen directly as bias current noise or via surrounding wires on the chip in the form of flux noise. Hence, improved RF shielding and filtering will be necessary and highly beneficial in a future version of the experimental arrangement.

Finally, we can take a look at the outcome for the asymmetry parameters of our fit. For the inductance asymmetry α_L of the two arms of the SQUID loop we obtain $L_1/L_2 = 0.714$. The deviation of the geometric inductances of the two gradiometer loops should be negligible, meaning that the asymmetry we obtain is most likely caused by mutual inductance effects (e.g. with the cantilever) that are included in the loop inductances L_1 and L_2.

The Josephson junction properties α_I and α_C result in surprisingly large values, α_R is as expected comparably small. If we express those parameters as the ratios of the underlying physical entities, we get

$$I_{0,1}/I_{0,2} = 0.664 \qquad R_1/R_2 = 1.055 \qquad C_1/C_2 = 0.605.$$

The reason for an asymmetry in the junction parameters is most likely a deviation from its nominal size, that results from imperfections in the fabrication procedure. Therefore, the asymmetry is typically of geometric origin, which would mean that $\alpha_\mathrm{I} = \alpha_\mathrm{R} = \alpha_\mathrm{C}$ [28]. However, for DC SQUIDs as ours, the Josephson junctions are usually externally shunted, meaning that the shunt resistance is not the intrinsic resistance of the junction, but a dedicated separate resistor on the chip. Because of that, α_R is completely independent of the other asymmetry parameters. As discussed in section 3.1.3, the step coverage of the thin gold resistive layer on top of the very thick niobium top layer is decent, resulting in resistances close to the nominal values.

The cause for the relatively large values of α_I and α_C is unclear. It is fair to assume that the asymmetry in the capacitances is mainly of geometric origin. The deviation between α_I and α_C would imply, that the asymmetry of the critical currents of the junctions also has an intrinsic contribution, i.e. a variation in the film properties. We were not able to perform any further investigations on those imperfections. A destructive test to inspect the junction cross section would probably give further insights.

5.2 Bias coil

One essential component for reaching the remarkably high magnetic field gradients proposed in ref. [5] is the large bias coil that should create a homogeneous magnetic field across the arrangement of SQUID and cantilever. As described in section 3.4, we had to manufacture multiple bias coils due to problems with the very thin and fragile insulation of the superconducting wire that caused shorts to the coil body. Despite those issues, we calibrated the created magnetic field with a Hall probe measurement and demonstrated that the thin superconducting wire can withstand the intended coil current of 1 A.

5.2.1 Magnetic field calibration

We performed a Hall probe measurement to calibrate the magnetic field created by the bias coil and to rule out possible shorts between neighbouring turns that would effectively reduce the number of windings of the coil. Because we are especially interested in the gradient of the coil field, we placed three evenly spaced Hall probes in the bottom of our sample box. The sensitive area of those probes is centred on the symmetry axis of the coil, the nominal spacings can be found in fig. 5.6.

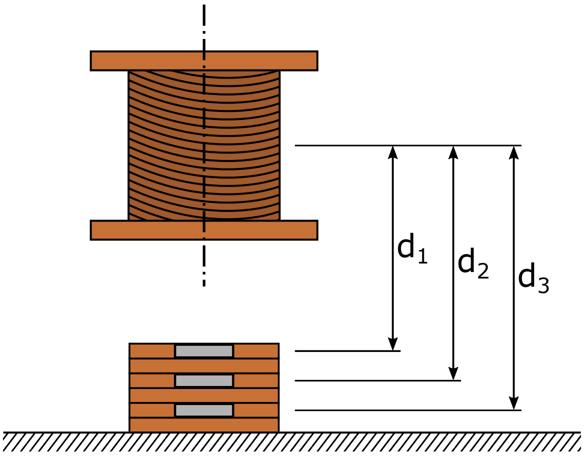

Figure 5.6: Bias coil arrangement. We align the Hall probes to the symmetry axis of the bias coil inside custom made spacers. The nominal spacings of Hall probe 1, 2 and 3 to the centre of the coil body are $d_1 = 7.2\,\mathrm{mm}$, $d_2 = 9.2\,\mathrm{mm}$ and $d_3 = 11.2\,\mathrm{mm}$ respectively.

We can describe the total field created by our coil as a sum of the contribution of each individual turn. The magnetic field of a single wire loop with radius R and current I can be expressed in cylindrical coordinates as

$$\vec{B}_{\mathrm{loop}}(\rho, z, R, I) = \frac{I\mu_0}{2\pi}\frac{1}{\sqrt{(R+\rho)^2+z^2}} \left[\frac{z}{\rho}\left(\frac{R^2+\rho^2+z^2}{(R-\rho)^2+z^2}E(k^2) - K(k^2)\right)\vec{e}_\rho + \right. \\ \left. + \left(\frac{R^2-\rho^2-z^2}{(R-\rho)^2+z^2}E(k^2) + K(k^2)\right)\vec{e}_{\mathrm{z}}\right], \tag{5.2.1}$$

$$k^2 = \frac{4R\rho}{(R+\rho)^2+z^2}.$$

Here ρ and z denote the radial and axial distance from the centre of the loop and $K(k^2)$ and $E(k^2)$ are the complete elliptic integrals of first and second kind. In the sum of the loop contributions, we have to take care of setting the radius p_{R} and axial position p_{z} of each winding correctly, as we build up the coil layer by layer. This can be described by

$$\vec{B}_{\mathrm{coil}}(\rho, z, R_{\mathrm{in}}, h_{\mathrm{coil}}, d_{\mathrm{wire}}, N, I) = \sum_{n=0}^{N} \vec{B}_{\mathrm{loop}}\Big(\rho, p_{\mathrm{z}}(z,n), p_{\mathrm{R}}(R_{\mathrm{in}},n), I\Big), \tag{5.2.2}$$

$$p_{\mathrm{z}}(z,n) = z - \frac{h_{\mathrm{coil}}}{2} + \left(\frac{1}{2} + n \bmod n_{\mathrm{layer}}\right) d_{\mathrm{wire}},$$

$$p_{\mathrm{R}}(R_{\mathrm{in}},n) = R_{\mathrm{in}} + \left(\frac{1}{2} + \left\lfloor \frac{n}{n_{\mathrm{layer}}} \right\rfloor\right) d_{\mathrm{wire}},$$

with $n_{\text{layer}} = \left\lfloor \frac{h_{\text{coil}}}{d_{\text{wire}}} \right\rfloor$ and $\lfloor \cdot \rfloor$ denoting the floor function. In this expression, h_{coil} is the height and R_{in} the radius of the coil body, d_{wire} is the diameter of the wire used to wind the coil and N is the number of windings. The coordinates $\rho = z = 0$ represent the centre of the coil body.

We can check if this simple model reproduces the magnetic field measured by the Hall probes with respect to magnitude and gradient along the axial z direction. The results for the first generation of our bias coil with $d_{\text{wire}} = 67\,\mu\text{m}$ and $N = 5240$ are presented in fig. 5.7.

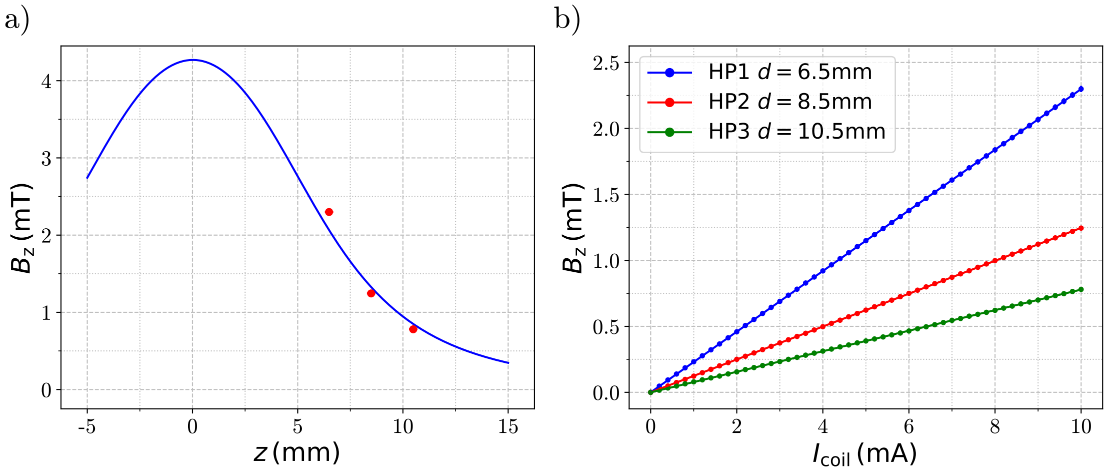

Figure 5.7: Magnetic field calibration of the bias coil. In a) we plot the magnetic field component B_z vs. the axial distance z from the centre of the coil body for a coil current of $I_{\text{coil}} = 10\,\text{mA}$. The blue line shows a fit of the model in eq. (5.2.2) and the red dots represent the measured field strengths of the three Hall probes. Sub plot b) displays the results of the Hall probe measurements for a sweep of the coil current, illustrating the perfectly linear relation. The spacings d listed in the legend include a correction factor with respect to the nominal values in fig. 5.6.

In fig. 5.7 a) we show a comparison of the magnetic field z-component measured by the Hall probes for $I_{\text{coil}} = 10\,\text{mA}$ along with the prediction of $\vec{B}_{\text{coil}}$ from eq. (5.2.2). The latter was modified by an additional factor that takes a possible z-displacement of the coil from its nominal position into account. A fit to the measured Hall probe data determines this value to be $d_{\text{dev}} = -0.710(6)\,\text{mm}$. Hence, the coil is placed a little closer to the Hall probes than intended, a deviation of less than a millimetre is however within the level of positioning accuracy that can be expected.

Figure 5.7 b) shows the magnetic field strength B_z measured by the three Hall probes vs. the applied coil current I_coil. An offset in the Hall probe voltages is compensated by a measurement with reversed coil current. The linear relation of field strength to current in eq. (5.2.2) is clearly satisfied. In the legend, we list the corrected distance d for each Hall probe measured from the centre of the coil body.

5.2.2 Current limitation

If we want to achieve a high magnetic field gradient in our experimental configuration, also the magnitude of the created fields will have to be relatively large. The limit for the highest magnetic field strength we can allow in our setup is the lower critical field of niobium of $B_\mathrm{crit} \approx 140\,\mathrm{mT}$ [14]. For our first generation of the bias coil, where we used a very thin $67\,\mu\mathrm{m}$ NbTi wire and wound a total number of windings $N = 5240$ on the coil body, this magnetic field strength at the position of the cantilever and SQUID chip is reached for a coil current of $I_\mathrm{coil} \approx 750\,\mathrm{mA}$.

In an initial attempt with our first generation bias coil, we achieved a maximum coil current of only roughly $100\,\mathrm{mA}$. The NbTi wire we used would however have a current rating of a few A [34]. Due to the fact, that this wire type only carries a single NbTi filament inside a copper cladding, we suspect that the superconducting wire broke in some places during the coil winding procedure. At the position of a defect, the current then has to be carried by the copper cladding, which would heat up rapidly for such high currents and in turn warm up a larger section of the NbTi wire, which leads to a breakdown of the superconductivity of the coil.

As a consequence, we decided to fabricate a second bias coil with fewer turns, but with a much thicker multi-filament NbTi wire with a diameter of $d_\mathrm{wire} = 254\,\mu\mathrm{m}$. This run resulted in a total number of $N = 440$ turns which were hand-wound in order to avoid damaging the superconducting filaments and the fragile insulation of the wire. The performance of this proof-of-principle attempt in a stress-test is presented in fig. 5.8.

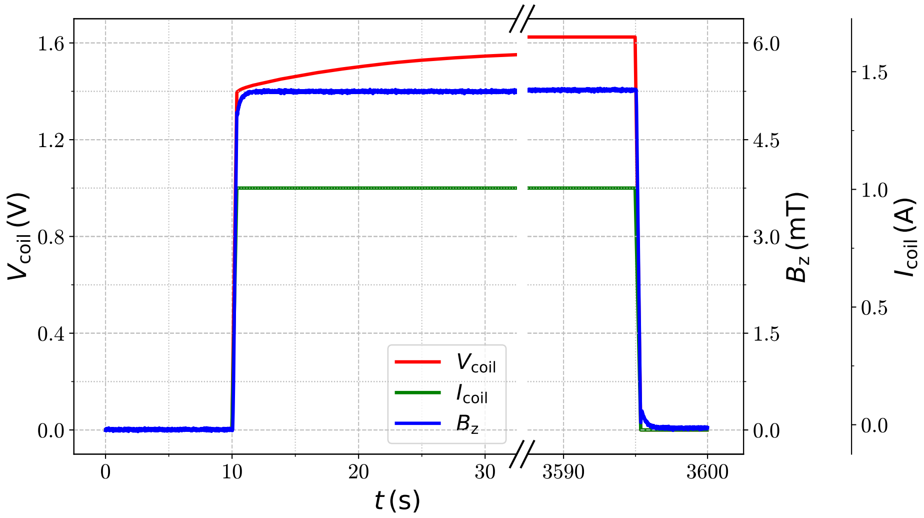

Figure 5.8: Stress test of the second generation bias coil. The plot shows the recordings of the voltage applied to the coil circuit V_{coil}, the magnetic field B_{z} measured by a Hall probe and the coil current I_{coil} vs. time t. The measured quantities refer to the axes on the left, the inner right and the outer right, respectively.

As we can see in the time log, the second generation coil survived a current of $I_{\text{coil}} = 1\,\text{A}$, continuously applied for a period of a full hour. V_{coil} represents the voltage drop across the normal conducting copper high current lines. We observe a slow increase in the resistance of those wires as the large current heats up the copper. This does not pose a problem however, as most of the heat load is deposited on the upper plates of the cryostat, where sufficient cooling power is available. Finally, the measured magnetic field strength $B_{\text{z}} = 5.26(1)\,\text{mT}$ is in perfect agreement with the predicted value from eq. (5.2.2). The nominal distance between the centre of the coil and the position of the Hall probe in this experiment was $d = 12.2\,\text{mm}$, for which we calculate a value of $B_{\text{z,coil}} = 5.32\,\text{mT}$.

The findings from those first two attempts resulted in a third generation for the bias coil with an intermediate wire diameter of $d_{\text{wire}} = 127\,\mu\text{m}$ and a total number of windings of $N = 1680$. The current limitations for this coil have not been tested so far, because the experiment had to move to another cryostat that was not equipped with the high current wiring described in section 3.5.2. A maximum applied current of 80 mA over a comparably long period did not cause any problems, however. To achieve the desired field strength of 140 mT, either a more careful technique for the winding procedure with the very thin 67 µm wire has to be found, or a design change in the experimental setup that allows for a bigger coil is necessary.

5.3 Quadrupole line

Besides the SQUID structures, our sample chip also carries superconducting lines in the shape of a very narrow and long loop. Its main section is formed by two close parallel wires with currents flowing in opposite directions. In combination with the field of the bias coil, we create a quadrupole-like field configuration around the location of the cantilever tip with zero magnetic field strength at the resting position of the beam, cf. section 2.4.

In our experiment, we aim to create a large magnetic field gradient around the zero position, which is favourable in multiple ways. On the one hand, this increases the induced supercurrents (eddy currents in case of a normal conductor) in the strip on the tip of the cantilever. The magnetic field that is created by those currents can be detected by the SQUID. Larger induced currents lead to an increased signal strength, which in turn allows for smaller displacements of the cantilever to be detected. On the other hand, the effective magnetic moment of the cantilever tip is increased. This improves the prospects for feedback- or parametric cooling techniques to reduce the effective cantilever temperature in a later stage of the experiment.

As we have seen in section 5.2, we can apply a current of 1 A to a coil with $N = 440$ windings. In this case, the bias coil creates a magnetic field strength at the cantilever position of $B_\mathrm{z} = 5.3\,\mathrm{mT}$. If we want to move the point with zero magnetic field to this location, we have to send a current of $I_\mathrm{qp} \approx 350\,\mathrm{mA}$ through the quadrupole line. We conducted a test measurement on our Tuebingen SQUID chip and applied currents in a range of $I_\mathrm{qp} = -10\ldots10\,\mathrm{mA}$ while monitoring the behaviour of SQUID #1. The results are summarised in fig. 5.9.

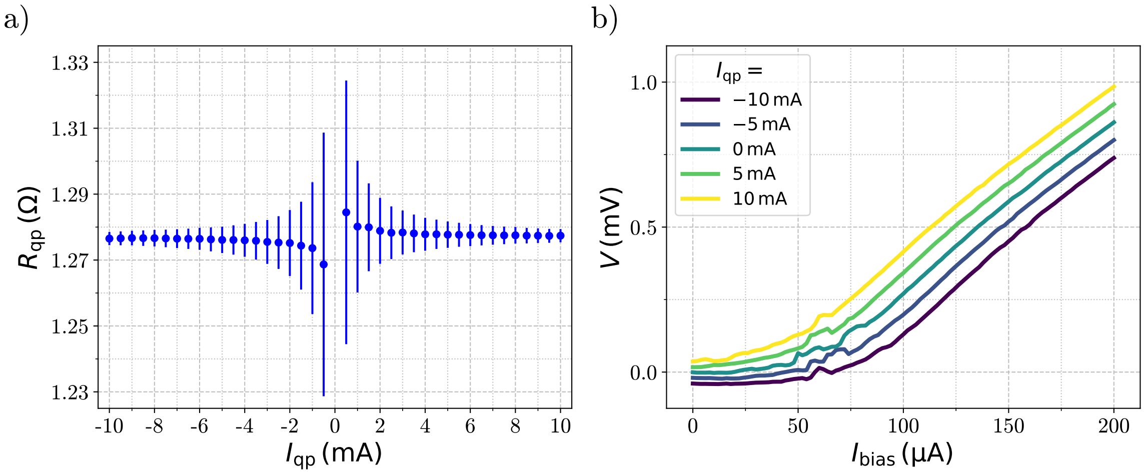

Figure 5.9: Quadrupole line stress test with SQUID monitoring. Fig. a) shows the measured resistance of the quadrupole line for different currents I_{qp}, indicating that the superconducting state is always preserved. In fig. b) we show the behaviour of SQUID #1 during this test. Applying a current to the quadrupole line clearly affects the SQUID, which would put the sensitive Josephson junctions at risk for larger currents I_{qp}.

As one can see in fig. 5.9 a), we find that the resistance of the quadrupole line R_{qp} stays constant through the course of the measurement. The current I_{qp} is applied for 45 s continuously, which is also the duration we use to record a single SQUID I-V curve. On this time scale, we do not observe heating processes as in section 5.2. The increasing uncertainty in the resistance R_{qp} for small values of I_{qp} is a consequence of an absolute uncertainty in the underlying voltage measurement. We determine a mean value of $\bar{R}_{\mathrm{qp}} = 1.277(2)\,\Omega$, which is in good agreement with the wiring resistance from the current source to the sample chip of $R_{\mathrm{wire}} = 1.2(1)\,\Omega$. Therefore, the quadrupole line remains in the superconducting state for the whole measurement series and we have not reached the critical current of the structure.

The reason why we limited the current range to such low values is illustrated in fig. 5.9 b), where the SQUID I-V curve for selected I_{qp} is shown. We observe that the behaviour of the SQUID is clearly affected by a current flow in the quadrupole line, which should, by design, not be the case. An imperfect balance in the gradiometer loops would explain a flux shift in the SQUID characteristics, which apparently applies to the measurements in fig. 5.9 b). However, we also observe a voltage offset of the SQUID I-V curves that depends on the quadrupole line current. This means that the two circuits of quadrupole line and SQUID are not galvanically isolated. We therefore cannot apply large currents to the quadrupole line without taking the risk of damaging the SQUIDs.

Consequently, we were not able to use the quadrupole line in our experiments on the detection of a signal from the cantilever. It is likely that the origin of this faulty connection between SQUID and quadrupole line circuit is related to the issue of the shorted flux bias loops, cf. section 5.1.2. The minimum spacing between neighbouring lines is comparable for those structures and as discussed in section 3.1.1 there were problems in the fabrication that could explain those undesired connections.

5.4 Cantilever detection

After a series of optimizations on the performance and a careful characterisation of our SQUID, we made an attempt to detect a signal from the micromechanical oscillator. The change to the Tuebingen SQUID design required a compromise, though. Our cantilever chips were designed to match the layout of the IBK SQUID chips. The orientation and the positioning of the SQUIDs on the Tuebingen layout differed from that, however. Therefore we could not make use of all 8 cantilevers on a chip, but had to focus on the alignment of a single one. In our final experimental setup, we placed two cantilever chips on top of a SQUID chip. We aligned a chromium-tip cantilever to SQUID #1 and the cantilever covered with nanoparticles (see fig. 3.14 was placed on top of SQUID #5.

Unfortunately, SQUID #1 suffered an inexplicable breakdown before a measurement was possible, so the tests could only be performed on SQUID #5.

5.4.1 SQUID bias current scan

The SQUID is connected to a spectrum analyser to possibly find an indication of the cantilever. We record noise spectra of the SQUID output voltage V and try to identify a signal in a reasonable frequency range for the fundamental mode of the oscillator that stands out from the noise floor.

From eq. (2.3.2) we can calculate a nominal resonance frequency of $f_0 = 553\,\text{kHz}$. We acquired noise spectra for the frequency ranges $250 - 550\,\text{kHz}$ and $50 - 1050\,\text{kHz}$ with a resolution bandwidth of $3\,\text{Hz}$ and $2\,\text{Hz}$ respectively. Each spectrum is an average of 100 traces. Finally, we record such spectra for a range of SQUID bias currents $I_{\text{bias}} = 0 - 150\,\mu\text{A}$. With that, we tune the sensitivity of the SQUID, which enables us to decide whether a noise peak is caused by a flux signal or by electromagnetic interference (EMI) from which the output line is not sufficiently shielded. The former would clearly depend on the SQUID sensitivity and should thus vanish for bias currents where the SQUID is insensitive to flux, whereas the latter would be present for any value of I_{bias}. The coil current is constantly kept at $I_{\text{coil}} = 350\,\mu\text{A}$. This was the value with the maximum flux sensitivity, obtained from an analysis identical to section 5.1.2 right before the measurements were recorded. In fig. 5.10 we show a comparison between three selected noise spectra for different bias currents I_{bias}.

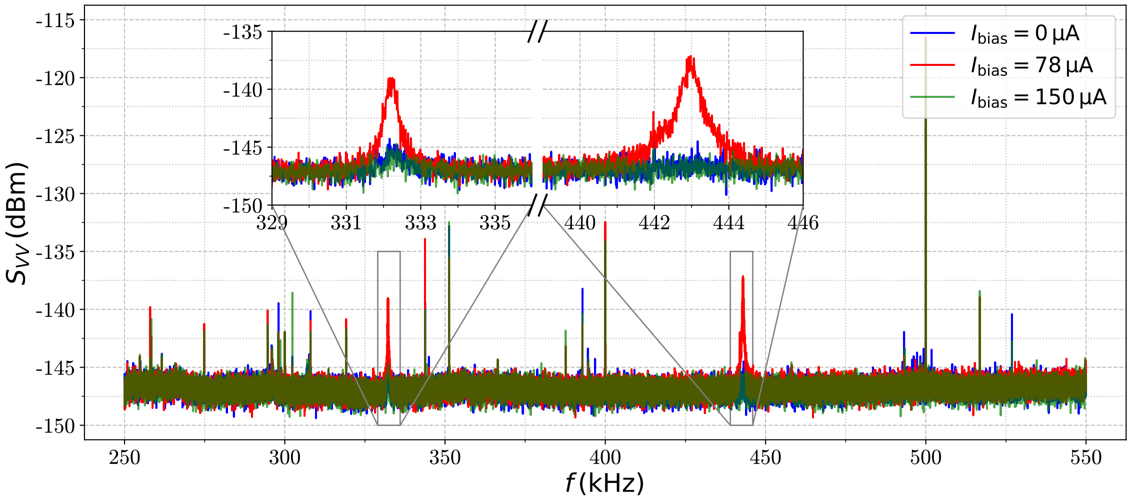

Figure 5.10: Noise spectra for different SQUID bias currents I_{bias}. The spectral noise density of the SQUID voltage S_{VV} is plotted vs. frequency f for three values of I_{bias}. The insets highlight interesting peaks, where the signal strength is greatly enhanced if the SQUID is tuned to the configuration with the highest flux sensitivity.

We compare the case of $I_{\text{bias}} = 0\,\mu\text{A}$, where the SQUID is completely insensitive to a flux change, with a spectrum where the SQUID is tuned to the point of maximum flux sensitivity for $I_{\text{bias}} = 78\,\mu\text{A}$, see section 5.1.2. Also a third trace for

$I_{\text{bias}} = 150\,\mu\text{A}$ is shown. At this point the SQUID is clearly in the normal conducting resistive state and should therefore also be completely flux insensitive.

It is obvious that some prominent peaks meet the described conditions to be identified as flux signals. Two particularly pronounced peaks are highlighted in the plot insets. The signal around 443 kHz clearly rises about 10 dB from the noise floor and the flux insensitive traces are completely flat. In contrast, the second feature at approximately 332 kHz is visible in all three spectra, but still enhanced by about 5 dB for the measurement at the flux sensitive working point.

These first noise scans are a good indication, that our SQUID is able to sense AC magnetic fields in the relevant frequency range, i.e. $f \leq 1\,\text{MHz}$. On the other hand, the noise peaks we observed may originate from any magnetic field noise present at the position of the SQUID and are not necessarily connected to the cantilever. In the following, we switch to the noise scan of a broader frequency range to get a better overview of sources of magnetic flux noise. Figure 5.11 illustrates the noise spectra for the bias current sweep, along with some evaluations of characteristic traces.

A first inspection of fig. 5.11 gives new insights on the noise peaks of fig. 5.10. We can clearly see a series of harmonics with a frequency spacing of roughly 111 kHz that the SQUID only picks up in the flux sensitive bias current region. In the colour plot, these are represented by the horizontal lines that appear at approximately 25 µA and fade out at about 90 µA. The eigenmode frequencies of a cantilever do not follow such a harmonic spectrum, cf. section 2.3.1. Therefore, we have to reject the cantilever as the origin of the broad noise peaks. We can suspect a pulsed periodic signal with a base frequency equal to the 111 kHz peak spacing as the source of the observed noise. It is likely that the signal stems from some kind of switching mode power supply and that it is carried into the cryostat via the ground connection or couples to some signal lines that are routed in the vicinity of the SQUID.

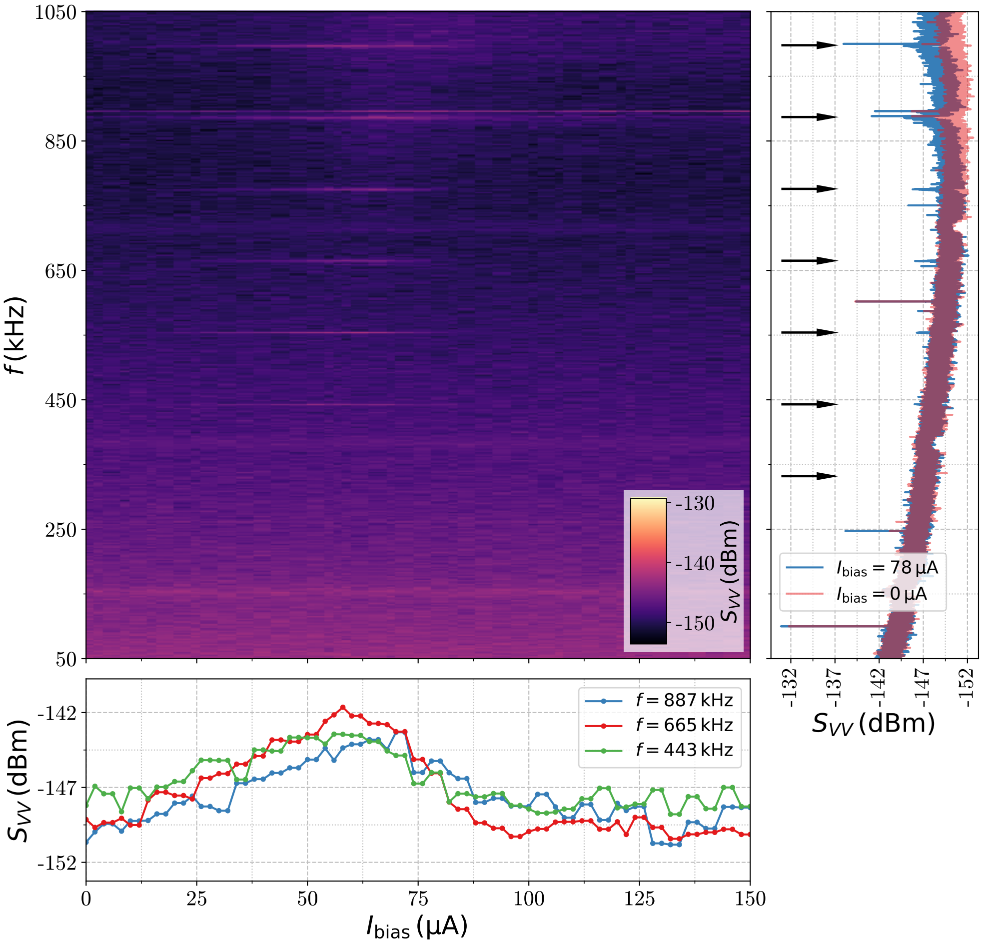

Figure 5.11: Compilation of the noise spectrum measurements with a broad frequency range and a sweep of the SQUID bias current I_{bias}. The main plot shows recorded spectra for different bias currents I_{bias}, where the magnitude of the noise spectral density S_{VV} of the SQUID voltage V is expressed by the colour coding. In the sub plot on the right, we compare the spectrum for $I_{\text{bias}} = 0\,\mu\text{A}$ with the configuration with maximum flux sensitivity at $I_{\text{bias}} = 78\,\mu\text{A}$. Arrows mark the position of characteristic peaks. The associated noise rise in the flux sensitive bias current region of the SQUID is illustrated in the bottom figure for some selected peaks.

In the bottom plot in fig. 5.11, we illustrate the spectral noise density S_{VV} vs. the bias current I_{bias} for three of the observed peaks. These lines represent cuts of the main plot at selected frequencies. The deviation in the baseline of the curves is a consequence of the varying noise floor for different frequencies, as can be seen in the right plot in fig. 5.11. We obtain the characteristic behaviour that we expect from a magnetic flux signal with a strong noise rise for bias currents with high flux sensitivity of the SQUID. Interestingly, the point with maximum sensitivity seems to have shifted to a lower value of $I_{\text{bias}} \approx 60\,\mu\text{A}$. The reason for this is unknown. The SQUID characteristics in section 5.1 was however determined for constant bias flux signals. Possibly the dynamically changing flux causes a deviation from that behaviour.

The sub plot in fig. 5.11 on the right compares the noise background, measured for $I_{\text{bias}} = 0$, to the trace for which the SQUID is tuned to the maximum flux sensitivity, cf. fig. 5.10. On the one hand, one can see the emergence of the broad noise peaks, whose positions are marked with arrows. On the other hand, we can also find additional peaks with a very narrow frequency profile, that are not present in the background trace. In the main graph these features are not clearly visible, due to the limited resolution and contrast of the colour plot. A thorough inspection finds that some of those peaks also fulfil the above mentioned criterion to be identified as a magnetic flux signal.

In order to get a better idea of what signal level and shape we should expect from the nanoparticle cantilever, we perform a rough estimation in the following. Let us assume that our mechanical oscillator has a resonance frequency of $f_{\text{R}} = 553\,\text{kHz}$. From a typical quality factor of $Q = 1 \times 10^4$ [35], we would then obtain a FWHM peak width of $\Gamma = f_{\text{R}}/Q \approx 55\,\text{Hz}$. The feature will therefore have a quite narrow frequency profile, assuming that the amplitude is small. On top of that, the lowest frequency resolution in our scans is approximately 30 Hz, which means that the signal might be confined to only a few points in the spectrum trace.

To estimate the noise magnitude, we start with calculating the effective mass m^* for the fundamental mode of the oscillator. We can model the mass m_{beam} that is distributed along the beam axis as a point mass attached to the end of a massless beam. The latter is equivalent to the effective mass and one finds the relation [36, 37]

$$m^* = 0.24 \cdot m_{\text{beam}}. \tag{5.4.1}$$

With the cantilever dimensions of $l = 100\,\mu\text{m}$, $w = 50\,\mu\text{m}$ and $h = 4\,\mu\text{m}$, as well as the density for silicon given in ref. [12], we determine the effective mass of the cantilever to be $m^* = 1.1 \times 10^{-11}\,\text{kg}$. According to eq. (2.3.12) and eq. (2.3.10) we can then calculate the RMS displacement due to the thermal motion of the oscillator,

$$u_{\mathrm{rms}} = \sqrt{\langle u^2 \rangle} = \sqrt{\frac{k_{\mathrm{B}}T}{m^* \omega_{\mathrm{R}}^2}} = 0.32\,\mathrm{pm}. \tag{5.4.2}$$

For this we assumed a temperature of $T = 1\,\mathrm{K}$.

To determine the magnitude of the magnetic flux noise caused by the cantilever oscillation, we model the effect of the magnetite (Fe_3O_4) nanoparticles that sit on the tip of the beam as a magnetic dipole. The crucial quantity that we need to estimate is therefore the total magnetic moment of the ensemble of particles along the oscillation direction $\vec{e}_z$. We can start with calculating the necessary magnetic moment m_{mag} for creating $1\,\Phi_0$ of static flux induced in the SQUID loop, according to

$$\Phi_{\mathrm{np}}(z_{\mathrm{dist}}) = \int_{-d_{\mathrm{y}}/2}^{d_{\mathrm{y}}/2} \int_{-d_{\mathrm{x}}/2}^{d_{\mathrm{x}}/2} B_{\mathrm{z,np}}(x, y, z_{\mathrm{dist}}) \mathrm{d}x \mathrm{d}y. \tag{5.4.3}$$

Here $d_{\mathrm{x}} = 13\,\mu\mathrm{m}$ and $d_{\mathrm{y}} = 36\,\mu\mathrm{m}$ are the dimensions of one of the gradiometer loops of the SQUID on top of which the cantilever tip is placed. The magnetic field of a dipole with the magnetic moment along the oscillation direction $\vec{m} = m\vec{e}_z$ is described in spherical coordinates by

$$\vec{B}_{\mathrm{np}} = \frac{\mu_0}{4\pi} \frac{m}{r^3} \left[2\cos(\theta)\vec{e}_r + \sin(\theta)\vec{e}_\theta\right]. \tag{5.4.4}$$

If we assume a distance of $d = 1\,\mu\mathrm{m}$ between cantilever tip and SQUID loop, we can determine m_{mag} from $\Phi_{\mathrm{np}}(d) = \Phi_0$ to be

$$m_{\mathrm{mag}} = 3 \times 10^{-14}\,\mathrm{Am}^2. \tag{5.4.5}$$

This is the total magnetic moment of the nanoparticles that is necessary to create $1\,\Phi_0$ of static induced flux in the SQUID loop. If we compare this value to the magnetic moment of a single magnetite nanoparticle $m_{\mathrm{mag,np}} = 1.7 \times 10^{-18}\,\mathrm{Am}^2$ [18, 38], we calculate the net number of particles that are perfectly aligned along the oscillation axis to be $N_{\mathrm{np}} \approx 18\,000$. From fig. 3.14 we estimate that a total volume of $20\,\mu\mathrm{m} \times 20\,\mu\mathrm{m} \times 200\,\mathrm{nm} \approx 0.1\,\mathrm{pl}$ is covered with nanoparticles. Compared to the stated particle concentration in ref. [18] we would get a total number of deposited particles of $N_{\mathrm{np,tot}} = 74\,000$, meaning that the magnetic polarisation would have to be relatively large, roughly 25 %.

If we, on the other hand, consider an initially unpolarised ensemble of nanoparticles, that we align by applying the bias field of our coil, the total magnetic moment is substantially lower. In ref. [39], we find a normalized magnetic moment of $\widetilde{m}_{\mathrm{mag}} = 0.31\,\mathrm{Am^2/kg}$ measured at a field strength of 3.8 mT. This article also shows that the dependence of $\widetilde{m}_{\mathrm{mag}}$ on the externally applied magnetic field can be linearised for small field strengths, to good approximation. We estimate the maximum externally applied magnetic field with eq. (5.2.2) for $I_{\mathrm{coil}}^{\mathrm{max}} = 40\,\mathrm{mA}$ to be $B_{\mathrm{z}} \approx 2\,\mathrm{mT}$. It is assumed that the hysteresis effects of the nanoparticle magnetization at such low temperatures preserve the magnetic polarisation to a large degree, cf. ref. [18]. Therefore we can determine the total magnetic moment, making use of the stated particle mass concentration $\rho_{\mathrm{np}} = 21.7\,\mathrm{mg/ml}$ [18], to be

$$m_{\mathrm{mag}} = \widetilde{m}_{\mathrm{mag}} \rho_{\mathrm{np}} V \frac{2\,\mathrm{mT}}{3.8\,\mathrm{mT}} = 4 \times 10^{-16}\,\mathrm{Am^2}, \tag{5.4.6}$$

where we again assumed a deposited volume of $V = 0.1\,\mathrm{pl}$. This magnetic moment results in a static induced flux of $\Phi_{\mathrm{np}}(d) = 1.3 \times 10^{-2}\,\Phi_0$.

If we now turn to the dynamic case and assume a harmonic oscillation of the cantilever with a displacement amplitude of u_{rms}, we can approximate the amplitude of the change in magnetic flux as

$$\Delta\Phi_{\mathrm{np}} = \frac{\Phi_{\mathrm{np}}(d - u_{\mathrm{rms}}) - \Phi_{\mathrm{np}}(d + u_{\mathrm{rms}})}{2} = 2.13 \times 10^{-10}\,\Phi_0. \tag{5.4.7}$$

We can also express this result in terms of a variation of the SQUID output voltage by using the flux-to-voltage transfer coefficient V_Φ at maximum flux sensitivity from section 5.1.2. This leads to a voltage amplitude of

$$\Delta V_{\mathrm{np}} = V_\Phi \Delta\Phi_{\mathrm{np}} = 0.14\,\mathrm{pV}. \tag{5.4.8}$$

Obviously, this value is extremely small. If we compare it with the noise floor level in our spectra of $-147\,\mathrm{dBm} \mathrel{\hat{=}} 10\,\mathrm{nV}$, we obtain that our signal is more than four orders of magnitude smaller than the noise. With such a low SNR there is no chance of measuring a signal from the cantilever. Hence, the improvised approach with magnetic nanoparticles as a magnetised material for the cantilever tip did not prove successful. A revised experimental setup will have to either rely on the Meissner effect scheme of the initial proposal for the experiment, see section 2.4, or find a way to increase the magnetic moment of the cantilever tip substantially.

5.4.2 Bias coil current scan

We carried out a second measurement in the search for a signal from the cantilever, where we varied the coil current I_{coil} while keeping the SQUID bias current constant at $I_{\mathrm{bias}} = 60\,\mu\mathrm{A}$, the value for which we observed the highest noise peak amplitudes in section 5.4.1. The main motivation for this test is an expected shift in the cantilever resonance frequency due to the force that is exerted on the magnetic material on the tip of the beam. We can describe this force according to

$$\begin{aligned}\vec{F} &= \vec{\nabla}(\vec{m}\cdot\vec{B}) = \vec{\nabla}\left[m_{\mathrm{z}}(B_{\mathrm{z}})\ B_{\mathrm{z}}\right] = \chi\vec{\nabla}(B_{\mathrm{z}}^2) = \\ &= 2m_{\mathrm{z}}\vec{\nabla}B_{\mathrm{z}} = 2m_{\mathrm{z}}\left(\frac{\partial B_{\mathrm{z}}}{\partial\rho}\vec{e}_\rho + \frac{\partial B_{\mathrm{z}}}{\partial z}\vec{e}_z\right) \approx 2m_{\mathrm{z}}\frac{\partial B_{\mathrm{z}}}{\partial z}\vec{e}_z, \end{aligned} \tag{5.4.9}$$

where $\vec{m} = m_{\mathrm{z}}\vec{e}_z$ is the magnetic moment of the nanoparticles and $\vec{B}$ is the magnetic field generated by the bias coil. We used that the nanoparticle magnetisation is linear in the magnetic field strength, $m_{\mathrm{z}}(B_{\mathrm{z}}) = \chi B_{\mathrm{z}}$, and neglected the gradient contribution of B_{z} along the radial direction, which is roughly 5 % of $\frac{\partial B_{\mathrm{z}}}{\partial z}$ at the position of the cantilever.

The noise spectra that we recorded for different coil currents in a range of $I_{\mathrm{coil}} = 0-40\,\mathrm{mA}$ are shown in fig. 5.12. A detailed inspection of the visible noise peaks does not provide any candidates for which the described resonance frequency shift could be observed. Following the reasoning in section 5.4.1, this is another indication that we are not able to sense a signal from the cantilever in the given configuration of the experiment.

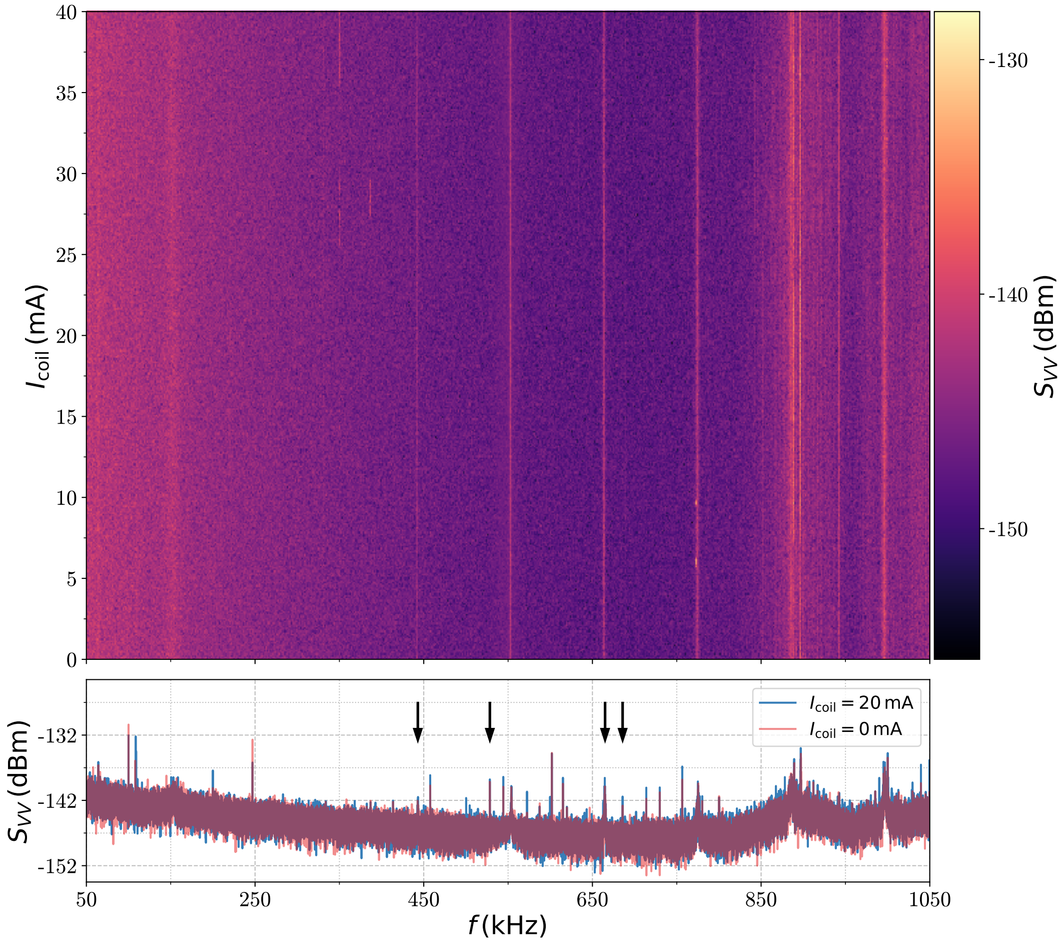

Figure 5.12: Noise spectrum measurements for a sweep of the coil current I_{coil}. The main plot is a representation of the recorded noise spectra with the frequency f on the horizontal axis, the coil current I_{coil} on the vertical axis and the spectral noise density of the SQUID output voltage S_{VV} encoded in the colour of the points. Below, a comparison between the $I_{\mathrm{coil}} = 0\,\mathrm{mA}$ and $I_{\mathrm{coil}} = 20\,\mathrm{mA}$ traces shows, that the noise spectra are virtually identical. The arrows mark the position of the noise peaks, for which a further analysis in terms of noise magnitude and peak position is carried out in fig. 5.13.

Exemplary, the position and the magnitude of some selected peaks are presented in fig. 5.13. We chose two of the peaks with the broad frequency profile that were studied in section 5.4.1 and randomly selected two of the very narrow features. The respective frequencies are marked with arrows in the sub figure in fig. 5.12. For the broad peaks, position and magnitude were determined from a Lorentzian peak fit, whereas for the narrow ones the determined frequency was constant within the scope of our measurement accuracy. Therefore, only the associated magnitude is presented.

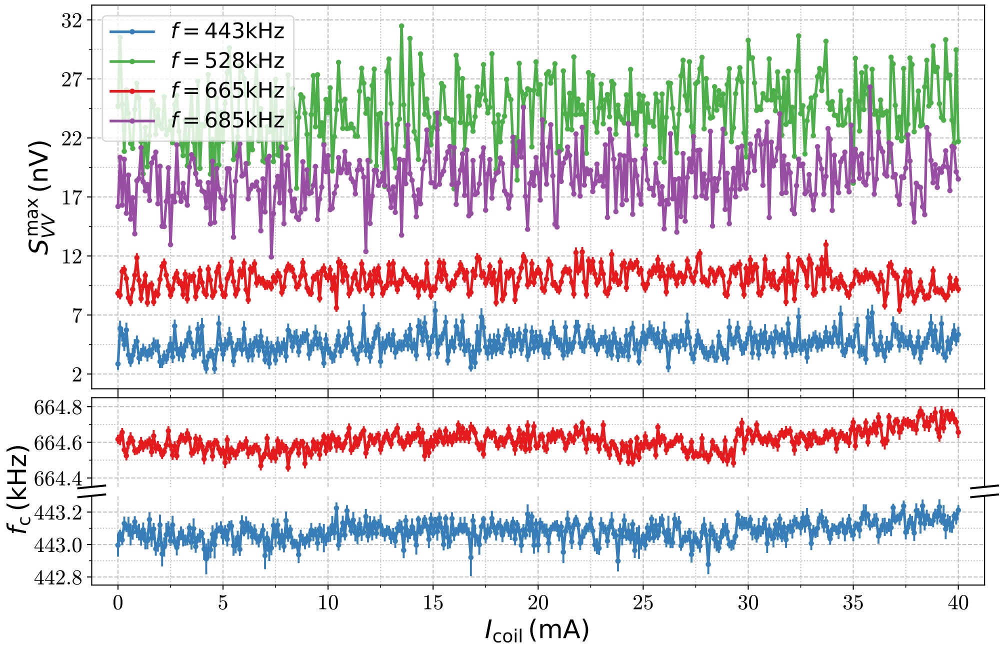

Figure 5.13: Analysis of selected noise peaks in terms of magnitude and peak position. The top plot shows the dependence of the noise magnitude on the coil current I_{coil}. The maximum in the spectral noise density $S_{VV}^{\max}$ is determined from a Lorentzian peak fit in the case of a noise peak with a broad frequency profile (red and blue line). For a narrow peak we plot the maximum value. In the bottom figure, the centre frequency of the Lorentzian peak fits for the broad noise signals are shown. We cannot observe a clear trend in the peak position for increasing coil currents.

Even though no indication of a signal from the cantilever was found, we would like to estimate the expected shift in the resonance frequency. For this, we model the effect of the magnetic force in eq. (5.4.9) as an additional mass $m_{\mathrm{F}} = F/g$ that is attached to the cantilever tip, with g being the gravitational acceleration. Recalling the result for the effective mass of the oscillator m^* from eq. (5.4.1), one obtains the resonance frequency for the loaded cantilever [36, 37]

$$f_{\text{loaded}} = \frac{1}{2\pi}\sqrt{\frac{k}{m^* + m_{\mathrm{F}}}} = f_0\sqrt{\frac{m^*}{m^* + m_{\mathrm{F}}}}, \tag{5.4.10}$$

with k being the cantilever spring constant and f_0 the unperturbed resonance frequency.

If we plug in the numbers from section 5.4.1, i.e. the magnetic moment of the nanoparticles $m_{\mathrm{z}} = 4 \times 10^{-16}\,\mathrm{Am}^2$ and the effective cantilever mass $m^* = 1.1 \times 10^{-11}\,\mathrm{kg}$, and we calculate the magnetic field gradient at the cantilever position from eq. (5.2.2) for $I_{\mathrm{coil}} = 40\,\mathrm{mA}$ (see sections 3.4 and 5.1.2 for geometry parameters), we obtain a maximum frequency shift of

$$f_{\mathrm{loaded}} - f_0 \approx 2\,\mathrm{Hz}. \tag{5.4.11}$$

This value is too low to resolve the shift in our noise spectra. However, the force on the cantilever tip scales linearly with the magnetic moment m_{z}. This means that by increasing m_{z}, which is a necessity to be able to detect a signal from the cantilever as we have seen in section 5.4.1, we also increase the frequency shift. In an improved experimental setup, this method could therefore be useful to discriminate a signal from the mechanical oscillator from other sources of noise.

Chapter 6

Conclusions and Outlook

The initial period of setting up our experiment was dominated by characterisation procedures for our DC SQUID. In section 5.1, we describe various SQUID measurements and determine characteristic parameters. We find that the modulation depth for the critical current is substantially lower than intended, which is attributed to issues in the fabrication process. This presents a major limitation for the detection of a cantilever signal as it decreases the flux-to-voltage transfer coefficient V_Φ. Further, the flux tuning of our SQUIDs is problematic, due to shorts in the designated flux bias loops. We hence have to use the large bias coil to tune the SQUIDs, which prevents the use of the flux-locked loop (FLL) readout technique. With FLL we would expect a lower detection threshold for the cantilever signal, because the SQUID can be constantly operated at the point with maximum flux sensitivity. The numerical simulations for the SQUID I-Φ-V characteristic curve in section 5.1.4 lead to the conclusion, that improvements in noise filtering of the SQUID control lines is urgently required. This will enhance the modulation depth of the critical current and lower the noise floor, which will ease the cantilever detection.

Considering the setup described in section 2.4 and the proposal for our experiment, we demonstrate the use of a current of 1 A in a cryostat, which supplies our bias coil. A similar demonstration for the quadrupole line on the SQUID chip is not possible, because we identify unwanted connections to the SQUIDs that would put the sensitive JJs at risk for such high currents.

The detection of a signal from the mechanical oscillator was not accomplished in the first iteration of our experiment, as explained in section 5.4. We aligned two cantilever beams to our SQUID structures, one with a strip of Cr and one with magnetite Fe_3O_4 nanoparticles on its tip. The SQUID with the Cr cantilever failed for an unknown reason. This left us with the nanoparticle cantilever, where we attempted to deposit a material that can be magnetised on the tip of the beam. In section 5.4.1, we find multiple peaks that can be identified as magnetic flux signals in the noise spectrum of the SQUID output voltage. However, none of the peaks can be related to the cantilever. We suspect a switching mode power supply as the source of the noise.

We close the section with some estimates on the cantilever signal intensity. These clearly support a noise amplitude below the detection limit. A substantial increase in the magnetic moment of the beam tip by roughly four orders of magnitude would be necessary for detecting the mechanical oscillator. This can either be achieved with the Meissner effect method described in the proposal, or by polarising the nanoparticles in a strong magnetic field during the application.

Finally, in section 5.4.2 we estimate the effect of an increasing bias field on the cantilever resonance frequency. In our current arrangement, we obtain a shift of only 2 Hz. This shift would be enhanced with an increased magnetic moment. Hence, in an improved setup, this method could help in distinguishing a cantilever signal from other sources of flux noise.

With fully functional SQUID samples and a cantilever with SC Nb on the tip, a detection of the mechanical oscillator seems to be within reach. After that, one can think about possible cooling mechanisms. Some of our SQUIDs were already equipped with an additional feedback loop that could be used for direct feedback cooling or parametric cooling. The major milestones for a future version of our experiment will be cooling to the motional ground state and eventually tackling the strong single photon coupling. This would open a wide range of possible quantum mechanics experiments for our hybrid device.

Bibliography

[1] A. D. O'Connell et al. "Quantum ground state and single-phonon control of a mechanical resonator". In: *Nature* 464 (Mar. 2010), p. 697. URL: `http://dx.doi.org/10.1038/nature08967`.

[2] T. A. Palomaki et al. "Entangling Mechanical Motion with Microwave Fields". In: *Science* 342.6159 (2013), pp. 710–713. ISSN: 0036-8075. DOI: `10.1126/science.1244563`. URL: `http://science.sciencemag.org/content/342/6159/710`.

[3] Simon Gröblacher et al. "Observation of strong coupling between a micromechanical resonator and an optical cavity field". In: *Nature* 460 (Aug. 2009), p. 724. URL: `http://dx.doi.org/10.1038/nature08171`.

[4] A. P. Reed et al. "Faithful conversion of propagating quantum information to mechanical motion". In: *Nature Physics* 13 (Sept. 2017), p. 1163. URL: `http://dx.doi.org/10.1038/nphys4251`.

[5] Guillem Via, Gerhard Kirchmair, and Oriol Romero-Isart. "Strong Single-Photon Coupling in Superconducting Quantum Magnetomechanics". In: *Phys. Rev. Lett.* 114 (14 Apr. 2015), p. 143602. DOI: `10.1103/PhysRevLett.114.143602`. URL: `https://link.aps.org/doi/10.1103/PhysRevLett.114.143602`.

[6] Rudolf Gross and Achim Marx. "Applied Superconductivity: Josephson Effect and Superconducting Electronics". Lecture notes. Oct. 2005. URL: `https://www.wmi.badw.de/teaching/Lecturenotes/index.html`.

[7] R. C. Jaklevic et al. "Quantum Interference Effects in Josephson Tunneling". In: *Phys. Rev. Lett.* 12 (7 Feb. 1964), pp. 159–160. DOI: `10.1103/PhysRevLett.12.159`. URL: `https://link.aps.org/doi/10.1103/PhysRevLett.12.159`.

[8] Reinhold Kleiner and Dieter Koelle. "Appendix 1: Basic Properties of Superconductivity". In: *The SQUID Handbook*. Wiley-VCH Verlag GmbH & Co. KGaA, 2005, pp. 357–366. ISBN: 9783527603640. DOI: `10.1002/3527603646.app1`. URL: `http://dx.doi.org/10.1002/3527603646.app1`.

[9] Menno Poot and Herre S.J. van der Zant. "Mechanical systems in the quantum regime". In: *Physics Reports* 511.5 (2012). Mechanical systems in the quantum regime, pp. 273–335. ISSN: 0370-1573. DOI: `https://doi.org/10.1016/j.physrep.2011.12.004`. URL: `http://www.sciencedirect.com/science/article/pii/S0370157311003644`.

[10] Markus Aspelmeyer, Tobias J. Kippenberg, and Florian Marquardt. "Cavity optomechanics". In: *Rev. Mod. Phys.* 86 (4 Dec. 2014), pp. 1391–1452. DOI: `10.1103/RevModPhys.86.1391`. URL: `https://link.aps.org/doi/10.1103/RevModPhys.86.1391`.

[11] M. A. Hopcroft, W. D. Nix, and T. W. Kenny. "What is the Young's Modulus of Silicon?" In: *Journal of Microelectromechanical Systems* 19.2 (Apr. 2010), pp. 229–238. ISSN: 1057-7157.

[12] *Material properties: Silicon (Si), bulk.* MEMSnet. Feb. 2018. URL: `https://www.memsnet.org/material/siliconsibulk/`.

[13] R. W. Andrews et al. "Bidirectional and efficient conversion between microwave and optical light". In: *Nature Physics* 10 (Mar. 2014), p. 321. URL: `http://dx.doi.org/10.1038/nphys2911`.

[14] Thorsten Fredrick Stromberg. "The superconducting properties of high purity niobium". Digital Repository @ Iowa State University, http://lib. dr. iastate. edu/. PhD thesis. Iowa State University, 1965. URL: `https://lib.dr.iastate.edu/rtd/3283`.

[15] Raúl Toral and Pere Colet. “Numerical Simulation of Stochastic Differential Equations”. In: *Stochastic Numerical Methods: An Introduction for Students and Scientists*. Wiley-VCH Verlag GmbH & Co. KGaA, 2014. Chap. 7, pp. 191–234. ISBN: 9783527683147. DOI: `10.1002/9783527683147.ch7`. URL: `http://dx.doi.org/10.1002/9783527683147.ch7`.

[16] Daniel T. Gillespie. “The mathematics of Brownian motion and Johnson noise”. In: *American Journal of Physics* 64.3 (1996), pp. 225–240. DOI: `10.1119/1.18210`. eprint: `https://doi.org/10.1119/1.18210`. URL: `https://doi.org/10.1119/1.18210`.

[17] Matthias Rudolph. “Development of an ultra-low field magnetic resonance imaging scanner and DC SQUID based current sensors for the investigation of hyperpolarization techniques”. PhD thesis. Universität Tübingen, Dec. 2018. DOI: `10.15496/publikation-21202`. URL: `https://publikationen.uni-tuebingen.de/xmlui/handle/10900/79806`.

[18] *Magnetic Nanoparticles*. nanoComposix. Jan. 2018. URL: `https://nanocomposix.eu/collections/magnetic-nanoparticles`.

[19] F. Teyssandier and D. Prêle. “Commercially Available Capacitors at Cryogenic Temperatures”. In: *Ninth International Workshop on Low Temperature Electronics - WOLTE9*. Guaruja, Brazil, June 2010. URL: `https://hal.archives-ouvertes.fr/hal-00623399/file/PRELE_Wolte9.pdf`.

[20] S. S. Gerber. “Performance of high-frequency high-flux magnetic cores at cryogenic temperatures”. In: *Energy Conversion Engineering Conference, 2002. IECEC ’02. 2002 37th Intersociety*. 2002, pp. 249–254.

[21] *Magnetic shielding theory - Formulas & calculations*. Amuneal Manufacturing Corp. 2017. URL: `http://www.amuneal.com/magnetic-shielding/theory-design/formulas-calculations`.

[22] R. Huebener et al. “Critical current density in superconducting niobium films”. In: *IEEE Transactions on Magnetics* 11.2 (Mar. 1975), pp. 344–346. ISSN: 0018-9464. DOI: `10.1109/TMAG.1975.1058718`.

[23] R. de Bruyn Ouboter and A.Th.A.M. de Waele. “Chapter 6 Superconducting Point Contacts Weakly Connecting Two Superconductors”. In: *Progress in Low Temperature Physics*. Ed. by C.J. Gorter. Vol. 6. Elsevier, 1970, pp. 243–290. DOI: `https://doi.org/10.1016/S0079-6417(08)60065-7`. URL: `http://www.sciencedirect.com/science/article/pii/S0079641708600657`.

[24] Claudia D. Tesche and John Clarke. “dc SQUID: Noise and optimization”. In: *Journal of Low Temperature Physics* 29.3 (Nov. 1977), pp. 301–331. ISSN: 1573-7357. DOI: `10.1007/BF00655097`. URL: `https://doi.org/10.1007/BF00655097`.

[25] John Clarke and Alex I. Braginski. *The SQUID Handbook: Vol. I Fundamentals and Technology of SQUIDs and SQUID Systems*. Vol. 1. Wiley-VCH, 2006. URL: `http://onlinelibrary.wiley.com/book/10.1002/3527603646`.

[26] Boris Chesca, Reinhold Kleiner, and Dieter Koelle. “SQUID Theory”. In: *The SQUID Handbook*. Wiley-VCH Verlag GmbH & Co. KGaA, 2005. Chap. 2, pp. 29–92. ISBN: 9783527603640. DOI: `10.1002/3527603646.ch2`. URL: `http://dx.doi.org/10.1002/3527603646.ch2`.

[27] V. J. de Waal, P. Schrijner, and R. Llurba. “Simulation and optimization of a dc SQUID with finite capacitance”. In: *Journal of Low Temperature Physics* 54.3 (Feb. 1984), pp. 215–232. ISSN: 1573-7357. DOI: `10.1007/BF00683275`. URL: `https://doi.org/10.1007/BF00683275`.

[28] J. Muller et al. “Voltage-flux-characteristics of asymmetric dc SQUIDs”. In: *IEEE Transactions on Applied Superconductivity* 11.1 (Mar. 2001), pp. 912–915. ISSN: 1051-8223.

[29] J. R. Rairden and C. A. Neugebauer. “Critical temperature of niobium and tantalum films”. In: *Proceedings of the IEEE* 52.10 (Oct. 1964), pp. 1234–1238. ISSN: 0018-9219. DOI: `10.1109/PROC.1964.3311`.

[30] C. Y. Ho et al. “Electrical Resistivity of Ten Selected Binary Alloy Systems”. In: *Journal of Physical and Chemical Reference Data* 12.2 (1983), pp. 183–322. DOI: `10.1063/1.555684`. eprint: `https://doi.org/10.1063/1.555684`. URL: `https://doi.org/10.1063/1.555684`.

[31] J. Ekin. *Experimental Techniques for Low-Temperature Measurements.* Oxford University Press, Oct. 2006. DOI: `10.1093/acprof:oso/9780198570547.001.0001`. URL: `https://doi.org/10.1093/acprof:oso/9780198570547.001.0001`.

[32] J. A. Nelder and R. Mead. "A Simplex Method for Function Minimization". In: *The Computer Journal* 7.4 (1965), pp. 308–313. DOI: `10.1093/comjnl/7.4.308`. eprint: `/oup/backfile/content_public/journal/comjnl/7/4/10.1093/comjnl/7.4.308/2/7-4-308.pdf`. URL: `+%20http://dx.doi.org/10.1093/comjnl/7.4.308`.

[33] David J. Wales and Jonathan P. K. Doye. "Global Optimization by Basin-Hopping and the Lowest Energy Structures of Lennard-Jones Clusters Containing up to 110 Atoms". In: *The Journal of Physical Chemistry A* 101.28 (1997), pp. 5111–5116. DOI: `10.1021/jp970984n`. eprint: `http://dx.doi.org/10.1021/jp970984n`. URL: `http://dx.doi.org/10.1021/jp970984n`.

[34] *Fine SC Wires.* Supercon, Inc. Mar. 2018. URL: `http://www.supercon-wire.com/content/fine-sc-wires`.

[35] Jannis Lübbe et al. "Determining cantilever stiffness from thermal noise". In: *Beilstein Journal of Nanotechnology* 4 (2013), pp. 227–233. ISSN: 2190-4286. DOI: `10.3762/bjnano.4.23`.

[36] J. P. Cleveland et al. "A nondestructive method for determining the spring constant of cantilevers for scanning force microscopy". In: *Review of Scientific Instruments* 64.2 (1993), pp. 403–405. DOI: `10.1063/1.1144209`. eprint: `https://doi.org/10.1063/1.1144209`. URL: `https://doi.org/10.1063/1.1144209`.

[37] E Macho-Stadler, M J Elejalde-García, and R Llanos-Vázquez. "Oscillations of end loaded cantilever beams". In: *European Journal of Physics* 36.5 (2015), p. 055007. URL: `http://stacks.iop.org/0143-0807/36/i=5/a=055007`.

[38] Sibylle Sievers et al. "Quantitative Measurement of the Magnetic Moment of Individual Magnetic Nanoparticles by Magnetic Force Microscopy". In: *Small*

8.17 (2012), pp. 2675–2679. ISSN: 1613-6829. DOI: `10.1002/smll.201200420`. URL: `http://dx.doi.org/10.1002/smll.201200420`.

[39] Natalie L. Adolphi et al. “Characterization of Single-core Magnetite Nanoparticles for Magnetic Imaging by SQUID-relaxometry”. In: *Physics in medicine and biology* 55.19 (Sept. 2010), pp. 10.1088/0031–9155/55/19/023. ISSN: 1361-6560. URL: `http://www.ncbi.nlm.nih.gov/pmc/articles/PMC3883308/`.

Appendix A

SDE Numerical simulation code: SQUID characteristics

In this appendix, I provide the code for the python library used to implement the numerical model of the SQUID I-Φ-V characteristics. The optimization routine follows at the end of the chapter.

```python
import numpy as np
import scipy.constants as scpconst
from multiprocessing import Pool
import parmap as pm
import tqdm as tqdm

Phi0 = scpconst.value('mag. flux quantum')

def wIntOU(hStep, gamma, tau, wOld=None, f1Old=None, f2Old=None):
    """
    ------------------------------------
    Description:
    ------------------------------------
    Numerical implementation of the Ornstein-Uhlenbeck noise integral.

    ------------------------------------
    Function arguments:
    ------------------------------------
    hStep:        Float. Step size of numerical simulation as a fraction of the
                  inverse of the characteristic angular frequency
                  wc = 2 pi I0 R / Phi0.
    gamma:        Float. Noise parameter gamma = 2 pi kB T / (I0 Phi0).
    tau:          Float. Ornstein-Uhlenbeck relaxation time. Normalised to wc.
                  tau = wc / fMax  with fMax corner frequency in noise power
                  spectral density -> fMax ~ equivalent noise bandwidth 'ENBW'.
    wOld:         Float. Resulting value for wIntOU of former iteration.
                  'None' for first function call/initialisation.
    f1Old, f2Old: Float. Random (correlated) variables of former iteration.
                  'None' for first function call/initialisation.

    ------------------------------------
    Returns:
    ------------------------------------
    wNew:         Float. New noise integral value for current iteration.
    f1New, f2New: Float. New random (correlated) variables of current iteration.
    """
```

```
    # determine Ornstein-Uhlenbeck diffusion constant from given parameters
    c = 2*gamma/tau**2

    # generation of correlated random numbers for OU noise integral wh
    p = np.exp(-hStep/tau)
    u, v = np.random.normal(size=2)

    f1New = tau*np.sqrt(c*hStep)*u
    f2New = (np.sqrt(c/hStep)*tau**2*(p - 1)*u +
             np.sqrt(c*tau**3*(1 - p)/2*(1 + p - 2*tau/hStep*(1 - p)))*v)

    if wOld is None:
        # initialisation in first call
        wNew = np.sqrt(c*tau**3/2)*(1 - p)*np.random.normal() + f1New + f2New
    else:
        # computation of wh that fulfils OU conditions
        wNew = p*(wOld - f1Old) + f1New - f2Old + f2New

    return wNew, f1New, f2New

def wIntWhiteNoise(hStep, gamma):
    """
    --------------------------------
    Description:
    --------------------------------
    Numerical implementation of the Gaussian white noise integral.

    --------------------------------
    Function arguments:
    --------------------------------
    hStep: Float. Step size of numerical simulation as a fraction of the inverse of
           the characteristic angular frequency wc = 2 pi I0 R / Phi0.
    gamma: Float. Noise parameter gamma = 2 pi kB T / (I0 Phi0).

    --------------------------------
    Returns:
    --------------------------------
    wNew:  Float. New noise integral value for current iteration.
    """
    # Determine intensity of Gaussian noise from given parameters.
    D = 2.*gamma

    # generation of white noise integral gh
    wNew = np.sqrt(D*hStep)*np.random.normal()

    return wNew

def heunSDEsquid(yInit, hStep, tEnd, method, iBias, phiA, gamma, betaC, betaL,
                 tau=None, alphaI=0., alphaR=0., alphaC=0., alphaL=0.,
                 noiseCurrOutput=True):
    """
    --------------------------------
    Description:
    --------------------------------
    Routine that implements the numerical Heun method as a solver of a
    stochastic numerical equation for the example of the SQUID RCSJ model.

    --------------------------------
    Function arguments:
    --------------------------------
    yInit:   Float array. Start values for junction phase (delta) and
             voltage (d delta/dt) variables.
             Structure: [delta1, delta1, u1, u2]
    hStep:   Float. Step size of numerical simulation as a fraction of the inverse
             of the characteristic angular frequency wc = 2 pi I0 R / Phi0.
    tEnd:    Float. Total simulation time. Normalised to wc^-1, tEnd = wc * tTot.
    method:  String. Decides which noise model is used. 'Gauss' for Gaussian noise
             and 'OU' for Ornstein-Uhlenbeck noise. For other choices the noise
             free case is simulated.
    iBias:   Float. SQUID bias current. Normalised to average critical current I0
             of one SQUID junction.
```

```
    phiA:     Float. SQUID flux bias. Normalised to Phi0.
    gamma:    Float. Noise parameter gamma = 2 pi kB T / (I0 Phi0).
    betaC:    Float. Steward-McCumber parameter. betaC = 2*pi*I0*R^2*C/Phi0
    betaL:    Float. Screening parameter. betaL = 2*L*I0/Phi0
    tau:      Float. Ornstein-Uhlenbeck relaxation time. Normalised to wc.
              tau = wc / fMax with fMax corner frequency in noise power
              spectral density -> fMax ~ equivalent noise bandwidth 'ENBW'.
              Not used, 'None', in the case of Gaussian noise.
    alphaI:   Float. Asymmetry parameter for critical currents of the two
              SQUID junctions. alphaI = (I0,2 - I0,1)/(I0,1 + I0,2)
    alphaR:   Float. Asymmetry parameter for shunt resistances of the two
              SQUID junctions. alphaR = (R1 - R2)/(R1 + R2)
    alphaC:   Float. Asymmetry parameter for shunt capacitances of the two
              SQUID junctions. alphaC = (C2 - C1)/(C1 + C2)
    alphaL:   Float. Asymmetry parameter for inductances of the two
              SQUID loop halves. alphaL = (L2 - L1)/(L1 + L2)
    noiseCurrOutput: Boolean. Decides whether the noise current data arrays are
                     included in the function returns. Used for the noise
                     characterisation. By default 'True'.

    --------------------------------
    Returns:
    --------------------------------
    tArray:   Float array. Array with time values for the simulation of the
              evolution of junction phases and voltages.
    yArray:   Float array. Data array with simulated values for the junction phases
              and voltages. Each value in tArray refers to a data array of the form:
              [delta1, delta2, u1, u2]
    iN1Array, iN2Array (optional): Float arrays. Simulated noise current values.
                                   Only returned if noiseCurrOutput == True.
    """
    # RESERVE MEMORY for simulation results
    tArray = np.append(np.arange(0, tEnd, hStep), np.ceil(tEnd/hStep)*hStep)

    if noiseCurrOutput:
        iN1Array = np.empty_like(tArray)
        iN2Array = np.empty_like(tArray)

    # call subroutine depending on noise model choice
    # for generation of noise variables
    if method == 'OU':
        wCurr_iN1, f1Curr_iN1, f2Curr_iN1 = wIntOU(hStep, gamma, tau)
        wCurr_iN2, f1Curr_iN2, f2Curr_iN2 = wIntOU(hStep, gamma, tau)
    elif method == 'Gauss':
        wCurr_iN1 = wIntWhiteNoise(hStep, gamma)
        wCurr_iN2 = wIntWhiteNoise(hStep, gamma)
    else: # no noise
        wCurr_iN1, wCurr_iN2 = np.zeros(2)

    # split arguments for detereministic drift function qDrift
    # and stochastic diffusion function gDiff
    p_q = [iBias, phiA, betaC, betaL, alphaI, alphaR, alphaC, alphaL]
    p_g = [gamma, betaC, betaL, alphaI, alphaR, alphaC, alphaL]

    if betaC == None:
        # RESERVE MEMORY for simulation results
        yArray = np.empty((np.alen(tArray), 2))

        # VARIABLE INITIALISATION
        yArray[0] = np.array(yInit)[:2]
        yOld = yArray[0]

        if noiseCurrOutput:
            iN1Array[0] = 1./hStep*np.dot(np.array([(-1.)*(1 - alphaR), 0]),
                                          wCurr_iN1*gDiffRSJ(0, yInit, *p_g))
            iN2Array[0] = 1./hStep*np.dot(np.array([0, (-1.)*(1 + alphaR)]),
                                          wCurr_iN2*gDiffRSJ(0, yInit, *p_g))

        # HEUN SDE CALCULATION
        for tIdx, tCurr in enumerate(tArray[0:-1]):
            # Runge-Kutta factors
```

```
            k = hStep*qDriftRSJ(tCurr, yOld, *p_q) # drift term k
            # diffusion term l
            l = np.dot(np.array([[wCurr_iN1, 0],
                                 [0, wCurr_iN2]]), gDiffRSJ(tCurr, yOld, *p_g))

            # contribution to diffusion term from noise currents
            gContr = 1/2 + np.dot(np.array([[wCurr_iN1/2, 0],
                                            [0, wCurr_iN2/2]]),
                                  gDiffRSJ(tCurr + hStep, yOld + k + l, *p_g))

            # calculate coordinate vector y and noise current magnitudes iN1 and
            # iN2 for t_i+1
            yArray[tIdx + 1] = (yOld + k/2 + gContr +
                              hStep/2*qDriftRSJ(tCurr + hStep, yOld + k + l, *p_q))

            if noiseCurrOutput:
                iN1Array[tIdx + 1] = (-1.)*(1. - alphaR)/hStep*gContr[0]
                iN2Array[tIdx + 1] = (-1.)*(1. + alphaR)/hStep*gContr[1]

            # store y value for next iteration and generate new random numbers
            # for noise currents
            yOld = yArray[tIdx + 1]

            if method == 'OU':
                wCurr_iN1, f1Curr_iN1, f2Curr_iN1 = wIntOU(hStep, gamma, tau,
                                                           wCurr_iN1, f1Curr_iN1,
                                                           f2Curr_iN1)
                wCurr_iN2, f1Curr_iN2, f2Curr_iN2 = wIntOU(hStep, gamma, tau,
                                                           wCurr_iN2, f1Curr_iN2,
                                                           f2Curr_iN2)
            elif method == 'Gauss':
                wCurr_iN1 = wIntWhiteNoise(hStep, gamma)
                wCurr_iN2 = wIntWhiteNoise(hStep, gamma)
            else: # no noise
                wCurr_iN1, wCurr_iN2 = np.zeros(2)

        # calculate voltages as derivative of phase values
        yArray = np.concatenate((yArray,
                                 (np.roll(yArray, -1, axis=0) -
                                  np.roll(yArray, 1, axis=0))/(2.*hStep)), axis=1)
        yArray[0][2:] = (yArray[1][:2] - yArray[0][:2])/hStep
        yArray[-1][2:] = (yArray[-1][:2] - yArray[-2][:2])/hStep

    else: # betaC != 0
        # RESERVE MEMORY for simulation results
        yArray = np.empty((np.alen(tArray), 4))

        # VARIABLE INITIALISATION
        yArray[0] = yInit
        yOld = yInit

        if noiseCurrOutput:
            iN1Array[0] = 1./hStep*np.dot(np.array([0,0,(-1.)*betaC*(1-alphaC),0]),
                                          wCurr_iN1*gDiff(0, yInit, *p_g))
            iN2Array[0] = 1./hStep*np.dot(np.array([0,0,0,(-1.)*betaC*(1+alphaC)]),
                                          wCurr_iN2*gDiff(0, yInit, *p_g))

        # HEUN SDE CALCULATION
        for tIdx, tCurr in enumerate(tArray[0:-1]):
            # Runge-Kutta factors
            k = hStep*qDrift(tCurr, yOld, *p_q) # drift term k
            # diffusion term l
            l = np.dot(np.array([[0, 0, 0, 0],
                                 [0, 0, 0, 0],
                                 [0, 0, wCurr_iN1, 0],
                                 [0, 0, 0, wCurr_iN2]]), gDiff(tCurr, yOld, *p_g))

            # contribution to diffusion term from noise currents
            gContr = 1/2 + np.dot(np.array([[0, 0, 0, 0],
                                            [0, 0, 0, 0],
                                            [0, 0, wCurr_iN1/2, 0],
```

```
                                              [0, 0, 0, wCurr_iN2/2]]),
                                   gDiff(tCurr + hStep, yOld + k + l, *p_g))

            # calculate coordinate vector y and noise current magnitudes iN1 and
            # iN2 for t_i+1
            yArray[tIdx + 1] = (yOld + k/2 + gContr +
                                 hStep/2*qDrift(tCurr + hStep, yOld + k + l, *p_q))

            if noiseCurrOutput:
                iN1Array[tIdx + 1] = (-1.)*betaC*(1. - alphaC)/hStep*gContr[2]
                iN2Array[tIdx + 1] = (-1.)*betaC*(1. + alphaC)/hStep*gContr[3]

            # store y value for next iteration and generate new random numbers
            # for noise currents
            yOld = yArray[tIdx + 1]

            if method == 'OU':
                wCurr_iN1, f1Curr_iN1, f2Curr_iN1 = wIntOU(hStep, gamma, tau,
                                                            wCurr_iN1, f1Curr_iN1,
                                                            f2Curr_iN1)
                wCurr_iN2, f1Curr_iN2, f2Curr_iN2 = wIntOU(hStep, gamma, tau,
                                                            wCurr_iN2, f1Curr_iN2,
                                                            f2Curr_iN2)
            elif method == 'Gauss':
                wCurr_iN1 = wIntWhiteNoise(hStep, gamma)
                wCurr_iN2 = wIntWhiteNoise(hStep, gamma)
            else: # no noise
                wCurr_iN1, wCurr_iN2 = np.zeros(2)


    if noiseCurrOutput:
        return tArray, yArray, iN1Array, iN2Array
    else:
        return tArray, yArray

def qDrift(t, y, iBias, phiA, betaC, betaL, alphaI, alphaR, alphaC, alphaL):
    """
    ---------------------------------
    Description:
    ---------------------------------
    Drift term in the SDE for the RCSJ model.

    ---------------------------------
    Function arguments:
    ---------------------------------
    t:         Float. Current timestep t_i. Normalised to wc^-1.
    y:         Float array. Current values for junction phase (delta) and voltage
               (d delta/dt) variables at timestep t.
               Structure: [delta1, delta2, u1, u2]
    iBias:     Float. SQUID bias current. Normalised to average critical current I0
               of one SQUID junction.
    phiA:      Float. SQUID flux bias. Normalised to Phi0.
    betaC:     Float. Steward-McCumber parameter. betaC = 2*pi*I0*R^2*C/Phi0
    betaL:     Float. Screening parameter. betaL = 2*L*I0/Phi0
    alphaI:    Float. Asymmetry parameter for critical currents of the two SQUID
               junctions. alphaI = (I0,2 - I0,1)/(I0,1 + I0,2)
    alphaR:    Float. Asymmetry parameter for shunt resistances of the two SQUID
               junctions. alphaR = (R1 - R2)/(R1 + R2)
    alphaC:    Float. Asymmetry parameter for shunt capacitances of the two SQUID
               junctions. alphaC = (C2 - C1)/(C1 + C2)
    alphaL:    Float. Asymmetry parameter for inductances of the two SQUID loop
               halves. alphaL = (L2 - L1)/(L1 + L2)

    ---------------------------------
    Returns:
    ---------------------------------
    q:         Float array. Drift term evaluated at (t_i, y(t_i)).
    """
    # auxiliary variables
    cL = 1./(betaL*np.pi)
    cCm = 1./(betaC*(1. - alphaC))
```

```
    cCp = 1./(betaC*(1. + alphaC))

    # Calculate deterministic drift contribution q to
    # new coordinate vector y for t_i+1
    q = (np.array([0,
                   0,
                   cCm*(iBias/2*(1. + alphaL) - 2*phiA/betaL),
                   cCp*(iBias/2*(1. - alphaL) + 2*phiA/betaL)]) +
         np.dot(np.array([[0, 0, 1, 0],
                          [0, 0, 0, 1],
                          [(-cL)*cCm, cL*cCm, (-1.)*(1. - alphaR)*cCm, 0],
                          [cL*cCp, (-cL)*cCp, 0, (-1.)*(1. + alphaR)*cCp]]), y) +
         np.dot(np.array([[0, 0, 0, 0],
                          [0, 0, 0, 0],
                          [(-1.)*(1. - alphaI)*cCm, 0, 0, 0],
                          [0, (-1.)*(1. + alphaI)*cCp, 0, 0]]), np.sin(y)))
    return q

def gDiff(t, y, gamma, betaC, betaL, alphaI, alphaR, alphaC, alphaL):
    """
    ----------------------------------
    Description:
    ----------------------------------
    Diffusion term in the SDE for the RCSJ model.

    ----------------------------------
    Function arguments:
    ----------------------------------
    t:        Float. Current timestep. Normalised to wc^-1.
    y:        Float array. Current values for junction phase (delta) and voltage
              (d delta/dt) variables at timestep t.
              Structure: [delta1, delta2, u1, u2]
    gamma:    Float. Noise parameter gamma = 2 pi kB T / (I0 Phi0).
    betaC:    Float. Steward-McCumber parameter. betaC = 2*pi*I0*R^2*C/Phi0
    betaL:    Float. Screening parameter. betaL = 2*L*I0/Phi0
    alphaI:   Float. Asymmetry parameter for critical currents of the two
              SQUID junctions. alphaI = (I0,2 - I0,1)/(I0,1 + I0,2)
    alphaR:   Float. Asymmetry parameter for shunt resistances of the two
              SQUID junctions. alphaR = (R1 - R2)/(R1 + R2)
    alphaC:   Float. Asymmetry parameter for shunt capacitances of the two
              SQUID junctions. alphaC = (C2 - C1)/(C1 + C2)
    alphaL:   Float. Asymmetry parameter for inductances of the two
              SQUID loop halves. alphaL = (L2 - L1)/(L1 + L2)

    ----------------------------------
    Returns:
    ----------------------------------
    g:        Float array. Diffusion term evaluated at (t_i, y(t_i)).
    """
    # auxiliary variables
    cCm = 1./(betaC*(1. - alphaC))
    cCp = 1./(betaC*(1. + alphaC))

    # Calculate stochastic diffusion contribution g to
    # new coordinate vector y for t_i+1
    g = np.array([0,
                  0,
                  (-1.)*cCm*np.sqrt(1. - alphaR),
                  (-1.)*cCp*np.sqrt(1. + alphaR)])
    return g

def qDriftRSJ(t, y, iBias, phiA, betaC, betaL, alphaI, alphaR, alphaC, alphaL):
    """
    ----------------------------------
    Description:
    ----------------------------------
    Drift term in the SDE for the RSJ model (no shunt capacitor, betaC=0).

    ----------------------------------
    Function arguments:
    ----------------------------------
```

```
    See 'qDrift' documentation.

    -------------------------------
    Returns:
    -------------------------------
    q:        Float array. Drift term evaluated at (t_i, y(t_i)).
    """
    # auxiliary variables
    cL = 1./(betaL*np.pi)
    cRm = 1./(1. - alphaR)
    cRp = 1./(1. + alphaR)

    # Calculate deterministic drift contribution q to
    # new coordinate vector y for t_i+1
    q = (np.array([cRm*(iBias/2*(1. + alphaL) - 2*phiA/betaL),
                   cRp*(iBias/2*(1. - alphaL) + 2*phiA/betaL)]) +
         np.dot(np.array([[(-cL)*cRm, cL*cRm],
                          [cL*cRp, (-cL)*cRp]]), y) +
         np.dot(np.array([[(-cRm)*(1. - alphaI), 0],
                          [0, (-cRp)*(1. + alphaI)]]), np.sin(y)))
    return q

def gDiffRSJ(t, y, gamma, betaC, betaL, alphaI, alphaR, alphaC, alphaL):
    """
    -------------------------------
    Description:
    -------------------------------
    Diffusion term in the SDE for the RSJ model (no shunt capacitor, betaC=0).

    -------------------------------
    Function arguments:
    -------------------------------
    See 'gDiff' documentation.

    -------------------------------
    Returns:
    -------------------------------
    g:        Float array. Diffusion term evaluated at (t_i, y(t_i)).
    """
    # auxiliary variables
    cRm = 1./(1. - alphaR)
    cRp = 1./(1. + alphaR)

    # Calculate stochastic diffusion contribution g to
    # new coordinate vector y for t_i+1
    g = np.array([(-1.)*cRm*np.sqrt(1. - alphaR),
                  (-1.)*cRp*np.sqrt(1. + alphaR)])
    return g

def simSquidIVcurve(iArray, yInit, hStep, Ttot, TinitSkip, method,
                    phiA, gamma, betaC, betaL, tauOU=None,
                    alphaI=0., alphaR=0., alphaC=0., alphaL=0.):
    """
    -------------------------------
    Description:
    -------------------------------
    Simulates a SQUID I-V characteristic curve for the given set of SQUID
    parameters.

    -------------------------------
    Function arguments:
    -------------------------------
    iArray:     Float array. SQUID bias current. Normalised to average critical
                current I0 of one SQUID junction.
    yInit:      Float array. Start values for junction phase (delta) and voltage
                (d delta/dt) variables in simulation for first value in bias
                current array iArray. Structure: [delta1, delta2, u1, u2]
    hStep:      Float. Step size of numerical simulation as a fraction of the
                inverse of the characteristic angular frequency wc=2 pi I0 R/Phi0.
    Ttot:       Float. Total simulation time. Normalised to wc^-1.
    TinitSkip:  Float. Time period during which transient from start values takes
```

```python
                place. Will be discarded in the calculation of the time averaged
                junction voltage. Normalised to wc^-1.
    method:     String. Decides which noise model is used. 'Gauss' for Gaussian
                noise and 'OU' for Ornstein-Uhlenbeck noise. For other choices the
                noise free case is simulated.
    phiA:       Float. SQUID flux bias. Normalised to Phi0.
    gamma:      Float. Noise parameter gamma = 2 pi kB T / (I0 Phi0).
    betaC:      Float. Steward-McCumber parameter. betaC = 2*pi*I0*R^2*C/Phi0
    betaL:      Float. Screening parameter. betaL = 2*L*I0/Phi0
    tauOU:      Float. Ornstein-Uhlenbeck relaxation time. Normalised to wc.
                tauOU = wc / fMax   with fMax corner frequency in noise power
                spectral density -> fMax ~ equivalent noise bandwidth 'ENBW'.
                Not used, 'None', in the case of Gaussian noise.
    alphaI:     Float. Asymmetry parameter for critical currents of the two
                SQUID junctions. By default 0. alphaI = (I0,2 - I0,1)/(I0,1 + I0,2)
    alphaR:     Float. Asymmetry parameter for shunt resistances of the two
                SQUID junctions. By default 0. alphaR = (R1 - R2)/(R1 + R2)
    alphaC:     Float. Asymmetry parameter for shunt capacitances of the two
                SQUID junctions. By default 0. alphaC = (C2 - C1)/(C1 + C2)
    alphaL:     Float. Asymmetry parameter for inductances of the two
                SQUID loop halves. By default 0. alphaL = (L2 - L1)/(L1 + L2)

    --------------------------------
    Returns:
    --------------------------------
    uAvgArray:  Float array. Data array of the simulated time averaged SQUID
                voltages for the specified bias current values in iArray.
    """
    # reserve memory for simulation data
    uAvgArray = np.empty_like(iArray)

    # counter for 10 percent status updates
    n10p = 0

    # use initial guess as start value for numerical simulation
    # --> calculated values in transient phase TinitSkip have to be excluded
    yStart = yInit

    for idx, iVal in enumerate(iArray):
        # run simulation for current iVal
        tCurr, dataCurr = heunSDEsquid(yStart, hStep, Ttot, method, iVal,
                                       phiA, gamma, betaC, betaL, tauOU,
                                       alphaI, alphaR, alphaC, alphaL,
                                       noiseCurrOutput=False)

        # calculate average voltage signal, exclude transient period
        mask = np.where(tCurr > TinitSkip)
        uSQUID = ((1. + alphaL)*np.array(dataCurr[:, 2]) +
                  (1. - alphaL)*np.array(dataCurr[:, 3]))/2.
        uAvgArray[idx] = np.trapz(uSQUID[mask], tCurr[mask])/(Ttot - TinitSkip)

        # update start value for numerical simulation with final data vector
        # for next iteration with different bias current
        yStart = dataCurr[-1]

        # status update
        if int(idx/np.alen(iArray)*10) != n10p:
            n10p += 1
            print('%d percent finished\n' % (n10p*10))

    return uAvgArray

def simSquidPhiVcurve(phiArray, yInit, hStep, Ttot, TinitSkip, method, i,
                      gamma, betaC, betaL, tauOU=None,
                      alphaI=0., alphaR=0., alphaC=0., alphaL=0.):
    """
    --------------------------------
    Description:
    --------------------------------
    Simulates a SQUID Phi-V characteristic curve for the given set of SQUID
    parameters.
```

```

    ------------------------------
    Function arguments:
    ------------------------------
    phiArray:   Float array. SQUID flux bias. Normalised to Phi0.
    yInit:      Float array. Start values for junction phase (delta) and voltage
                (d delta/dt) variables in simulation for first value in flux bias
                array phiArray. Structure: [delta1, delta2, u1, u2]
    hStep:      Float. Step size of numerical simulation as a fraction of the
                inverse of the characteristic angular frequency wc=2 pi I0 R/Phi0.
    Ttot:       Float. Total simulation time. Normalised to wc^-1.
    TinitSkip:  Float. Time period during which transient from start values takes
                place. Will be discarded in the calculation of the time averaged
                junction voltage. Normalised to wc^-1.
    method:     String. Decides which noise model is used. 'Gauss' for Gaussian
                noise and 'OU' for Ornstein-Uhlenbeck noise. For other choices the
                noise free case is simulated.
    i:          Float. SQUID bias current. Normalised to average critical current
                I0 of one SQUID junction.
    gamma:      Float. Noise parameter gamma = 2 pi kB T / (I0 Phi0).
    betaC:      Float. Steward-McCumber parameter. betaC = 2 pi I0 R^2 C/Phi0
    betaL:      Float. Screening parameter. betaL = 2 L I0/Phi0
    tauOU:      Float. Ornstein-Uhlenbeck relaxation time. Normalised to wc.
                tauOU = wc / fMax    with fMax corner frequency in noise power
                spectral density --> fMax ~ equivalent noise bandwidth 'ENBW'.
                Not used, 'None', in the case of Gaussian noise.
    alphaI:     Float. Asymmetry parameter for critical currents of the two
                SQUID junctions. By default 0. alphaI = (I0,2 - I0,1)/(I0,1 + I0,2)
    alphaR:     Float. Asymmetry parameter for shunt resistances of the two
                SQUID junctions. By default 0. alphaR = (R1 - R2)/(R1 + R2)
    alphaC:     Float. Asymmetry parameter for shunt capacitances of the two
                SQUID junctions. By default 0. alphaC = (C2 - C1)/(C1 + C2)
    alphaL:     Float. Asymmetry parameter for inductances of the two
                SQUID loop halves. By default 0. alphaL = (L2 - L1)/(L1 + L2)

    ------------------------------
    Returns:
    ------------------------------
    uAvgArray:  Float array. Data array of the simulated time averaged SQUID
                voltages for the specified flux bias values in phiArray.
    """
    # reserve memory for simulation data
    uAvgArray = np.empty_like(phiArray)

    # counter for 10 percent status updates
    n10p = 0

    # use initial guess as start value for numerical simulation
    # --> calculated values in transient phase TinitSkip have to be excluded
    yStart = yInit

    for idx, phiVal in enumerate(phiArray):
        # run simulation for current phiVal
        tCurr, dataCurr = heunSDEsquid(yStart, hStep, Ttot, method, i,
                                       phiVal, gamma, betaC, betaL, tauOU,
                                       alphaI, alphaR, alphaC, alphaL,
                                       noiseCurrOutput=False)

        # calculate average voltage signal, exclude transient period
        mask = np.where(tCurr > TinitSkip)
        uSQUID = ((1. + alphaL)*np.array(dataCurr[:, 2]) +
                  (1. - alphaL)*np.array(dataCurr[:, 3]))/2.
        uAvgArray[idx] = np.trapz(uSQUID[mask], tCurr[mask])/(Ttot - TinitSkip)

        # update start value for numerical simulation with final data vector
        # for next iteration with different bias current
        yStart = dataCurr[-1]

        # status update
        if int(idx/np.alen(phiArray)*10) != n10p:
            n10p += 1
```

```python
            print('%d percent finished\n' % (n10p*10))

    return uAvgArray

def simSquidIPhiVsurface(iArray, phiArray, yInit, hStep, Ttot, TinitSkip, method,
                         gamma, betaC, betaL, tauOU=None,
                         alphaI=0., alphaR=0., alphaC=0., alphaL=0.):
    """
    -------------------------------
    Description:
    -------------------------------
    Simulates a SQUID I-Phi-V surface of characteristic curves for the given set of
    SQUID parameters.

    -------------------------------
    Function arguments:
    -------------------------------
    iArray:       Float array. SQUID bias current. Normalised to average critical
                  current I0 of one SQUID junction.
    phiArray:     Float array. SQUID flux bias. Normalised to Phi0.
    yInit:        Float array. Start values for junction phase (delta) and voltage
                  (d delta/dt) variables in simulation. Used for first value in bias
                  current array iArray for every value in flux bias array phiArray.
                  Structure: [delta1, delta2, u1, u2]
    hStep:        Float. Step size of numerical simulation as a fraction of the
                  inverse of the characteristic angular frequency wc=2 pi I0 R/Phi0.
    Ttot:         Float. Total simulation time. Normalised to wc^-1.
    TinitSkip:    Float. Time period during which transient from start values takes
                  place. Will be discarded in the calculation of the time averaged
                  junction voltage. Normalised to wc^-1.
    method:       String. Decides which noise model is used. 'Gauss' for Gaussian
                  noise and 'OU' for Ornstein-Uhlenbeck noise. For other choices the
                  noise free case is simulated.
    gamma:        Float. Noise parameter gamma = 2 pi kB T / (I0 Phi0).
    betaC:        Float. Steward-McCumber parameter. betaC = 2 pi I0 R^2 C/Phi0
    betaL:        Float. Screening parameter. betaL = 2 L I0/Phi0
    tauOU:        Float. Ornstein-Uhlenbeck relaxation time. Normalised to wc.
                  tauOU = wc / fMax   with fMax corner frequency in noise power
                  spectral density -> fMax ~ equivalent noise bandwidth 'ENBW'.
                  Not used, 'None', in the case of Gaussian noise.
    alphaI:       Float. Asymmetry parameter for critical currents of the two
                  SQUID junctions. By default 0. alphaI = (I0,2 - I0,1)/(I0,1 + I0,2)
    alphaR:       Float. Asymmetry parameter for shunt resistances of the two
                  SQUID junctions. By default 0. alphaR = (R1 - R2)/(R1 + R2)
    alphaC:       Float. Asymmetry parameter for shunt capacitances of the two
                  SQUID junctions. By default 0. alphaC = (C2 - C1)/(C1 + C2)
    alphaL:       Float. Asymmetry parameter for inductances of the two
                  SQUID loop halves. By default 0. alphaL = (L2 - L1)/(L1 + L2)

    -------------------------------
    Returns:
    -------------------------------
    uAvgArray:    Float array. Data array of the simulated time averaged SQUID
                  voltages for the specified range of bias current and flux bias
                  values in iArray and phiArray. Structure: uAvgArray[idxPhi, idxI]
    """
    # reserve memory for simulation data
    uAvgArray = np.empty((np.alen(phiArray), np.alen(iArray)))

    # counter for 10 percent status updates
    n10p = 0

    for idxPhi, phiVal in enumerate(phiArray):
        # use initial guess as start value for numerical simulation
        # --> calculated values in transient phase TinitSkip have to be excluded
        yStart = yInit

        for idxI, iVal in enumerate(iArray):
            # run simulation for current iVal and phiVal
            tCurr, dataCurr = heunSDEsquid(yStart, hStep, Ttot, method, iVal,
                                           phiVal, gamma, betaC, betaL, tauOU,
```

```
                                          alphaI, alphaR, alphaC, alphaL,
                                          noiseCurrOutput=False)

            # calculate average voltage signal, exclude transient period
            mask = np.where(tCurr > TinitSkip)
            uSQUID = ((1. + alphaL)*np.array(dataCurr[:, 2]) +
                      (1. - alphaL)*np.array(dataCurr[:, 3]))/2.
            uAvgArray[idxPhi, idxI] = np.trapz(uSQUID[mask],
                                              tCurr[mask])/(Ttot - TinitSkip)

            # update start value for numerical simulation with final data vector
            # for next iteration with different bias current
            yStart = dataCurr[-1]

        # status update
        if int(idxPhi/np.alen(phiArray)*10) != n10p:
            n10p += 1
            print('%d percent finished\n' % (n10p*10))

    return uAvgArray

def parallelSquidIV(phiA, iArray, yInit, hStep, Ttot, TinitSkip, method,
                    gamma, betaC, betaL, tauOU, alphaI, alphaR, alphaC, alphaL):
    """
    -------------------------------
    Description:
    -------------------------------
    Function wrapper for the parallelised computation of the SQUID I-V curve used
    for fitting procedures.

    -------------------------------
    Function arguments:
    -------------------------------
    See 'simSquidIVcurve' documentation.

    -------------------------------
    Returns:
    -------------------------------
    Simulated I-V curve of simSquidIVcurve for the specified SQUID parameters.
    """
    return simSquidIVcurve(iArray, yInit, hStep, Ttot, TinitSkip, method,
                           phiA, gamma, betaC, betaL, tauOU,
                           alphaI, alphaR, alphaC, alphaL)

def simSquidIPhiVsurfaceMP(iArray, phiArray, yInit, hStep, Ttot, TinitSkip, method,
                           gamma, betaC, betaL, tauOU=None,
                           alphaI=0., alphaR=0., alphaC=0., alphaL=0.):
    """
    -------------------------------
    Description:
    -------------------------------
    Multi-processing version of simSquidIPhiVSurface. Simulates a SQUID I-Phi-V
    surface of characteristic curves for the given set of SQUID parameters using
    multi-core computation.

    -------------------------------
    Function arguments:
    -------------------------------
    See 'simSquidIPhiVsurface' documentation.

    -------------------------------
    Returns:
    -------------------------------
    uAvgArray:  Float array. Data array of the simulated time averaged SQUID
                voltages for the specified range of bias current and flux bias
                values in iArray and phiArray. Structure: uAvgArray[idxPhi, idxI]
    """
    # SQUID parameters
    pars = (iArray, yInit, hStep, Ttot, TinitSkip, method, gamma, betaC, betaL,
            tauOU, alphaI, alphaR, alphaC, alphaL)

```

```
    # use parallelSquidIV function wrapper for parallelised computation
    # order of phiArray is translated to uAvgArray
    uAvgArray = pm.map(parallelSquidIV, phiArray, *pars, pm_chunksize=1,
                       pm_processes=4, pm_pbar=True)

    return uAvgArray

def squidIVFit(iArray, I0, R0, phiA, gamma, betaC, betaL, tauOU=None, alphaI=0.,
              alphaR=0., alphaC=0., alphaL=0., yInit=[1., 0.5, 1e-4, 1e-4],
              hStep=0.5, Ttot=1e3, TinitSkip=1e2, method='Gauss'):
    """
    -------------------------------
    Description:
    -------------------------------
    Function wrapper for fitting the simulated SQUID I-V model to an experimental
    data set. Translates current and voltage from normalised values into physical
    quantities.

    -------------------------------
    Function arguments:
    -------------------------------
    I0:   Float. Average critical current of the two Josephson junctions.
          I0 = (I0,1 + I0,2)/2
    R0:   Float. Two times parallel resistance of the junction shunt resistors.
          R0 = 2 R1 R2/(R1 + R2)
    Rest: See 'simSquidIVcurve' documentation.

    -------------------------------
    Returns:
    -------------------------------
    vArray:     Float array. Data array of the simulated time averaged SQUID
                voltages for the specified bias current values in iArray.
    """
    vArrayTemp = simSquidIVcurve(iArray/I0, yInit, hStep, Ttot, TinitSkip, method,
                                 phiA, gamma, betaC, betaL, tauOU, alphaI, alphaR,
                                 alphaC, alphaL)

    vArray = I0*R0*vArrayTemp

    return vArray

def squidPhiVFit(iCoilArray, cIPhi, phiCoil0, I0, R0, i, gamma, betaC, betaL,
                 tauOU=None, alphaI=0., alphaR=0., alphaC=0., alphaL=0.,
                 yInit=[1., 0.5, 1e-4, 1e-4], hStep=0.5, Ttot=1e3, TinitSkip=1e2,
                 method='Gauss'):
    """
    -------------------------------
    Description:
    -------------------------------
    Function wrapper for fitting the simulated SQUID Phi-V model to an experimental
    data set. Translates current and voltage from normalised values into physical
    quantities.

    -------------------------------
    Function arguments:
    -------------------------------
    iCoilArray: Float array. Bias coil current.
    cIPhi:      Float. Translation factor between coil current and magnetic flux
                phiA. phiArray = cIPhi*iCoilArray - phiCoil0
    phiCoil0:   Float. Flux offset for 0 applied coil current.
    I0:         Float. Average critical current of the two Josephson junctions.
                I0 = (I0,1 + I0,2)/2
    R0:         Float. Two times parallel resistance of the junction shunt
                resistors. R0 = 2 R1 R2/(R1 + R2)
    Rest:       See 'simSquidPhiVcurve' documentation.

    -------------------------------
    Returns:
    -------------------------------
    vArray:     Float array. Data array of the simulated time averaged SQUID
                voltages for the specified coil current values in iCoilArray.
```

```
    """
    vArrayTemp = simSquidPhiVcurve(cIPhi*iCoilArray - phiCoil0, yInit, hStep, Ttot,
                                   TinitSkip, method, i/I0, gamma, betaC, betaL,
                                   tauOU, alphaI, alphaR, alphaC, alphaL)

    vArray = I0*R0*vArrayTemp

    return vArray

def squidIPhiVFit(iArray, iCoilArray, I0, R0, cIPhi, phiCoil0, gamma, betaC, betaL,
                  tauOU=None, alphaI=0., alphaR=0., alphaC=0., alphaL=0.,
                  yInit=[1., 0.5, 1e-4, 1e-4], hStep=0.5, Ttot=1e3, TinitSkip=1e2,
                  method='Gauss'):
    """
    -------------------------------
    Description:
    -------------------------------
    Function wrapper for fitting the simulated SQUID I-Phi-V model to an
    experimental data set, using parallelised computation. Translates current and
    voltage from normalised values into physical quantities.

    -------------------------------
    Function arguments:
    -------------------------------
    iArray:     Float array. SQUID bias current. Normalised to average critical
                current I0 of one SQUID junction.
    iCoilArray: Float array. Bias coil current.
    I0:         Float. Average critical current of the two Josephson junctions.
                I0 = (I0,1 + I0,2)/2
    R0:         Float. Two times parallel resistance of the junction shunt
                resistors. R0 = 2 R1 R2/(R1 + R2)
    cIPhi:      Float. Translation factor between coil current and magnetic flux
                phiA. phiArray = cIPhi*iCoilArray - phiCoil0
    phiCoil0:   Float. Flux offset for 0 applied coil current.
    Rest:       See 'simSquidIPhiVsurface' documentation.

    -------------------------------
    Returns:
    -------------------------------
    vArray:       Float array. Data array of the simulated time averaged SQUID
                  voltages for the specified range of SQUID bias and bias coil
                  current values in iArray and iCoilArray.
                  Structure: vArray[idxICoil, idxIBias]
    """
    vArrayTemp = simSquidIPhiVsurfaceMP(iArray/I0, iCoilArray/cIPhi - phiCoil0,
                                        yInit, hStep, Ttot, TinitSkip, method,
                                        gamma, betaC, betaL, tauOU,
                                        alphaI, alphaR, alphaC, alphaL)

    vArray = I0*R0*np.array(vArrayTemp)

    return vArray
```

The following routine was used for fitting the SQUID I-Φ-V numerical model to experimental data. In the optimization it is ensured that only physically meaningful configurations are tested. To this end, the fit-parameters are implemented as relative changes to the initial SQUID variables or restricted to the relevant parameter space.

```python
import numpy as np
import scipy as scp
from scipy import optimize

# import library for SQUID numerical simulations
from numSimSQUID import *

# IMPORT EXPERIMENTAL DATA:
# iBiasSample -> SQUID bias currents
# iCoilSample -> Bias coil currents
# vSample     -> SQUID output voltages (Shape: (nICoil, nIBias))

# configure simulation and set initial values for SQUID parameters
yInit = [1., 0.5, 1e-4, 1e-4]; hStep = 0.2; Ttot = 1e4; TinitSkip = 1e3;
method = 'Gauss'

I0Init = 3.80e-05; R0Init = 16.68; cIPhiInit = 6.85e-4; phiCoil0Init = 0.095;
gammaInit = 3.41e-2; betaCInit = 1.043; betaLInit = 4.640;
alphaIInit = 0.202; alphaRInit = 0.027; alphaCInit = 0.246; alphaLInit = 0.167

def varsRelToAbs(x):
    """ Helper function for translating variables from relative to absolute """
    (I0Rel, R0Rel, gammaRel, betaCRel, betaLRel,
     tanAlphaI, tanAlphaR, tanAlphaC, tanAlphaL) = x

    I0 = I0Init*abs(I0Rel)
    R0 = R0Init*abs(R0Rel)
    gamma = gammaInit*abs(gammaRel)
    betaC = betaCInit*abs(betaCRel)
    betaL = betaLInit*abs(betaLRel)
    alphaI,alphaR,alphaC,alphaL = 2/np.pi*np.arctan(np.array([tanAlphaI, tanAlphaR,
                                                             tanAlphaC, tanAlphaL]))

    return np.array([I0, R0, gamma, betaC, betaL, alphaI, alphaR, alphaC, alphaL])

def squidIPhiVFitLSWrapper(x, iBiasArray, iCoilArray, vArray):
    """ Wrapper function for least squares expression for minimization """
    # translate variables from relative to absolute
    I0, R0, gamma, betaC, betaL, alphaI, alphaR, alphaC, alphaL = varsRelToAbs(x)

    # sum of squared residuals
    return np.linalg.norm(vArray - squidIPhiVFit(iBiasArray, iCoilArray, I0, R0,
                                    cIPhiInit, phiCoil0Init, gamma, betaC, betaL,
                                    alphaI=alphaI, alphaR=alphaR,
                                    alphaC=alphaC, alphaL=alphaL, hStep=hStep,
                                    Ttot=Ttot, TinitSkip=TinitSkip, method=method))

if __name__ == '__main__': # necessary for multi-processing library
    # use relative parameters wrt. initial values for optimization to circumvent
    # unphysical results
    I0Curr, R0Curr, gammaCurr, betaCCurr, betaLCurr = np.ones(5)
    alphaICurr, alphaRCurr, alphaCCurr, alphaLCurr = np.tan(np.pi/2*
                        np.array([alphaIInit, alphaRInit, alphaCInit, alphaLInit]))

    # Nelder-Mead minimization
#   res = scp.optimize.minimize(squidIPhiVFitLSWrapper,
#                       np.array([I0Curr, R0Curr, gammaCurr, betaCCurr, betaLCurr,
#                                 alphaICurr, alphaRCurr, alphaCCurr, alphaLCurr]),
#                       args=(iBiasSample, iCoilSample, vSample), callback=print,
#                       method='Nelder-Mead', options={'disp':True, 'maxiter':50,
#                                                      'maxfev':100, 'fatol':5e-6})

```

```
    # Basinhopping minimization with Nelder-Mead
    res = scp.optimize.basinhopping(squidIPhiVFitLSWrapper,
                         np.array([I0Curr, R0Curr, gammaCurr, betaCCurr, betaLCurr,
                              alphaICurr, alphaRCurr, alphaCCurr, alphaLCurr]),
                         niter=10,stepsize=0.2,interval=3,callback=print,disp=True,
                         minimizer_kwargs={'method':'Nelder-Mead',
                                      'args':(iBiasSample,iCoilSample,vSample),
                                      'options':{'disp':True, 'maxiter':50,
                                           'maxfev':100, 'fatol':5e-6}})

    # translate variables from relative to absolute
    [I0Curr, R0Curr, gammaCurr, betaCCurr, betaLCurr,
     alphaICurr, alphaRCurr, alphaCCurr, alphaLCurr] = varsRelToAbs(res.x)

    # Calculate simulation result
    simSqArray = squidIPhiVFit(iBiasSample, iCoilSample, I0Curr, R0Curr,
                              cIPhiInit, phiCoil0Init, gammaCurr, betaCCurr,
                              betaLCurr, alphaI=alphaICurr, alphaR=alphaRCurr,
                              alphaC=alphaCCurr, alphaL=alphaLCurr, hStep=hStep,
                              Ttot=Ttot, TinitSkip=TinitSkip)

    # SAVE SIMULATION DATA
```